

Theoretical Characterization of Aromatic Exciplex Fluorescence

Thesis by
Rachel Ann Krueger

In Partial Fulfillment of the Requirements for the
Degree of
Doctor of Philosophy

The logo for the California Institute of Technology (Caltech), featuring the word "Caltech" in a bold, orange, sans-serif font.

CALIFORNIA INSTITUTE OF TECHNOLOGY
Pasadena, California

2020
Defended July 19, 2019

© 2020

Rachel Ann Krueger
ORCID: 0000-0002-5457-2931

All rights reserved

ACKNOWLEDGEMENTS

This work would not have been possible without the enthusiasm and guidance of my research advisor, Professor Guillaume Blanquart. I thank him for introducing me to some of the most difficult and interesting problems in combustion, and I will miss our weekly soot discussions. The depth of chemistry knowledge among my thesis committee members, Professor Mitchio Okumura, Professor Tom Miller, and Professor Geoff Blake, has also been invaluable. I am grateful to the National Science Foundation Department of Graduate Education for their financial support (DGE-1745301). Research mentors at Mount Holyoke College and the Max Planck Institute for Solid State Research were vital to my scientific growth, and I am particularly indebted to Professor Maria Gomez and Dr. Klaus-Dieter Kreuer.

My time at Caltech has been a pleasure, thanks in large part to the company of my graduate compatriots—the members of the Blanquart group, my classmates in the chemistry department, and the ones in chemical engineering. With so many pleasant lunches, cups of tea, and trips to the opera, it's a wonder that we have all passed thermodynamics and enjoyed relative academic success thereafter. I'm grateful to Nick, in particular, for sticking with me through the peaks and valleys of life and research. I thank my sister for doing everything first, and my parents for their constant love and support.

ABSTRACT

The negative effects of soot on the environment and human health are well known, but efforts to decrease soot production in combustion processes are hampered by the absence of accurate, transferable models for soot formation. Uncertainties about the soot nucleation mechanism, including the size and properties of the molecules involved and the relative importance of chemical and physical stabilization, have made model development difficult. Electronic spectroscopy methods such as laser-induced fluorescence (LIF) have the potential to characterize transient soot nuclei, but interpreting spectra requires a comprehensive understanding of the photoresponse of likely soot precursors, namely polycyclic aromatic hydrocarbon (PAH) dimers and clusters. To build up a picture of this photoresponse using theory, it is necessary to evaluate which methods are capable of treating the relevant molecules at reasonable cost while capturing the excited-state and noncovalent interactions involved in excimer and exciplex formation, a key excited-state process for aromatic clusters. In this work, we describe extensive benchmarking of basis set error in highly-accurate perturbatively-corrected multireference calculations of exciplex interaction strength and use the best possible multireference approach to evaluate the performance of less-expensive time-dependent density functional theory (TDDFT) results. Using the most accurate TDDFT methods, we explore how the geometric and electronic properties of the monomers influence excited-state interactions in complexes, considering a large database of complexes. A predictive model for exciplex fluorescence emissions of complexes containing six-membered ring PAHs based on monomer HOMO-LUMO gaps is proposed. We describe the contrasting photoresponse of PAHs containing five-membered rings, where nonaromatic groups produce conformational flexibility that has a strong impact on absorption and emission behavior.

PUBLISHED CONTENT AND CONTRIBUTIONS

- (1) Krueger, R. A.; Blanquart, G. *J. Phys. Chem. A* **2019**, *123*, 1796–1806, DOI: 10.1021/acs.jpca.8b11461. R.K. participated in the conception of the project, ran the calculations, analyzed the data, and wrote the manuscript.
- (2) Krueger, R. A.; Blanquart, G. *Phys. Chem. Chem. Phys.* **2019**, *21*, 10325–10335, DOI: 10.1039/c9cp02027f. R.K. participated in the conception of the project, ran the calculations, analyzed the data, and wrote the manuscript.
- (3) Krueger, R. A.; Blanquart, G. *Combust. Flame* **2019**, This manuscript is under review. R.K. participated in the conception of the project, ran the calculations, analyzed the data, and wrote the manuscript.
- (4) Krueger, R. A.; Blanquart, G. *Int. J. Quantum Chem.* **2019**, *119*, e25819, DOI: 10.1002/qua.25819. R.K. participated in the conception of the project, ran the calculations, analyzed the data, and wrote the manuscript.

TABLE OF CONTENTS

Acknowledgements	iii
Abstract	iv
Published Content and Contributions	v
Table of Contents	vi
List of Illustrations	vii
List of Tables	ix
Chapter I: Introduction	1
1.1 The Soot Nucleation Problem	2
1.2 <i>In Situ</i> Electronic Spectroscopy Techniques for Characterizing Soot Nuclei	4
1.3 Study Objectives	7
Chapter II: Multireference Exciplex Binding Energies: Basis Set Convergence and Error	11
2.1 Introduction	11
2.2 Computational Methods	13
2.3 Results and Discussion	17
Chapter III: Exciplex Stabilization in Asymmetric Acene Dimers	27
3.1 Introduction	27
3.2 Computational Methods	29
3.3 Results and Discussion	33
Chapter IV: Predicting Aromatic Exciplex Fluorescence Emission Energies	47
4.1 Introduction	47
4.2 Methods	47
4.3 Results and Discussion	49
Chapter V: Predicting the Photoresponse of Soot Nuclei: Spectroscopic Char- acteristics of Aromatic Aggregates Containing Five-Membered Rings	67
5.1 Introduction	67
5.2 Computational Methods	67
5.3 Results and Discussion	68
Chapter VI: Conclusions and Outlook	78
6.1 Basis Set Selection for Multireference Calculations: Best Practices	78
6.2 Asymmetric Acene Exciplex Properties via Multireference and DFT Methods	79
6.3 Towards a Predictive Model for Aromatic Exciplex Fluorescence Emission Energies	80
6.4 Exploring the Spectroscopic Impacts of Five-Membered Ring Groups in PAH Complexes	80
6.5 Directions for Future Work	81

LIST OF ILLUSTRATIONS

<i>Number</i>	<i>Page</i>
1.1 Processes involved in soot formation.	2
1.2 Energetic quantities used to describe exciplex formation.	6
2.1 PAH complex geometries.	15
2.2 (BzBz)* binding energy values as a function of basis set cardinality.	17
2.3 (BzBz)* absolute binding energy error.	20
2.4 (BdBz)* E_B and $E_{B,CP}$ values as a function of basis set cardinality.	21
2.5 (BdBz)* absolute binding energy error.	22
2.6 (BzNa)* E_B and $E_{B,CP}$ values as a function of basis set cardinality.	24
2.7 (BzNa)* absolute binding energy error.	24
3.1 Asymmetric exciplex geometries.	33
3.2 Binding energies without the D3 dispersion correction.	34
3.3 (BN)* S_1 potential energies.	36
3.4 (BA)* S_1 potential energies.	36
3.5 (NA)* S_1 potential energies.	37
3.6 TDDFT binding energies E_B as a function of NEVPT2 binding energies.	37
3.7 TDDFT optimal intermolecular separations r_0 as a function of NEVPT2 r_0 values.	37
3.8 Binding energy E_B as a function of the number of carbons.	39
3.9 Frontier natural transition orbital isosurfaces for (BN)*.	40
3.10 Frontier natural transition orbital isosurfaces for (BA)*.	41
3.11 Frontier natural transition orbital isosurfaces for (NA)*.	41
4.1 Comparison of LC-BLYP-T and B2PLYP-D3 ΔE_F values.	48
4.2 Clar structures for the PAH monomers.	50
4.3 Variation in ΔE_F for excimers containing tet isomers.	51
4.4 Frontier orbitals for the tet and benzo excimers.	51
4.5 PAH edge groups.	53
4.6 Variation in ΔE_F for excimers containing pent isomers	57
4.7 Variation in ΔE_F for complexes containing naphthalene.	58
4.8 Variation in ΔE_F for all complexes.	59
4.9 Heterodimer geometries.	60

4.10	Emission energies for aliphatically-bridged complexes vs. emission energies for noncovalent complexes.	63
4.11	Frontier orbitals for aliphatically-bridged benzene dimers.	64
5.1	Complex structures optimized in the ground state.	69
5.2	Ground state binding energies as a function of mass.	70
5.3	Homodimer structures optimized in the S_1 state.	73
5.4	Cyclo dimer and cyclo-benz complex frontier orbitals.	73
5.5	Partitioning of monomer absorption energy ΔE_A	73
5.6	Heterodimer structures optimized in the S_1 state.	74

LIST OF TABLES

<i>Number</i>	<i>Page</i>
2.1 Binding energies for different starting orbital types and DMRG parameters.	14
2.2 Exciplex binding energies.	18
2.3 Extrapolated complete basis set binding energies.	19
3.1 Binding energies and intermolecular separations.	35
3.2 Monomer S ₁ Absorption Energies ΔE_V and ΔE_A	36
3.3 Statistical descriptors computed using one-electron transition density matrices.	43
4.1 Electronic properties for all monomers.	54
4.2 Electronic and geometric properties of noncovalent homodimers. . .	55
4.3 R^2 values for the complex descriptors.	55
4.4 Electronic and geometric properties of noncovalent heterodimers. . .	56
4.5 Emission energies for covalently-linked structures.	65
5.1 Electronic properties of the monomers.	72
5.2 Spectroscopic parameters and excited state planarity descriptors for complexes.	72

Chapter 1

INTRODUCTION

Soot particles are a major product of incomplete hydrocarbon combustion. Mature soot particles are made up of one or more primary particles that are 10-50 nm in diameter and have C-H ratios between 10 and 20.[1] They represent a major source of atmospheric particulate matter with diameter less than 2.5 μm ($\text{PM}_{2.5}$). Exposure to $\text{PM}_{2.5}$ levels below the 12 $\mu\text{g}/\text{m}^3$ allowed by the United States' National Ambient Air Quality Standards has been associated with increased mortality. Approximately 12,000 US deaths could be avoided annually if $\text{PM}_{2.5}$ concentrations were maintained at 11 $\mu\text{g}/\text{m}^3$. [2]

Globally, soot represents a major component of household air pollution, which causes an estimated 3.9 million premature deaths annually. The vast majority of these deaths have been attributed to diseases of the respiratory and cardiovascular systems.[3] The role soot particles play in these adverse health outcomes is an area of active research.[4] It is hypothesized that besides acting as carriers of highly mutagenic polycyclic aromatic hydrocarbons (PAHs), soot particles increase the production of radical species associated with DNA damage in cells and inflammation. Characterizing the role of soot particles in this process will require detailed modeling not just of soot concentration, but also morphology, charge, and chemical makeup of particle surfaces.[5]

Detailed predictions of soot particle size and properties would also improve descriptions of soot effects in climate models. Beyond absorbing and trapping energy from sunlight as aerosols, soot particles participate in radiative forcing by altering cloud formation patterns.[6] Soot deposition decreases the albedo of snow and ice surfaces, and heat radiated from soot particles contributes to earlier snow melt in arctic regions, exposing lower-albedo surfaces such as soil and rock.[7, 8] In the short term, smaller snowpacks and faster snowpack melting can decrease summer water availability.[9]

Accurate modeling of soot production and soot character could give designers the information necessary to avoid or improve the most polluting combustion processes, mitigating in part the negative environmental and health consequences of combustion.[10] Moreover, energy absorption and radiation by soot particles within

the combustion environment can play an important role in heat transfer within flames.[11] Inaccuracies in soot formation predictions can then introduce error into predictions of other properties, including the amounts of toxic pollutants such as CO and formaldehyde produced.

1.1 The Soot Nucleation Problem

The Soot Formation Process

The general soot formation process involves a series of chemical and physical growth steps, illustrated in Fig. 1.1. An initial population of hydrocarbon precursors and radicals undergo addition reactions, yielding larger molecules. This population is expected to include a large number of PAHs, which are relatively stable at flame temperature.[12] Nascent soot particles have been shown to contain molecules with sizes that are consistent with PAHs containing four to five six-membered rings, such as pyrene and perylene.[13] Nascent soot particles have much lower C-H ratios than mature particles, around 1.4–2.5. Moderately-sized PAHs such as pyrene and coronene have C-H ratios in this range. It is generally agreed that both PAHs and substituted PAHs play a role in soot nucleation.[14]

Once nucleation of primary particles has occurred, particle growth can continue through a mixture of physical adsorption and addition reactions. Collision between primary particles then leads to aggregation. Finally, oxidation through surface reactions with radicals occurs.[15]

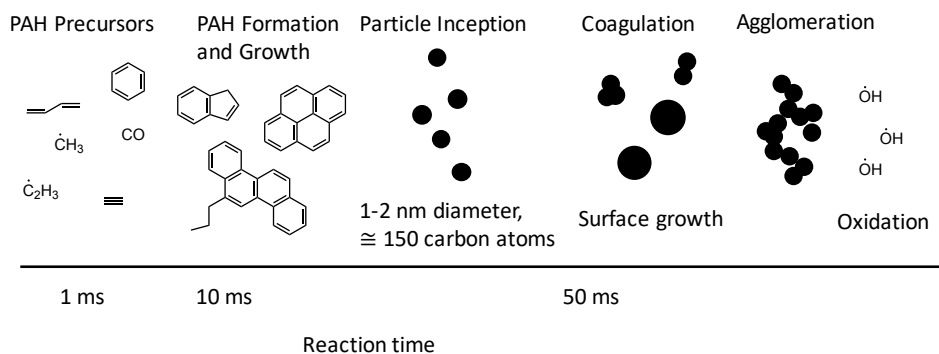


Figure 1.1: Processes involved in soot formation.[15]

Proposed Mechanisms for Soot Nucleation

Despite decades of research, the mechanism of the nucleation step remains unclear. Historically, three basic nucleation processes have been proposed. The first involves

the noncovalent association of two or more PAHs. Stabilizing dispersion interactions are postulated to compensate for the loss of translational entropy that results from dimerization.[14] However, it has been demonstrated that the moderately-sized PAHs likely to be present in flames do not form thermodynamically stable dimers at flame temperature,[16] and the lifetime of noncovalent dimers formed is likely to be short.[17] Traditional molecular dynamics (MD) simulations do not allow for bond formation and are thus able to capture only dispersion-driven soot nucleation, but this process is not observed at flame-relevant temperatures for the moderately-sized PAHs that are expected to be present in flames. [18, 19] Metadynamics simulations involving the association of two PAH molecules have yielded similar results.[20–22]

These results are not surprising, given that even one of the largest PAHs expected to be present at appreciable concentrations, coronene, has a boiling temperature of ≈ 800 K at atmospheric pressure,[23] well below the 1500-1800 K range encountered in flames. The single exception is a study[24] that is now acknowledged to include artificially strong PAH-PAH dispersion interactions, inflating the probability of nucleation.[18, 25] It is important to note, though, that kinetic soot formation models that use the dimerization of pyrene or similarly-sized PAHs are often able to reproduce experimental results, obtained for certain flames, e.g., [26] and [27], which may reflect felicitous choice of parameters or the possibility that calculated pyrene dimerization rates serve as a reasonable proxy for the true underlying molecular-level nucleation mechanism.

The second proposed soot nucleation pathway, chemical nucleation, involves covalent bond formation. This bond formation may occur between small to moderately-sized PAHs, with chemical dimerization taking place after hydrogen abstraction by a small radical such as H, CH₃, or OH. The bond formation step may even be preceded by noncovalent dimer formation.[28] Soot formation has been observed in regions of flames where the temperature is too low to maintain the necessary population of small radicals, though, suggesting that this mechanism cannot be the only soot formation pathway, and may not even represent a major pathway in most systems.[14]

Recently, an alternate mechanism for covalent bond formation between PAHs has been proposed. Mass spectra suggest that a population of small resonantly-stabilized radicals (RSRs) such as phenyl, cyclopentadienyl, and indenyl, as well as larger species, exist in flames in appreciable concentrations. These RSRs could serve as initiator species in a radical chain reaction mechanism for PAH cluster growth,

reacting with closed-shell PAHs and generating new RSRs. Most of these pathways would involve a combination of barrierless and low-barrier reactions, allowing them to occur in lower-temperature regions of the flame.[29] Mechanisms for PAH growth involving RSRs have been suggested,[30] but Johansson and coworkers' proposed mechanism involves the formation of aliphatic bonds between PAH units, resulting in the formation of nonplanar, three-dimensional structures of connected PAH groups.[29]

A third pathway, involving the growth of covalently-linked PAH dimers or "aromers" into folded graphene-like soot nuclei has also been proposed. A similar mechanism was suggested to account for the presence of fullerenes in some flames.[31] The slow kinetics involved, though, make this mechanism unfeasible even at flame temperature.[32]

1.2 *In Situ* Electronic Spectroscopy Techniques for Characterizing Soot Nuclei

Experimental characterization of soot nuclei represents a significant challenge. Soot nuclei are by definition transient species, which either undergo further growth processes to become nascent soot particles or dissociate into the smaller precursor species. Nuclei can undergo additional chemical and physical processes during the process of extraction for *ex situ* analysis, making diagnostics that may be performed in the flame itself with minimal effect on the combustion process desirable. Two such diagnostics both fall under the umbrella of electronic spectroscopy: UV-visible absorption and laser-induced fluorescence.

UV-Visible Absorption

UV-Visible absorption has shown promise as a method for distinguishing soot particles based on maturity. Nascent soot particles tend to absorb in the UV range, while more mature soot particles absorb at longer wavelengths, in the visible range.[1, 33] This effect is visible in absorption spectra taken at varying heights above the burner (HAB) in a flame, where larger HAB, and thus increased particle maturity, is associated with absorption at lower energies.[34]

The absorption behavior of soot particles in flames has also been interpreted by modeling soot particles in flames as amorphous semiconductors.[33, 35, 36] It has been shown that the low-energy end of the absorption bands obtained for such systems can provide an estimate of the transition energy from the ground state to

localized electronic excited states, i.e., the optical bandgap E_g^{opt} , [37] according to

$$h\nu\alpha \approx (h\nu - E_g^{opt})^r, \quad (1.1)$$

where r is a constant that depends on the allowedness of the electronic transition. If the absorber is assumed to be a PAH monomer, the following empirical relationship may be used to determine the total mass M of the monomer:

$$E_g^{opt} = \frac{5.8076}{M^{1/2}} + 0.5413. \quad (1.2)$$

This relationship yields an average monomer size of approximately 14 aromatic rings. [36] The possibility of partially-delocalized absorption involving multiple monomers stacked close together within a soot particle was also considered, with the effect of decreasing the monomer size required to explain the results to approximately 10 aromatic rings. [35]

Laser-Induced Fluorescence

Rather than determining the energies and shapes of absorption bands, laser-induced fluorescence (LIF) experiments involve excitation with light at a single, predetermined frequency. Fluorescence from the population of absorbers is then measured. A number of LIF studies, e.g., [38, 39], have shown that UV-range excitation leads to a broad, red-shifted fluorescence emission at lower-energy UV and visible wavelengths. The lowest-energy fluorescence emissions are observed for large HAB, where soot nucleation is expected to occur. [40] This absorption-emission profile is consistent with the expected photoresponse of PAH dimers or larger clusters, which can involve exciplex formation. [40, 41]

Exciplex (“excited complex”) or excimer (“excited dimer”) formation occurs when an electron-hole pair becomes delocalized over neighboring chromophores such as PAHs, stabilizing the intermolecular interaction through a mixture of exciton resonance and charge resonance. This is reflected by nonzero contributions of both locally-excited states and charge transfer states to the overall wavefunction for chromophores A and B :

$$\Psi_{Exciplex} = c_1\Psi(A^*B) + c_2\Psi(AB^*) + c_3\Psi(A^{\cdot-}B^{\cdot+}) + c_4\Psi(A^{\cdot+}B^{\cdot-}). \quad (1.3)$$

Exciplex formation is known to play an important role in the photophysics and photochemistry of many systems containing aggregates of chromophores, from DNA [42] to organic photovoltaics. [43, 44] The strength of the exciplex interaction is proportional to the orbital overlap of the two molecules, which decreases exponentially

with increasing internuclear distance. Thus, an observable exciplex emission in flames indicates the presence of PAHs in close proximity to one another—the optimal intermolecular distances for S_1 excimers and exciplexes of small acenes range from $\approx 3.0\text{--}3.3 \text{ \AA}$. [45–48]

The energetics of exciplex formation are summarized in Fig. 1.2. Based on Kasha’s rule,[49] we assume that fast internal conversion means that fluorescence emission typically occurs from the lowest-energy singlet (S_1) excited state, allowing us to confine our analysis to the S_1 and S_0 states. The initial photoabsorption event often involves a single molecule,[50] so the absorption energy ΔE_A for the complex is similar to the absorption energy for one of the constituent monomers. Exciplex stabilization is quantified using the excited-state binding energy $E_{B,E}$.

Fluorescence emission occurs mostly from the minimum-energy geometry on the excited-state potential energy surface. The emission energy ΔE_F reflects the energy difference between the excited-state minimum-energy geometry on the excited-state potential energy surface and the same geometry on the ground-state potential energy surface. Often, in the ground state, this geometry is unfavorable relative to the reference configuration, which consists of the two monomers at infinite separation. The energy difference between the ground-state reference energy and the ground state energy at the excited-state minimum-energy geometry is the repulsion energy, E_R . The strength of the ground-state interaction between the two molecules is quantified by $E_{B,G}$, the energy difference between the ground-state minimum-energy configuration and the ground-state reference configuration.

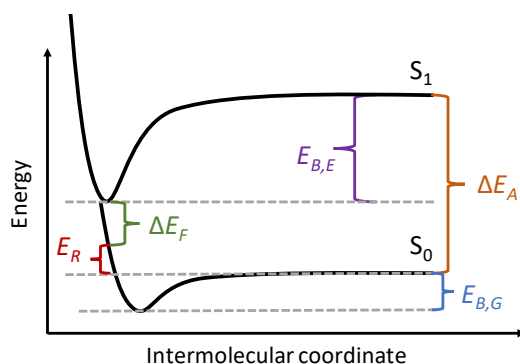


Figure 1.2: Energetic quantities used to describe exciplex formation.

LIF spectra obtained from flames may be decomposed into contributions from PAH monomers and PAH complexes based on known spectroscopic properties for each species. If nonzero contributions to the spectrum are observed for a given species,

then the spectrum is shown to be consistent with the presence of that species. In some cases, the observed spectra may be reproduced by contributions from three to five PAH dimers.[40]

1.3 Study Objectives

To determine whether LIF spectra are consistent with the presence of a specific PAH dimer or complex, accurate information about the photoresponse of the complex is required. Only a few of the PAH complexes that are potentially present in flames have been characterized spectroscopically, many in solution rather than in the gas phase, and theoretical predictions for others have so far been limited to homodimers of PAHs the size of pyrene or smaller.[45, 48, 51–54]

Calculating accurate excited-state binding energies and fluorescence energies for PAH dimers combines two major challenges for theory: accurate description of excited states and accurate treatment of noncovalent interactions. The first goal of this work is to determine which electronic structure methods may be used to treat exciplexes containing the PAHs likely to be present in the largest concentrations in flames (generally agreed to include PAHs the size of coronene and smaller, due to kinetic constraints on the extent of PAH growth[14]). Perturbatively-corrected complete active space self-consistent field (CASSCF) methods have the potential to capture both static and dynamic correlation, yielding highly accurate benchmark results for ground- and excited-state complexes, but the error introduced through choice of basis set for these methods remains poorly understood. We address basis set error for $E_{B,E}$ calculations in Chapter 2, examining the trade-offs involved in calculating accurate benchmark energies.

In Chapter 3 we benchmark single-reference $E_{B,E}$ results for three aromatic exciplexes against perturbatively-corrected multireference binding energies, assessing the performance of several time-dependent density functional theory (TDDFT) exchange-correlation functionals and the second-order algebraic diagrammatic construction method (ADC(2)) and analyzing the character of each excited-state interaction in detail.

Using the TDDFT methods that offer the best accuracy, we then calculate fluorescence emission energies for a large database of PAH complexes, reporting these results in Chapter 4. The relationship between monomer properties and complex emission energy is examined, and several predictive models for emission energy are evaluated. We also examine how the presence of an aliphatic linker between PAH

groups affects emission energy. Finally, we extend this analysis to PAHs containing five-membered rings in Chapter 5, showing how the conformational flexibility of nonaromatic groups leads to unexpected photophysical behavior.

References

- (1) Michelsen, H. A. *Proc. Combust. Inst.* **2017**, *36*, 717–735.
- (2) Di, Q.; Wang, Y.; Zanobetti, A.; Wang, Y.; Koutrakis, P.; Choirat, C.; Dominici, F.; Schwartz, J. D. *N. Engl. J. Med.* **2017**, *376*, 2513–2522.
- (3) Smith, K. R.; Bruce, N.; Balakrishnan, K.; Adair-Rohani, H.; Balmes, J.; Chafe, Z.; Dherani, M.; Hosgood, H. D.; Mehta, S.; Pope, D.; Rehfuess, E. *Annu. Rev. Public Health* **2014**, *35*, 185–206.
- (4) Janssen, N. A.; Hoek, G.; Simic-Lawson, M.; Fischer, P.; van Bree, L.; ten Brink, H.; Keuken, M.; Atkinson, R. W.; Anderson, H. R.; Brunekreef, B.; Cassee, F. R. *Environ. Health Perspect.* **2011**, *119*, 1691–1699.
- (5) Kennedy, I. M. *Proc. Combust. Inst.* **2007**, *31*, 2757–2770.
- (6) Karcher, B. *Survey Geophys.* **1999**, *20*, 113–167.
- (7) McConnell, J. R.; Edwards, R.; Kok, G. L.; Flanner, M. G.; Zender, C. S.; Saltzman, E. S.; Banta, J. R.; Pasteris, D. R.; Carter, M. M.; Kahl, J. D. W. *Science* **2007**, *317*, 1381–1385.
- (8) Hansen, J.; Nazarenko, L. *Proc. Natl. Acad. Sci. USA* **2004**, *101*, 423–428.
- (9) Qian, Y.; Gustafson, W. I.; Leung, L. R.; Ghan, S. J. *J. Geophys. Res. Atmos.* **2009**, *114*, 1–19.
- (10) Law, C. K.; Sung, C. J.; Wang, H.; Lu, T. F. *AIAA J.* **2003**, *41*, 1629–1646.
- (11) Viskanta, R.; Mengüç, M. *Prog. Energy Combust. Sci.* **1987**, *13*, 97–160.
- (12) Stein, S. E.; Fahr, A. *J. Phys. Chem.* **1985**, *89*, 3714–3725.
- (13) Teini, P. D.; Karwat, D. M. A.; Atreya, A. *Combust. Flame* **2011**, *158*, 2045–2055.
- (14) Wang, H. *Proc. Combust. Inst.* **2011**, *33*, 41–67.
- (15) Lighty, J. A. S.; Veranth, J. M.; Sarofim, A. F. *J. Air Waste Manag. Assoc.* **2000**, *50*, 1565–1618.
- (16) Sabbah, H.; Biennier, L.; Klippenstein, S. J.; Sims, I. R.; Rowe, B. R. *J. Phys. Chem. Lett.* **2010**, *1*, 2962–2967.
- (17) Frenklach, M. *Phys. Chem. Chem. Phys.* **2002**, *4*, 2028–2037.
- (18) Totton, T. S.; Misquitta, A. J.; Kraft, M. *Phys. Chem. Chem. Phys.* **2012**, *14*, 4081–94.

- (19) Iavarone, S.; Pascazio, L.; Sirignano, M.; De Candia, A.; Fierro, A.; de Arcangelis, L.; D'Anna, A. *Combust. Theory Model.* **2017**, *21*, 49–61.
- (20) Elvati, P.; Turrentine, K.; Violi, A. **2017**.
- (21) Lowe, J. S.; Lai, J. Y. W.; Elvati, P.; Violi, A. *Proc. Combust. Inst.* **2015**, *35*, 1827–1832.
- (22) Elvati, P.; Violi, A. *Proc. Combust. Inst.* **2013**, *34*, 1837–1843.
- (23) *CRC Handbook of Data on Organic Compounds*, 2nd ed.; Weast, R. C., Grasselli, J. G., Eds.; CRC Press: Boca Raton, FL, 1989.
- (24) Herdman, J. D.; Miller, J. H. *J. Phys. Chem. A* **2008**, *112*, 6249–6256.
- (25) Pascazio, L.; Sirignano, M.; D'Anna, A. *Combust. Flame* **2017**, *185*, 53–62.
- (26) Salenbauch, S.; Cuoci, A.; Frassoldati, A.; Saggese, C.; Faravelli, T.; Hasse, C. *Combust. Flame* **2015**, *162*, 2529–2543.
- (27) Lindstedt, R. P.; Waldheim, B. B. O. *Proc. Combust. Inst.* **2013**, *34*, 1861–1868.
- (28) Kholghy, M. R.; Kelesidis, G. A.; Pratsinis, S. *Phys. Chem. Chem. Phys.* **2018**, *20*, 10926–10938.
- (29) Johansson, K. O.; Head-Gordon, M. P.; Schrader, P. E.; Wilson, K. R.; Michelsen, H. A. *Science* **2018**, *1000*, 997–1000.
- (30) Miller, J. A.; Melius, C. F. *Combust. Flame* **1992**, *91*, 21–39.
- (31) Homann, K.-H. *Angewandte Chemie International Edition* **1998**, *37*, 2434–2451.
- (32) Frenklach, M. *Phys. Chem. Chem. Phys.* **2002**, *4*, 2028–2037.
- (33) D'Alessio, A.; D'Anna, A.; Gambi, G.; Minutolo, P. *J. Aerosol Sci.* **1998**, *29*, 397–409.
- (34) Migliorini, F.; Thomson, K. A.; Smallwood, G. J. *Appl. Phys. B* **Aug. 2011**, *104*, 273–283.
- (35) Adkins, E. M.; Giaccari, J. A.; Miller, J. H. *Proc. Combust. Inst.* **2017**, *36*, 957–964.
- (36) Adkins, E. M.; Miller, J. H. *Phys. Chem. Chem. Phys.* **2015**, *17*, 2686–2695.
- (37) Wood, D. L.; Tauc, J. *Phys. Rev. B* **Apr. 1972**, *5*, 3144–3151.
- (38) Sirignano, M.; Collina, A.; Commodo, M.; Minutolo, P.; D'Anna, A. *Combust. Flame* **2012**, *159*, 1663–1669.
- (39) Smyth, K.; Miller, J. H.; Dorfman, R. C.; Mallard, W. G.; J. S. R. *Combust. Flame* **1985**, *62*, 157–181.

- (40) Mercier, X.; Carrivain, O.; Irimiea, C.; Faccinnetto, A.; Therssen, E. **2019**, 1–37.
- (41) Miller, J. H. *Proc. Combust. Inst.* **2005**, *30*, 1381–1388.
- (42) Takaya, T.; Su, C.; de La Harpe, K.; Crespo-Hernandez, C. E.; Kohler, B. *Proc. Natl. Acad. Sci.* **2008**, *105*, 10285–10290.
- (43) Xia, J.; Sanders, S. N.; Cheng, W.; Low, J. Z.; Liu, J.; Campos, L. M.; Sun, T. *Adv. Mater.* **2017**, *29*, 1601652.
- (44) Casanova, D. *J. Chem. Theory Comput.* **2015**, *11*, 2642–2650.
- (45) Shirai, S.; Kurashige, Y.; Yanai, T. *J. Chem. Theory Comput.* **2016**, *12*, 2366–2372.
- (46) Krueger, R. A.; Blanquart, G. *J. Phys. Chem. A* **2019**, *123*, 1796–1806.
- (47) Krueger, R. A.; Blanquart, G. *Int. J. Quantum Chem.* **2019**, *119*, e25819.
- (48) Diri, K.; Krylov, A. I. *J. Phys. Chem. A* **2012**, *116*, 653–662.
- (49) Kasha, M. *Disc. Faraday Soc* **1950**, *9*, 9–14.
- (50) Birks, J. B., *Photophysics of Aromatic Molecules*; Wiley – Interscience: New York, 1970.
- (51) Hoche, J.; Schmitt, H.-C.; Humeniuk, A.; Fischer, I.; Ro, M. I. S. *Phys. Chem. Chem. Phys.* **2017**, *19*, 25002–25015.
- (52) Huenerbein, R.; Grimme, S. *Chem. Phys.* **2008**, *343*, 362–371.
- (53) Kołaski, M.; Arunkumar, C. R.; Kim, K. S. *J. Chem. Theory Comput.* **2013**, *9*, 847–856.
- (54) Shirai, S.; Iwata, S.; Tani, T.; Inagaki, S. *J. Phys. Chem. A* **2011**, *115*, 7687–7699.

MULTIREFERENCE EXCIPLEX BINDING ENERGIES: BASIS SET CONVERGENCE AND ERROR

Copyright 2018 Wiley. Used with permission from Krueger, R. A.; Blanquart, G. *Int. J. Quantum Chem.* **2019**, *119*, e25819.

2.1 Introduction

Exciplex stabilization is fundamentally a noncovalent interaction, and thus binding energy calculations are prey to the same errors that plague calculations involving van der Waals or hydrogen bond interactions. The well-known failure of most DFT functionals to account for stabilizing dispersion interactions can contribute to severe underestimation of exciplex binding energies when corrections are not included.[2] Further errors can be attributed to basis set effects. Basis sets that are too small may destabilize complexes by failing to properly describe the intermolecular electron density, resulting in basis set incompleteness error (BSIE) that will not be canceled by similar error for the infinitely separated monomers. Monomers in a complex may also “borrow” extra basis functions from other monomers, lowering the energy of the complex relative to the infinitely separated monomers. This effect is described as basis set superposition error (BSSE).

The counterpoise (CP) correction of Boys and Bernardi[3] is commonly applied to decrease the effect of BSSE on calculated binding energies. Less-expensive alternatives have been discussed in a recent review.[4] In some cases BSSE may balance other sources of error, making uncorrected energies closer to the complete basis set (CBS) limit,[5, 6] but it has been noted that, even for calculations performed using a single method, the contribution of BSSE to total error varies significantly between complexes.[4]

Perturbatively-corrected complete active space methods, such as second-order complete active space perturbation theory CASPT2[7] and second-order n-electron valence perturbation theory (NEVPT2),[8] have the potential to address the problem of describing the excited states encountered in exciplexes. They have successfully captured the static and dynamic correlation involved valence excitations of acene monomers[9–11] and dimers.[2, 12, 13] Exponential scaling with active space size

has limited multireference perturbation theory approaches to small molecules, but it is likely that increased computing power and the possibility of achieving lower scaling using techniques such as the density matrix renormalization group (DMRG) approach[14–16] will allow these computational methods to be used in increasingly larger systems, including noncovalently-bound dimers and supramolecular complexes.

Thus, it will become increasingly necessary to understand the mixture of basis set error involved in perturbatively-corrected CASSCF descriptions of noncovalent interactions. CASPT2 excitation energies have been calculated using both the TZVP and aug-cc-pVTZ basis sets for a database of small molecules,[17] and the performance of basis sets of different sizes and families for excited state energies and wave function descriptors of tetracene has been assessed.[10] Basis set effects on the excited state *noncovalent* interactions of aromatics, though, have not been examined in detail; studies have been limited to a single atomic natural orbital basis[12, 13] or to double- and triple-zeta basis sets without diffuse functions.[2] No studies of aromatic excimer or exciplex interactions have reported results from basis sets of quadruple-zeta quality or higher, and the effects of diffuse functions on description of noncovalent interactions have not been systematically examined. An NEVPT2 investigation of the ground state interaction between Cr atoms using the cc-pwVNZC-DK basis set family[18] revealed a difference in binding energy of nearly 50% between $N = 3$ and $N = 5$ despite the large size of both basis sets,[19] hinting at high basis set sensitivity for interaction energies even beyond the double-zeta level.

A benchmark of basis set effects for a large database of exciplexes is beyond the scope of this work. However, as a first step towards the goal of establishing best practices for basis set usage in perturbatively-corrected CASSCF binding energy calculations, we have chosen to analyze the effects of basis set size and quality on the binding energies of three test exciplexes, computing estimated CBS binding energies for each.

The first complex considered is the benzene excimer (BzBz)*, which has been the subject of several CASPT2 and coupled cluster studies[12, 13, 20, 21] that provide points of comparison. Experimental estimates of binding energy have also been reported.[22, 23] The other two complexes represent exciplexes that remain theoretically and experimentally uncharacterized: the *cis*-butadiene–benzene exciplex (BdBz)* and the benzene–naphthalene exciplex (BzNa)*. The *cis*-butadiene–

naphthalene exciplex has been examined using Hückel theory,[24] and it has been suggested that the *cis*-butadiene–anthracene exciplex represents an intermediate in the photocycloaddition involving the two molecules.[25] Nonetheless, (BdBz)*, the smallest diene-aromatic exciplex, has not been investigated in any work to date. Similarly, while the benzene and naphthalene excimers represent important benchmark systems for excited state electronic structure methods, the spectroscopic parameters for (BzNa)* and the degree of excited state stabilization remain unknown.

2.2 Computational Methods

All calculations have been performed using the CASSCF method with energies perturbatively corrected using the NEVPT2 approach. The form of the NEVPT2 Hamiltonian prevents intruder state mixing,[8] a source of error in CASPT2 calculations that must be corrected through the use of shift parameters. Optimal CASPT2 shift parameters have been shown to vary based on system size and basis set,[26] making the use of a fixed parameter set particularly undesirable in this work. When shift parameters are used in CASPT2 calculations, though, vertical excitation energies computed using the CASPT2 and NEVPT2 schemes are generally similar,[27] so the conclusions drawn in this work can likely be generalized to CASPT2 descriptions of exciplex binding.

To characterize the valence $\pi \rightarrow \pi^*$ excitations considered for each complex, active spaces consisting of one 2pz orbital per C atom, where the z-axis is normal to the molecule, were chosen. One active electron was included for each active orbital. The use of smaller active spaces results in incorrect L_a – L_b state ordering for the naphthalene excimer compared with the full valence π active space.[2]

For (BzNa)*, this procedure results in a 16 electron–16 orbital active space, which lies at or beyond the limits of conventional CASSCF/NEVPT2 techniques. To overcome this scaling challenge, the polynomial-scaling DMRG approach[14–16, 28, 29] has been used in both CASSCF and NEVPT2 calculations. The DMRG method uses an approximate wave function ansatz known as a matrix product state (MPS) in which the wave function is built from a series of $M \times M$ matrices. M , known as the MPS bond dimension, controls the accuracy of the wave function through the number of variational parameters, which scales as M^2 . The energy is variationally optimized with respect to one matrix at a time.[29]

DMRG calculations have been performed using the PySCF framework version 1.3b,[30] which provides an interface to the Block DMRG solver version 1.5.0.[28]

Restricted Hartree-Fock calculations were performed to obtain canonical starting orbitals, with active 2pz orbitals selected using the atomic valence active space (AVAS) technique.[31] Following CASSCF orbital optimization with $M = 500$, a subsequent complete active space configuration interaction (CASCI) calculation was performed with $M = 1200$ to refine the coefficients for each configuration. Each DMRG calculation involves a series of MPS optimizations with increasing values of M up to the specified maximum value. The default optimization schedule was used in every calculation. All DMRG NEVPT2 calculations were of the strongly contracted type, and the compress approximation[19] was used. M was also set to 1200 for all NEVPT2 calculations.

It should be noted that the choice of starting orbital type, e.g., canonical, localized, or split-localized, can affect the convergence of DMRG energies with increasing M . [29] Benchmark calculations performed for the (BzNa)* system (Table 2.1) show that for a given set of M values, binding energies calculated using canonical orbitals are approximately 1 kJ/mol higher than the ones obtained using localized starting orbitals, mostly due to differences in the absolute energies of the dimer with $r_z = r_0$. For canonical starting orbitals, setting $M = 500$ for CASSCF and $M = 1200$ for CASCI and NEVPT2 yields a binding energy approximately 0.5 kJ/mol lower than the apparent large- M limiting value. Choosing canonical starting orbitals and $M = 500$ and $M = 1200$ for CASSCF and CASCI/NEVPT2 calculations, respectively, represented a reasonable compromise between accuracy and computational cost.

Table 2.1: NEVPT2 binding energies for (BzNa)* in the S_1 state with different starting orbital types and M values. The aug-cc-pVTZ basis was used in all calculations.

Orbital Type	CASSCF M	CASCI/NEVPT2 M	$ E_{Min} $ (kJ/mol)	$ E_{Ref} $ (kJ/mol)	E_B (kJ/mol)
Local	500	1200	1619828.8	1619790.5	38.3
Local	800	1800	1619829.4	1619790.1	39.3
Local	1000	2250	1619829.4	1619790.1	39.3
Canonical	300	900	1619829.8	1619790.1	39.7
Canonical	500	1200	1619830.0	1619790.1	39.9
Canonical	800	1800	1619830.4	1619790.0	40.4
Canonical	1000	2250	1619830.4	1619790.1	40.3

Eclipsed configurations, with the planes of the molecules parallel and C atoms directly overlapping, have been shown to be the minimum-energy configurations for

S_1 acene excimers.[20, 32–34] An eclipsed configuration has been chosen for all $(\text{BzBz})^*$ calculations in this work, and configurations closely resembling the eclipsed configuration have been chosen for $(\text{BdBz})^*$ and $(\text{BzNa})^*$ (Fig. 2.1). Monomer geometries have been optimized in the ground state using density functional theory (DFT) with the B3LYP functional,[35] including Grimme’s D3 dispersion correction,[36] and the def2-TZVP basis set.[37] DFT calculations were carried out using the ORCA software package[38] version 4.0.0.

The internal coordinates of each monomer have been frozen at their ground state values for all S_1 state calculations. The r_0 intermolecular separation used for each exciplex is the r_0 value obtained from a CASSCF/NEVPT2 scan of the intermolecular coordinate r_z performed using the aug-cc-pVTZ basis set without CP correction. Scans of r_z performed for $(\text{BzBz})^*$ using both the def2-TZVP and aug-cc-pVTZ basis sets show that r_0 differs by only 0.04 Å. Because energies change slowly with r_z in the vicinity of r_0 , the energies for both r_0 values calculated using a given basis set are very similar. The variation in r_0 between basis sets is more pronounced for $(\text{BzNa})^*$, but aug-cc-pVTZ r_0 value of 3.15 Å represents a midpoint between the def2-TZVP and aug-cc-pVDZ results. The interaction energy for each system is negligible for $r_z > 7$ Å, so r_z is set to 10 Å to obtain the infinitely separated complex energy. Only S_1 binding energies are considered, so for simplicity, $E_{B,E}$ will be shortened to E_B .

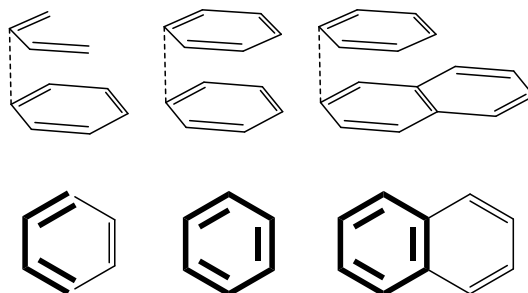


Figure 2.1: Eclipsed geometries from side and top perspectives for $(\text{BdBz})^*$ (left), $(\text{BzBz})^*$ (center), and $(\text{BzNa})^*$ (right). The intermolecular coordinate r_z is marked with a dotted line.

The basis sets considered in this work include members of Dunning and coworkers’ commonly-used cc-pVNZ family, where $N = \text{D, T, Q, 5}$. [39] The aug-cc-pVNZ basis set family, obtained by adding diffuse functions to the cc-pVNZ basis sets,[40] is also considered. For simplicity, the cardinality of double-, triple-, and quadruple-zeta basis sets will be indicated with $N = 2, 3,$ and $4,$ respectively. The aug-cc-

pVTZ basis has been used as the reference basis set in existing CASPT2 basis set benchmarks.[10, 17]

An important objective of this work, though, is to explore the diffuse function space beyond the cc-pVNZ and aug-cc-pVNZ basis set families. Diffuse functions are frequently recommended for calculations involving noncovalent interactions performed using wave function theories. Truhlar and coworkers have argued, though, that for a range of chemical problems including noncovalent interaction energy, the number of diffuse functions provided by the aug-cc-pVNZ family is not necessary. In fact, the choice to decrease basis set cardinality—valence space size—in order to add a full complement of diffuse functions may lead to poor results due high BSSE. BSSE is expected to approach zero in the CBS limit, but the aug-cc-pVDZ and aug-cc-pVTZ basis sets remain far from this limit, and increasing basis set size with diffuse functions does not a priori guarantee lower BSSE or total error.[41, 42]

Avoiding unnecessarily large basis sets is desirable for every *ab initio* method, but it is particularly critical for the DMRG-NEVPT2 method, which in practice requires calculation of the fourth-order reduced density matrix on the fly. This means that the NEVPT2 step has much higher memory requirements than the CASSCF/CASCI calculations used to generate the multiconfigurational wave function.[43]

The calendar basis sets[41] are convergent, correlation-consistent basis set families with systematically varying numbers of diffuse functions. The largest family, jul-cc-pV(N+d)Z, is simply the aug-cc-pVNZ family with diffuse functions removed from H atoms. Removing a diffuse subshell from each heavier atom yields the jun- family, and repeating the procedure yields the may- and then the apr- families. The basis sets generated in this manner include the “minimally augmented” maug-cc-pVNZ family previously proposed.[41, 42]

Within the cc-pVNZ family, the lowest basis function exponents decrease with increasing cardinality, which means that even without the addition of diffuse functions, basis sets become more diffuse. The calendar basis sets maintain a minimum level of diffuseness by providing low-cardinality basis sets only for the more augmented basis set families. This means that the jun- and jul- basis sets are provided for N= 2, 3, 4, the may- basis sets for N= 3, 4, and the apr- basis set for N = 4.[41] Because extrapolation of binding energies to obtain the CBS limit is of primary importance, we have chosen to consider the basis set families for which N = 2, 3, 4 are all available. The prohibitively large aug-cc-pVQZ basis set has only been used for the smallest system, (BdBz)*, and the jul-cc-pV(Q+d)Z basis set has been omitted

for the largest system, (BzNa)*.

2.3 Results and Discussion

The Benzene Excimer

Our analysis begins with the benzene excimer, the best-characterized of the systems considered here. Both CP-corrected and uncorrected binding energies have been computed using each basis set (Table 2.2). An r_0 value of 2.88 Å was used.

The convergence of uncorrected E_B values with increasing basis set cardinality N varies widely among the basis set families considered (Fig. 2.2). For the least-diffuse basis set families, cc-pVNZ and jun-cc-pV(N+d)Z, E_B varies non-monotonically with N . This variation is likely the result of the shifting balance between BSIE and BSSE, with BSIE dominating at $N = 2$ and yielding low energies relative to the CBS limit for each basis set. In contrast, E_B decreases monotonically for the more diffuse jul-cc-pV(N+d)Z and aug-cc-pVNZ basis sets, suggesting that the basis set error is dominated by BSSE, which decreases as the basis sets for each monomer approach the CBS limit. The aug-cc-pVTZ and jul-cc-pV(N+d)Z values converge at $N = 3$, and the jun- and jul-cc-pV(N+d)Z converge at $N = 4$.

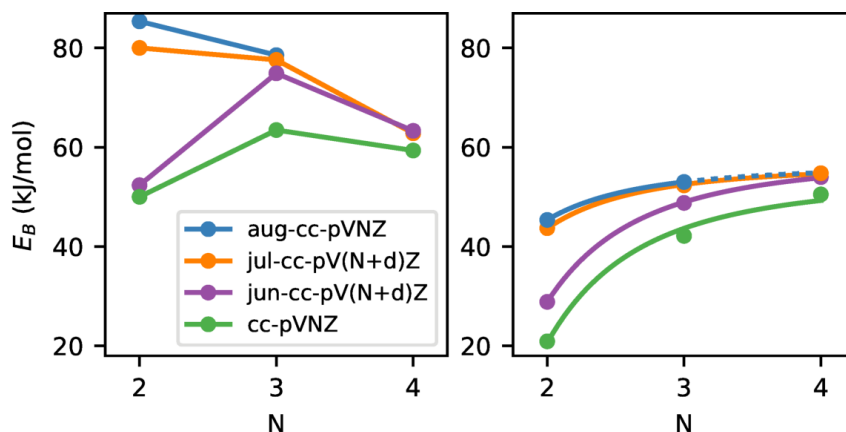


Figure 2.2: (BzBz)* binding energy values as a function of basis set cardinality N . Uncorrected E_B values are shown on the left, with connecting lines added to guide the eye. CP-corrected values $E_{B,CP}$ are shown on the right, with best-fit $N = 2, 3, 4$ N^{-3} curves shown. The dotted line indicates extrapolation from the $N = 2, 3$ fit.

CP-corrected E_B values ($E_{B,CP}$), on the other hand, increase monotonically with increasing N for every basis set family. The jul-cc-pV(N+d)Z and aug-cc-pVNZ basis set families are in extremely good agreement for $N = 2, 3$ and converge quickly toward their apparent CBS limits. The monotonicity of the $E_{B,CP}$ allows

Table 2.2: Binding energies E_B and counterpoise corrected binding energies $E_{B,CP}$ for the exciplexes. All energies are calculated at the NEVPT2 level and reported in kJ/mol.

Basis Set	(BdBz)*			(BzBz)*			(BzNa)*		
	E_B	$E_{B,CP}$	%CPC	E_B	$E_{B,CP}$	%CPC	E_B	$E_{B,CP}$	%CPC
cc-pVDZ	8.7	-8.0	209	50.0	20.9	139	18.0	-6.4	381
cc-pVTZ	14.8	2.6	469	63.5	42.1	50	27.0	7.3	270
cc-pVQZ	12.2	7.0	74	59.3	50.5	17	20.3	13.2	54
jun-cc-pVDZ	11.4	-2.3	596	52.4	28.9	81	24.5	1.2	1942
jun-cc-pVTZ	20.2	7.0	189	74.9	48.8	53	37.5	13.8	171
jun-cc-pVQZ	14.9	9.6	55	63.3	54.0	17	24.7	16.9	46
jul-cc-pVDZ	27.2	3.8	616	80.0	43.7	83	41.6	11.0	278
jul-cc-pVTZ	22.8	9.4	143	77.6	52.3	48	37.5	15.5	142
jul-cc-pVQZ	14.6	10.1	45	62.8	54.8	15	–	–	–
aug-cc-pVDZ	28.9	7.5	285	85.3	45.4	88	44.4	11.9	270
aug-cc-pVTZ	23.5	9.3	153	78.5	53.0	48	39.5	16.0	147
aug-cc-pVQZ	15.5	10.4	49	–	–	–	–	–	–

straightforward fitting and extrapolation to the CBS limit. Functions of the form

$$E_B = E_{B,CBS} + aN^{-3} \quad (2.1)$$

have been used. Two-parameter N^{-3} expressions are frequently used to extrapolate correlation energies calculated using correlation-consistent basis sets, while exponential functions are favored for Hartree-Fock or multiconfigurational SCF energies. Variations such as $(N + c)^{-3}$ are also common choices for correlation energies.[44–47] The physical rationale for these choices has been discussed by Varandas.[48]

The $E_{B,CP}$ results reported reflect both the MCSCF energy and the NEVPT2 correlation values. Nonetheless, the three-point fits performed using Eq. 2.1 match the data generated using the jun- and jul-cc-pV(N+d)Z and the aug-cc-pVNZ basis sets extremely well. This is unsurprising, given that an NEVPT2 dynamic correlation correction is required to observe an attractive binding interaction for the benzene excimer. Without the correction, CASSCF/CASCI results show no monomer interaction for $r_z > 4.5 \text{ \AA}$ and a repulsive interaction for $r_z < 4.5 \text{ \AA}$. The same pattern has been observed for the naphthalene excimer.[2]

Comparing the $E_{B,CBS}$ values obtained from two- and three-point N^{-3} extrapolations (Table 2.3), the jun- and jul-cc-pV(N+d)Z and the aug-cc-pVNZ estimates have a mean of 56.8 kJ/mol, and all fall within ± 1.0 kJ/mol of this mean. For each basis set family, two-point results using $N = 2, 3$ match three-point fit results

closely, while two-point fits using $N = 3, 4$ yield $E_{B,CBS}$ values that are slightly more binding. Differences between $E_{B,CBS}$ values extrapolated from cc-pVNZ results are significantly larger. The $E_{B,CBS}$ value obtained using $N = 3, 4$ is in excellent agreement with the corresponding jul-cc-pV(N+d)Z result, but the high error associated with the CP-corrected cc-pVDZ binding energy skews the $N = 2, 3$ and $N = 2, 3, 4$ results.

Table 2.3: Extrapolated complete basis set counterpoise-corrected binding energies using $E_{B,CP}$ values from $N = 2, 3$, $N = 3, 4$, and $N = 2, 3, 4$. Reference values for each system appear in boldface.

Basis Set Family	(BdBz)*			(BzBz)*			(BzNa)*		
	$N = 2, 3$	$N = 3, 4$	$N = 2, 3, 4$	$N = 2, 3$	$N = 3, 4$	$N = 2, 3, 4$	$N = 2, 3$	$N = 3, 4$	$N = 2, 3, 4$
cc-pVNZ	0.3	10.2	4.4	51.0	56.6	53.4	13.1	17.5	14.9
jun-cc-pVNZ	10.9	11.5	11.1	57.2	57.8	57.4	19.1	19.2	19.1
jul-cc-pVNZ	11.7	10.6	11.2	55.9	56.6	56.2	17.44	–	–
aug-cc-pVNZ	10.1	11.1	10.5	56.2	–	–	17.7	–	–

In principle, the $E_{B,CBS}$ values obtained for $N = 3, 4$ for the most diffuse basis set family available minimize both BSSE and BSIE, so we take this result as the reference for each system. To account for the remaining error, we take the difference between this $E_{B,CBS}$ and the one obtained for the second-most diffuse basis set family to be the uncertainty associated with the reference value. For (BzBz)*, this procedure yields a reference $E_{B,CBS}$ of 56.6 ± 1.2 kJ/mol, an uncertainty of approximately 2%. The absolute deviation from the reference value $\Delta E_{B,Abs}$ (Fig. 2.3) and the deviation relative to the converged CBS limit, $\Delta E_{B,Rel}$, may be used to estimate the error associated with each E_B and $E_{B,CP}$ value. To assess the trade-off between accuracy and computational expense, the number of contracted basis functions (N_{CBF}) in each basis set is used as a rough proxy for the cost of the calculation in terms of time, memory, and storage.

For uncorrected results at the double-zeta level, the cc-pVNZ and jun-cc-pV(N+d)Z basis sets provide surprisingly low E_B error at low cost, likely due to fortuitous BSIE and BSSE error cancellation. Increasing diffuseness is associated with increasing error, suggesting that BSIE and BSSE do not decrease at the same rate. At the quadruple-zeta level in particular, forgoing added diffuse functions decreases error and results in significant cost savings. This variation reflects the high basis set sensitivity of CASSCF/NEVPT2 binding energies—a careless choice of the aug-cc-pVDZ basis set results in an E_B value 50% greater than the reference $E_{B,CBS}$.

Absolute errors in $E_{B,CP}$, though, vary monotonically with basis set size within

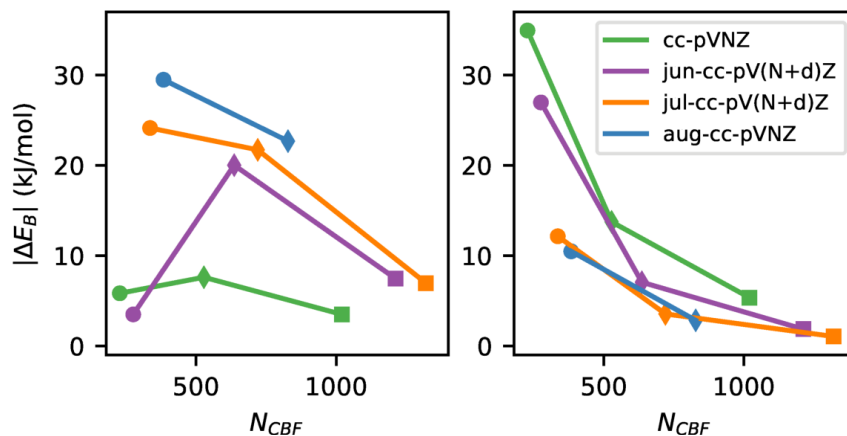


Figure 2.3: (BzBz)* absolute binding energy error values $|\Delta E_B|$ as a function of the number of contracted basis functions in each set for uncorrected E_B values (left) and for $E_{B,CP}$ values (right). Error represents the deviation from the CBS limit obtained by extrapolating CP-corrected $N = 3, 4$ jul-cc-pV(N+d)Z values using an N^{-3} fit. Double-, triple-, and quadruple-zeta basis set results are marked with circles, diamonds, and squares, respectively.

each basis set family. Using the jul-cc-pVDZ basis set rather than the jun-cc-pVDZ basis set improves E_B results by more than a factor of two with little additional cost. The benefits of additional diffuse functions decrease as N increases. The poor performance of the CP-corrected cc-pVDZ basis set is associated with a large relative CP correction. Following Papajak and coworkers,[42] we define %CPC as

$$\%CPC = 100 \times \frac{|E_B - E_{B,CP}|}{|E_{B,CP}|}. \quad (2.2)$$

With the exception of the cc-pVDZ basis set, with %CPC = 138, %CPC remains approximately constant with respect to diffuseness for fixed N , with %CPC ≈ 80 for $N = 2$ and decreasing to %CPC ≈ 50 and 15 for $N = 3$ and 4, respectively (Table 2.2). This indicates that relative size of the correction alone is not a sufficient criterion for determining the quality of the result.

Our reference $E_{B,CBS}$ value of 56.6 kJ/mol is markedly higher than reported experimental values, the most recent of which range from 33–35 kJ/mol.[22, 23] Several factors make direct comparison of calculated 0 K gas phase binding energies to experimental binding energies difficult. Obtaining E_B values for $T = 0$ K from finite-temperature measurements requires determining the relationship between excimer lifetime and temperature to a high degree of accuracy. Solvent effects on binding energy are also difficult to predict. Previous CASPT2 predictions of $E_{B,CP}$ based on single moderately-sized ANO basis sets range from 41–51 kJ/mol,[12, 13]

in good agreement with our results from moderately diffuse basis sets with $N = 2-3$, despite differences in the monomer geometries used in each study.

The Butadiene-Benzene Exciplex

The butadiene-benzene exciplex (BdBz)* that we label S_1 originates from the benzene monomer S_1 state, as the first singlet excitation energy is lower for the benzene monomer than for the butadiene monomer. It allows us to consider basis set effects on a weaker exciplex interaction that involves a non-aromatic molecule. Binding energies have been computed using $r_0 = 3.1 \text{ \AA}$. Trends for uncorrected E_B values (Table 2.2 and Fig. 2.4) are similar to the ones observed for (BzBz)*. The less-diffuse cc-pVNZ and jun-cc-pV(N+d)Z E_B values have a maximum at $N = 3$, while the more-diffuse aug-cc-pVNZ and jul-cc-pV(N+d)Z basis set energies decrease monotonically with increasing N . E_B values for the latter have converged by $N = 3$, with the jun-cc-pV(N+d)Z basis set matching the more diffuse ones for $N = 4$.

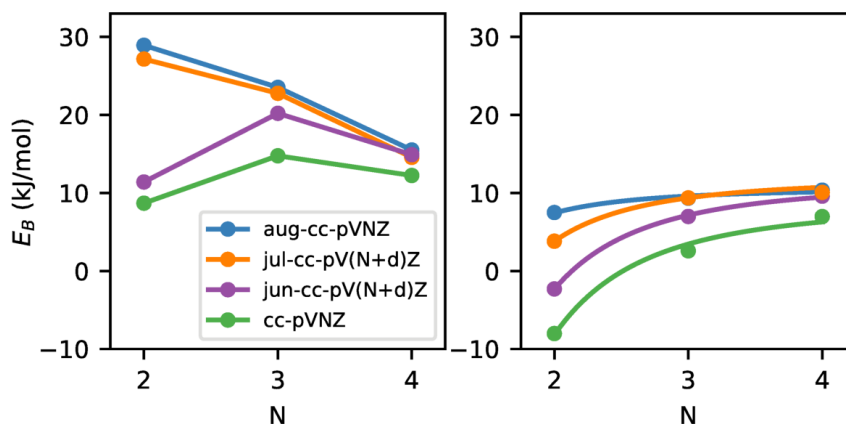


Figure 2.4: (BdBz)* E_B and $E_{B,CP}$ values as a function of basis set cardinality N . Uncorrected values are shown on the left, with connecting lines added to guide the eye. CP-corrected values are shown on the right, with best-fit $N = 2, 3, 4 N^{-3}$ curves added.

As with (BzBz)*, $E_{B,CP}$ values increase monotonically toward $E_{B,CBS}$ for each basis set. The most accurate result for $E_{B,CBS}$ is 11.1 kJ/mol, obtained using an $N = 3, 4$ fit for the aug-cc-pVNZ basis, with an uncertainty of ± 0.5 kJ/mol based on the difference between the aug-cc-pVNZ reference and the jul-cc-pV(N+d)Z $N = 3, 4$ $E_{B,CBS}$. This uncertainty amounts to approximately 5% of the reference value.

Large counterpoise corrections for the double-zeta cc-pVNZ and jun-cc-pV(N+d)Z basis sets yield repulsive $E_{B,CBS}$ values—a qualitatively incorrect result. Indeed, %CPC values in excess of 200 make the appropriateness of the term “correction”

questionable. Nonetheless, an N^{-3} fit describes the $E_{B,CP}$ results extremely well, and a fit based on the relatively inexpensive double- and triple-zeta jun-cc-pV(N+d)Z basis sets is sufficient to obtain a $E_{B,CBS}$ value just 0.2 kJ/mol away from the aug-cc-pVNZ $N = 3, 4$ reference $E_{B,CBS}$. For the cc-pVNZ family, quality of the $N = 2, 3$ and $N = 2, 3, 4$ $E_{B,CBS}$ results is extremely poor. Both are less than half the reference value. The $N = 3, 4$ $E_{B,CBS}$ value, on the other hand, comes within 10% of the reference value.

Once again, the highest absolute error values (Fig. 2.5) are observed for the aug-cc-pVDZ E_B and the cc-pVDZ $E_{B,CP}$, while cancellation of error results in an excellent jun-cc-pV(D+d)Z E_B value. The $E_{B,CBS}$ values obtained from each basis set family leave no doubt that this complex is stabilized by an exciplex interaction in the excited state, with binding energies greater than the ones obtained for the benzene dimer, a larger complex, in the ground state (≈ 10 kJ/mol).[49]

Several E_B and $E_{B,CP}$ values differ from the reference by more than 100%, the highest relative error values obtained for any complex. For the more diffuse double- and triple-zeta basis sets, BSSE is likely the culprit. Indeed, the asymmetry of the complex may contribute to high BSSE. The number of “extra” basis functions available to each monomer is different, and sensitivity of each monomer’s energy to extra basis functions may differ as well.

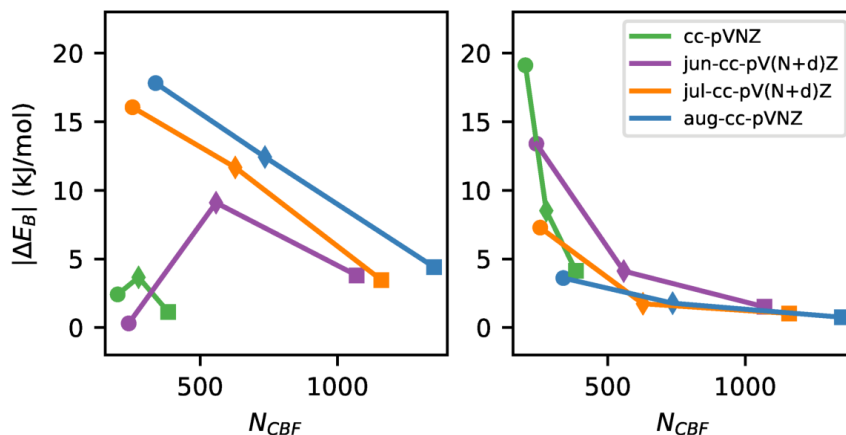


Figure 2.5: (BdBz)* absolute binding energy error values $|\Delta E_B|$ as a function of the number of contracted basis functions in each set for uncorrected E_B values (left) and for $E_{B,CP}$ values (right). Error represents the deviation from the CBS limit obtained by extrapolating CP-corrected $N = 3, 4$ aug-cc-pVNZ values using an N^{-3} fit. Double-, triple-, and quadruple-zeta basis set results are marked with circles, diamonds, and squares, respectively.

The Benzene-Naphthalene Exciplex

Originating from the S_1 excitation of the naphthalene monomer, the $(\text{BzNa})^*$ exciplex interaction is weak compared with the one observed for $(\text{BzBz})^*$. With $r_0 = 3.15$ Å obtained from the CASSCF/NEVPT2 aug-cc-pVTZ intermolecular coordinate scan, it also has the largest optimal intermolecular separation of the exciplexes considered here. The trends observed in E_B and E_{CP} nonetheless remain remarkably consistent (Fig. 2.6). Convergence of E_B values obtained using the cc-pVNZ and jun-cc-pV(N+d)Z basis sets is non-monotonic, while $E_{B,CP}$ values for every basis set converge smoothly toward $E_{B,CBS}$. CP corrections for double-zeta basis sets are extravagantly large, approaching 2000% for the jun-cc-pV(D+d)Z basis set (Table 2.2). This disparity reflects the large error in $E_{B,CP}$ values obtained for the less diffuse double-zeta basis sets (Fig. 2.7). As in the case of $(\text{BdBz})^*$, the cc-pVDZ $E_{B,CP}$ is even repulsive.

The $N = 3, 4 N^{-3}$ fit obtained from the jun-cc-pV(N+d)Z basis sets yields a reference $E_{B,CBS}$ of 19.2 kJ/mol, with an uncertainty of 1.7 kJ/mol amounting to approximately 9% of the reference. Based on the behavior of the other two complexes, we can predict that the $E_{B,CBS}$ that would be obtained from $N = 3, 4$ extrapolations for the more diffuse jul-cc-pV(N+d)Z and aug-cc-pVNZ basis sets is likely to be 1-2 kJ/mol lower than the reference.

$E_{B,CBS}$ values obtained for $(\text{BzNa})^*$ are more than 50% lower than the reference $E_{B,CBS}$ for the smaller $(\text{BzBz})^*$ complex. Such weak exciplex binding presents a sharp contrast with ground state aromatic interaction energy trends, which show binding energies scaling roughly linearly with the molecular weight.[50, 51]

References

- (1) Krueger, R. A.; Blanquart, G. *Int. J. Quantum Chem.* **2019**, *119*, e25819.
- (2) Shirai, S.; Kurashige, Y.; Yanai, T. *J. Chem. Theory Comput.* **2016**, *12*, 2366–2372.
- (3) Van Duijneveldt, F. B.; van Duijneveldt-van de Rijdt, J. G. C. M.; van Lenthe, J. H. *Chem. Rev.* **1994**, *94*, 1873–1885.
- (4) Sure, R.; Brandenburg, J. G.; Grimme, S. *ChemistryOpen* **2016**, *5*, 94–109.
- (5) Mentel, L. M.; Baerends, E. J. *J. Chem. Theory Comput.* **2014**, *10*, 252–267.
- (6) Sheng, X. W.; Mentel, L.; Gritsenko, O. V.; Baerends, E. J. *J. Comput. Chem.* **2011**, *32*, 2896–2901.

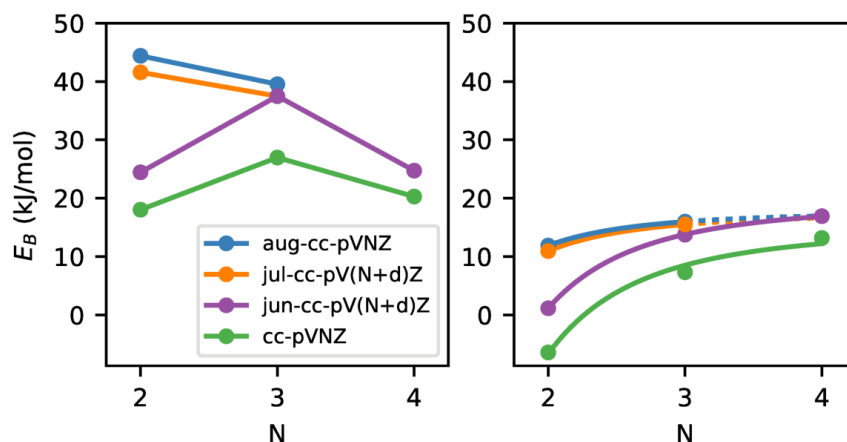


Figure 2.6: (BzNa)* E_B and $E_{B,CP}$ values as a function of basis set cardinality N . Uncorrected values are shown on the left, with connecting lines added to guide the eye. CP-corrected values are shown on the right, with best-fit $N = 2, 3, 4 N^{-3}$ curves added.

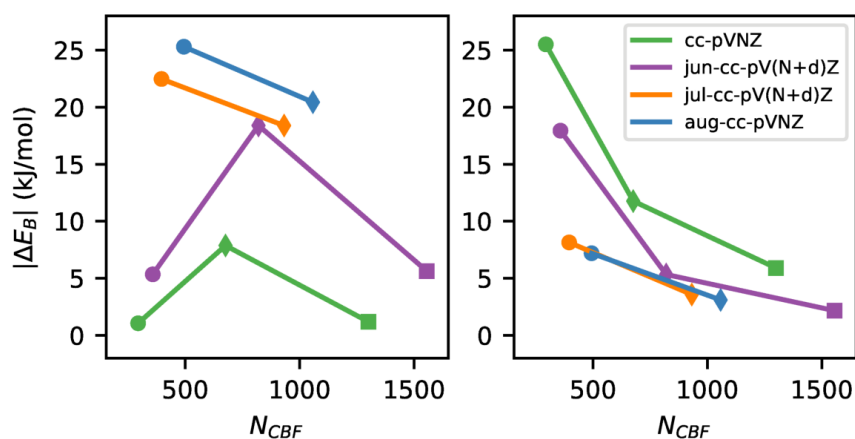


Figure 2.7: (BzNa)* absolute binding energy error values $|\Delta E_B|$ as a function of the number of contracted basis functions in each set for uncorrected E_B values (left) and for $E_{B,CP}$ values (right). Error represents the deviation from the CBS limit obtained by extrapolating CP-corrected $N = 3, 4$ jun-cc-pV(N+d)Z values using an N^{-3} fit. Double-, triple-, and quadruple-zeta basis set results are marked with circles, diamonds, and squares, respectively.

- (7) Andersson, K.; Malmqvist, P.-Å.; Roos, B. O. *J. Chem. Phys.* **1992**, *96*, 1218–1226.
- (8) Angeli, C.; Cimiraglia, R.; Evangelisti, S.; Leininger, T.; Malrieu, J. P. *J. Chem. Phys.* **2001**, *114*, 10252.
- (9) Bettanin, F.; Ferrão, L. F.; Pinheiro, M.; Aquino, A. J.; Lischka, H.; Machado, F. B.; Nachtigallova, D. *J. Chem. Theory Comput.* **2017**, *13*, 4297–4306.

- (10) Plasser, F.; Mewes, S. A.; Dreuw, A.; González, L. *J. Chem. Theory Comput.* **2017**, *13*, 5343–5353.
- (11) Rubio, M.; Merchán, M.; Ortí, E.; Roos, B. O. *Chem. Phys.* **1994**, *179*, 395–409.
- (12) Jara-Cortés, J.; Rocha-Rinza, T.; Hernández-Trujillo, J. *Comput. Theor. Chem.* **2015**, *1053*, 220–228.
- (13) Rocha-Rinza, T.; Vico, L. D.; Veryazov, V.; Roos, O. *Chem. Phys. Lett.* **2006**, *426*, 268–272.
- (14) Chan, G. K.-L.; Keselman, A.; Nakatani, N.; Li, Z.; White, S. R. *J. Chem. Phys.* **2016**, *014102*, 014102.
- (15) Chan, G. K.-L.; Dorando, J. J.; Ghosh, D.; Hachmann, J.; Neuscamman, E.; Wang, H.; Yanai, T. In *Frontiers in Quantum Systems in Chemistry and Physics*, Wilson, S., Grout, P. J., Maruani, J., Delgado-Barrio, G., Piecuch, P., Eds.; Springer Netherlands: Dordrecht, 2008, pp 49–65.
- (16) Chan, G. K. L.; Head-Gordon, M. *J. Chem. Phys.* **2002**, *116*, 4462–4476.
- (17) Silva-Junior, M. R.; Schreiber, M.; Sauer, S. P. A.; Thiel, W. *J. Chem. Phys.* **2010**, *133*, 174318.
- (18) Balabanov, N. B.; Peterson, K. A. *J. Chem. Phys.* **2005**, *123*, 064107.
- (19) Guo, S.; Watson, M. A.; Hu, W.; Sun, Q.; Chan, G. K. L. *J. Chem. Theory Comput.* **2016**, *12*, 1583–1591.
- (20) Iyer, E. S. S.; Sadybekov, A.; Lioubashevski, O.; Krylov, A. I.; Ruhman, S. *J. Phys. Chem. A* **2017**, *121*, 1962–1975.
- (21) Diri, K.; Krylov, A. I. *J. Phys. Chem. A* **2012**, *116*, 653–662.
- (22) Cundall, R. B.; Ogilvie, S. M.; Robinson, D. A. *J. Photochem.* **1972**, *1*, 417–422.
- (23) Hirayama, F.; Lipsky, S. *J. Chem. Phys.* **1969**, *51*, 1939–1951.
- (24) Eaton, D. F.; Pensak, D. A. *J. Am. Chem. Soc.* **1978**, *100*, 7428–7429.
- (25) Yang, N. C.; Srinivasachar, K.; Kim, B.; Libman, J. *J. Am. Chem. Soc.* **1975**, *97*, 5006–5008.
- (26) Zobel, J. P.; Nogueira, J. J.; González, L. *Chem. Sci.* **2017**, *8*, 1482.
- (27) Schapiro, I.; Sivalingam, K.; Neese, F. *J. Chem. Theory Comput.* **2013**, *9*, 3567–3580.
- (28) Sharma, S.; Chan, G. K.-L. *J. Chem. Phys.* **2012**, *136*, 124121.
- (29) Olivares-Amaya, R.; Hu, W.; Nakatani, N.; Sharma, S.; Yang, J.; Chan, G. K.-L. *J. Chem. Phys.* **2015**, *142*, 34102.

- (30) Sun, Q.; Berkelbach, T. C.; Blunt, N. S.; Booth, G. H.; Guo, S.; Li, Z.; Liu, J.; McClain, J.; Sayfutyarova, E. R.; Sharma, S.; Wouters, S.; Chan, G. K.-L. *Wiley Interdiscip. Rev. Comput. Mol. Sci.* **2017**, *8*, e1340.
- (31) Sayfutyarova, E. R.; Sun, Q.; Chan, G. K. L.; Knizia, G. *J. Chem. Theory Comput.* **2017**, *13*, 4063–4078.
- (32) Dubinets, N. O.; Safonov, A. A.; Bagaturyants, A. A. *J. Phys. Chem. A* **2016**, *120*, 2779–2782.
- (33) Casanova, D. *Int. J. Quantum Chem.* **2015**, *115*, 442–452.
- (34) Amicangelo, J. C. *J. Phys. Chem. A* **2005**, *109*, 9174–9182.
- (35) Stephens, P. J.; Devlin, F. J.; Chabalowski, C. F.; Frisch, M. J. *J. Phys. Chem.* **1994**, *98*, 11623–11627.
- (36) Grimme, S.; Ehrlich, S.; Goerigk, L. *J. Comput. Chem.* **2010**, *31*, 2967–2970.
- (37) Weigend, F.; Ahlrichs, R. *Phys. Chem. Chem. Phys.* **2005**, *7*, 3297–3305.
- (38) Neese, F. *Wiley Interdiscip. Rev. Comput. Mol. Sci.* **2012**, *2*, 73–78.
- (39) Dunning, T. H. *J. Chem. Phys.* **1989**, *90*, 1007–1023.
- (40) Kendall, R. A.; Dunning, T. H.; Harrison, R. J. *J. Chem. Phys.* **1992**, *96*, 6796.
- (41) Papajak, E.; Zheng, J.; Xu, X.; Leverentz, H. R.; Truhlar, D. G. *J. Chem. Theory Comput.* **2011**, *7*, 3027–3034.
- (42) Papajak, E.; Leverentz, H. R.; Zheng, J.; Truhlar, D. G. *J. Chem. Theory Comput.* **2009**, *5*, 3330–3330.
- (43) Andersson, K.; Malmqvist, P.-Å.; Roos, B. O. Benchmark., <https://sanshar.github.io/caspt2>.
- (44) Helgaker, T.; Klopper, W.; Koch, H.; Noga, J. *J. Chem. Phys.* **1997**, *106*, 9639–9646.
- (45) Varandas, A. J. *J. Chem. Phys.* **2000**, *113*, 8880–8887.
- (46) Valeev, E. F.; Allen, W. D.; Hernandez, R.; Sherrill, C. D.; Schaefer, H. F. *J. Chem. Phys.* **2003**, *118*, 8594–8610.
- (47) Lee, J. S.; Park, S. Y. *J. Chem. Phys.* **2000**, *112*, 10746–10753.
- (48) Varandas, A. J. *J. Chem. Phys.* **2007**, *126*, 244105.
- (49) Miliordos, E.; Aprà, E.; Xantheas, S. S. *J. Phys. Chem. A* **2014**, *118*, 7568–7578.
- (50) Podaszwa, R.; Szalewicz, K. *Phys. Chem. Chem. Phys.* **2008**, *10*, 2735–2746.
- (51) Ehrlich, S.; Moellmann, J.; Grimme, S. *Acc. Chem. Res.* **2013**, *46*, 916–926.

Chapter 3

EXCIPLEX STABILIZATION IN ASYMMETRIC ACENE DIMERS

Adapted with permission from Krueger, R. A.; Blanquart, G. J. *Phys. Chem. A* **2019**, *123*, 1796–1806. Copyright 2019 American Chemical Society.

3.1 Introduction

Predicting spectroscopic properties of the wide range of PAH complexes potentially present in flames will require a method capable of treating both excimer and exciplex interactions. To date, most *ab initio* studies have focused on the smallest acene excimers. Binding energies and singlet excitation energies for the benzene S₁ excimer have been characterized using CASPT2[1, 2], coupled cluster methods,[3] and equation-of-motion coupled cluster methods.[4] Binding energies have been evaluated at the global minimum potential energy configuration for the excimer, corresponding to an eclipsed configuration, with one monomer translated along the intermolecular coordinate with respect to the other. The results range from 33-48 kJ/mol[2, 3] when corrected for basis set superposition error (BSSE) by the counterpoise (CP) method.[5] Even the lowest binding energy obtained is more than twice as large as the CP-corrected benchmark CCSD(T) binding energies obtained for the ground state benzene dimer in a parallel-displaced configuration.[6]

Naphthalene and larger acenes are characterized by two close-together, low-lying singlet $\pi \rightarrow \pi^*$ excited states, polarized along the two axes of the molecules. The B_{2u} state, labeled L_a , is described almost completely by a HOMO→LUMO transition, while the B_{3u} L_b state is the result of a mixed HOMO-1→LUMO and HOMO→LUMO+1 transition. In the valence-bond theory framework, the L_a state is ionic and the L_b state covalent.[7]

Time-dependent density functional theory (TDDFT) calculations performed using hybrid exchange-correlation functionals tend to underestimate the energy of the L_a state, and this error increases with increasing acene size.[8, 9] Although the ionic description of the state hints at charge separation, the L_a state cannot be classified as a “true” charge transfer state,[10, 11] indicating that the error is not directly attributable to the well-known failure of hybrid TDDFT to capture charge transfer

behavior. Use of double-hybrid functionals improves L_a energies substantially.[8, 12]

The energy of the L_b state, on the other hand, tends to be overestimated by TDDFT calculations using hybrid, double-hybrid, and range-separated functionals. Errors remain roughly constant with acene size. For several hybrid functionals, the combination of errors in both state energies leads to the incorrect L_a - L_b state ordering for the naphthalene monomer.[8, 9]

For the naphthalene excimer (NN)*, the L_a and L_b -derived states cross at an intermolecular separation of 4.5 Å,[13, 14] and the L_a -derived state becomes the lowest-energy singlet excited state around the potential energy minimum at an intermolecular separation of ≈ 3.08 Å. CASPT2 calculations yielded non-CP-corrected binding energies of 128 kJ/mol and 60 kJ/mol for the L_a and L_b -derived states of the naphthalene excimer, respectively.[13]

The lowest singlet excited state of the benzene-naphthalene exciplex is derived from the L_b state of the naphthalene monomer. An approximate CP-corrected NEVPT2 complete basis set binding energy of 19.2 kJ/mol has been reported for the complex in the S_1 state,[15] indicating a much weaker interaction than the ones observed for S_1 benzene and naphthalene excimers.

The first objective of this work is to evaluate the effectiveness of TDDFT for calculating exciplex binding and excitation energies using several exchange-correlation functionals. Three representative acene exciplexes have been selected for study: the benzene-naphthalene exciplex (BN)*, the benzene-anthracene exciplex (BA)*, and the naphthalene-anthracene complex (NA)*. TDDFT binding energies are compared against CASSCF/NEVPT2 results. Binding energies have also been calculated using the second-order algebraic diagrammatic construction method, (ADC(2)), [16] a complementary single-reference approach. To the best of our knowledge, these binding energies are the first to be reported for (BA)* and (NA)*.

To rationalize trends in exciplex binding energies, the extent of the exciton delocalization and charge transfer in each complex has been quantified using the one-electron transition density matrix. Developing a predictive model for spectroscopic parameters of arbitrary aromatic exciplexes will require a larger body of data, but the benchmark results and systems characterized in this work represent a first step towards this goal.

3.2 Computational Methods

To avoid the pitfalls associated with the lowest-energy electronic states of the small acenes, multireference complete active space self-consistent field (CASSCF) calculations with a perturbative n -electron valence perturbation theory second-order (NEVPT2) correction[17] have been performed to provide a reliable point of comparison for TDDFT results. Benchmarks have shown that the NEVPT2 method yields perturbative dynamic correlation values similar to the popular CASPT2 method,[18] but the Dyll Hamiltonian used in NEVPT2 prevents intruder state mixing and eliminates the need for shift parameters.[17] Perturbatively-corrected CASSCF calculations have the capacity to capture both static and dynamic correlation, providing a balanced treatment of both the single and double excitations observed among acenes. Standard EOM-CCSD potential energy curves flip the order of the lowest-energy singlet excited states of the naphthalene excimer around the global minimum geometry, an error that CASSCF/CASPT2 calculations correct.[13] For the relative energy of the lowest-energy singlet excited state of benzene, EOM-EE-CCSD and NEVPT2 calculations vary by less than 2 kJ/mol.[4, 18] All CASSCF wave functions were further optimized in CASCI calculations to adjust orbital coefficients before NEVPT2 corrections were calculated.

The CASSCF/CASCI/NEVPT2 techniques used here have been employed in previous work,[15] and only a brief review will be provided. This multireference procedure is used here in order to calculate complete binding curves for (BN)*, (BA)*, and (NA)* using the cc-pVDZ basis set,[19] data that is reported here for the first time. The use of a relatively small basis set to describe noncovalent interactions might rightly provoke skepticism. However, it has been shown that, for aromatic exciplexes, cancellation of BSSE and basis set incompleteness error yields cc-pVDZ binding energies very close to the complete basis set limit, providing an excellent cost–accuracy trade-off.[15] Energies calculated according to this procedure will be described simply as NEVPT2 energies.

The active spaces for multireference calculations include one p orbital parallel to the intermolecular axis and one electron for each carbon atom. Smaller active spaces yield the wrong state ordering for naphthalene complexes.[13] The resulting active spaces range in size from 16 active orbitals and electrons to 24 active orbitals and electrons.

To make these large active spaces computationally tractable, the density matrix renormalization group (DMRG) approach[20–22] was used in both CASSCF and

NEVPT2 calculations. By employing an approximate wave function ansatz known as the matrix product state (MPS), the DMRG method offers a polynomial-scaling alternative to exponentially-scaling CAS methods. The accuracy of the wave function is determined by the dimension chosen for the matrices, known as the bond dimension M . For a discussion of the errors associated with the DMRG approach and the convergence of DMRG results with increasing M , the reader is referred to recent discussions of the method.[23, 24] The number of variational parameters scales as M^2 . An approximate compressed MPS perturber[23] was used in NEVPT2 calculations, which were of the strongly contracted type. DMRG calculations were performed using the PySCF framework version 1.3b[25] with an interface to the Block DMRG solver version 1.5.0.[26]

CASSCF starting orbitals were obtained from restricted Hartree Fock (RHF) calculations, and active space p orbitals were selected using the atomic valence active space (AVAS) technique.[27] The choice of starting orbital type can affect the convergence of DMRG energies with increasing M , but aromatic exciplex binding energies computed using canonical and localized starting orbitals are both generally well-converged with $M = 500$ for CASSCF calculations and $M = 1200$ for CASCI and NEVPT2 calculations.[15] For the larger (NA)* exciplex, setting $M = 1000$ for the CASSCF step was necessary to obtain a converged binding energy, and localized B3LYP starting orbitals were used because RHF orbitals generated were of poor quality. For (BA)*, the binding energy calculated using both sets of conditions differed by less than 1 kJ/mol, so the full binding curve was generated using $M = 500$ for the CASSCF step and RHF starting orbitals.

For TDDFT calculations, representative functionals from several major classes have been chosen. The B3LYP functional[28] has been chosen from the hybrid GGAs, as well as the BHandHLYP functional, which includes a larger amount of Hartree-Fock exchange than other hybrids.[29] The B2PLYP functional[30] with a double excitation correction[31] was chosen from the double hybrids. Grimme's D3 empirical dispersion correction with Becke-Johnson damping[32] was applied to the B3LYP, B2PLYP, and BHandHLYP functional results. Though developed for ground state DFT calculations, the D3 correction has also significantly improved the TDDFT description of excimers, at least for dimers in valence excited states such as the ones considered in this work. [33, 34] To accelerate double hybrid calculations, the resolution of identity (RI) approximation[35] was used in the evaluation of Coulomb integrals.

Range-separated functionals have shown particular promise for describing the electronic states of aromatic systems.[10] Among these functionals, the ω B97 functional,[36] which includes varying Hartree-Fock exchange for all long-range interactions, and the ω B97X-D3 functional,[37] which includes a region of fixed Hartree-Fock exchange, were used.

To control the transition between long-range exact exchange and short-range semilocal exchange, range separated functionals rely on the use of a range-split parameter γ . Tuning γ values for individual systems to enforce as closely as possible the DFT version of Koopmans' theorem has been shown to improve the accuracy of range-separated functionals.[10, 38]

To examine the effectiveness of this technique for exciplex binding energy calculations, the long-range corrected BLYP functional, LC-BLYP,[39] has been used, along with two variants of the LC-BLYP functional, each with γ tuned to minimize the difference between the energy of the highest-occupied molecular orbital in the ground state and the ground state ionization energy. For one of the functionals, LC-BLYP-TM, the tuning is performed only for the larger monomer in each complex. For the other, LC-BLYP-TD, tuning is performed for the complete dimer at its minimum-energy geometry. Values of γ used in each functional for each exciplex are reported in [40]. Optimal γ values do depend on the intermolecular separation of the complex, with γ for the dimer approaching γ for the larger monomer at an intermolecular separation of 10 Å. To prioritize correct treatment of the exciplexes near their energy minima, we have chosen to set γ for the LC-BLYP-TD functional to the optimal value obtained for the minimum-energy dimer configuration.

The def2-TZVP[41] basis set has been used for all TDDFT calculations, with the def2/JK auxiliary basis[42] used in RI calculations. TDDFT energies are generally less sensitive to basis set size than wave function methods. For electronic transition energies in a range of organic molecules, the def2-TZVP basis generally yields small errors with respect to the much larger aug-cc-pVTZ basis, providing excellent accuracy relative to computational cost.[43] Based on a benchmark study involving the ground state binding energies of the S66 noncovalent dimer test set, BSSE is expected to represent $\leq 12\%$ of the total binding energy.[44] The Tamm-Dancoff approximation was applied in all TDDFT calculations.

As an alternative single-reference approach, the ADC(2) method[16] was used together with the smaller cc-pVDZ basis set[19] because of the method's high memory requirements.[8, 16] ADC(2) excitation energies were added to MP2 ground

state energies, which are consistent with the ADC(2) reference state.[45]

All TDDFT and ADC(2) calculations were performed using the ORCA software package[46] version 4.0.0 with integration grid size 5. Statistical descriptors of exciton character were calculated using the TheoDORE package version 1.0.[47] Molecule graphics have been generated using VMD version 1.9.1.[48]

Previous studies of aromatic excimers have shown that an eclipsed configuration is the most favorable geometry for complexes in the lowest singlet excited state,[49–52] while parallel-displaced configurations have larger binding energies in the ground state for most acenes.[50, 53] Exciplex geometries considered in this work (Fig. 3.1) resemble the minimum-energy structures for acene excimers, although the monomer size mismatch in the exciplex structures means that the larger monomer is not perfectly eclipsed by the smaller one. For (BA)*, two eclipsed configurations are possible. The configuration with the benzene centered over the middle ring of the anthracene was chosen because its binding energy is greater than the binding energies of configurations with the benzene centered over a side ring.

Binding curves were generated by translating the monomers along the intermolecular coordinate r_z , with intramolecular coordinates frozen at their ground state values. Ground state monomer geometries were computed with DFT using the B3LYP functional and the def2-TZVP basis set. Adiabatic absorption energies, the difference between the minima of the ground and S_1 states, were computed for the naphthalene and anthracene monomers using each method for which excited-state gradients were available. Relaxation of monomer and dimer structures in the S_1 state performed using B3LYP TDDFT gradients has a minor impact on intramolecular and intermolecular C–C distances (≈ 0.02 Å), including a breaking of the six-fold symmetry of the benzene in the (BN)* complex (Tables S2-S5). Geometry changes are small enough, though, that we expect relative trends in exciplex binding energy to apply to both relaxed and unrelaxed structures.

The S_1 binding energy E_B is defined as

$$E_B = |E(r_z = r_0) - E(r_z = 10)|, \quad (3.1)$$

where r_0 is the minimum-energy intermolecular separation. It is important to note that the lowest-energy singlet excited state for the separated monomers ($r_z = 10$ Å) has the larger monomer in the first excited state (S_1) and the smaller monomer in the ground state (S_0) because the $S_0 \rightarrow S_1$ transition energy decreases with increasing acene size. This configuration serves as the reference in E_B calculations. Excimers

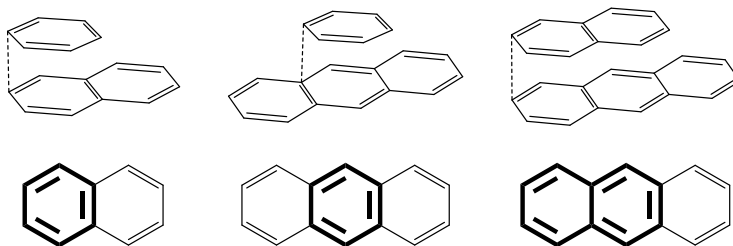


Figure 3.1: Eclipsed geometries from side and top perspectives for (BN)* (left), (BA)* (center), and (NA)* (right). The intermolecular coordinate r_z is marked with a dotted line.

have degenerate reference states. The excitation energies corresponding to vertical monomer absorption, ΔE_V , and adiabatic monomer absorption, ΔE_A , refer to the excitation energy of the larger monomer in the complex for the same reason.

3.3 Results and Discussion

Error in the TDDFT Description of Exciplex Binding

For (BN)*, the potential energies computed for varying r_z (Fig. 3.3) at the NEVPT2/cc-pVDZ level yield an E_B value of 18.16 kJ/mol (Table 3.1). The complex has an approximate complete basis set limit binding energy of 19.2 kJ/mol,[15] more than 30% higher than the CCSD(T)-corrected DFT binding energy for the ground state complex in an eclipsed configuration (≈ 14.5 kJ/mol).[54] This difference suggests that exciplex stabilization is an important contributor to the complex's S_1 binding energy. Error due to the use of the DMRG approach is estimated at ≈ 1 kJ/mol based on E_B convergence with M for this complex.[15]

The shape and well depth of the intermolecular exciplex potential energy surface varies significantly between the TDDFT calculations performed using different exchange-correlation functionals. The LC-BLYP functional has a binding energy 54% lower than the NEVPT2/cc-pVDZ result. The tuned LC-BLYP functionals perform better—the LC-BLYP-TM functional yields a binding energy 28% too low, while the LC-BLYP-TD functional comes within 7% of the correct result. For $r_z \geq 4.5$ Å, all of the LC-BLYP functionals are in excellent agreement, suggesting that relative energy is insensitive to γ outside the region of the global minimum, and the choice to tune γ based on the global minimum geometry is justified.

While another range-separated functional, ω B97, matches the NEVPT2 potential energy surface extremely well around the minimum, it underbinds the complex in

the 4-6 Å region, even slightly overshooting the $r_z = 10$ Å value around 5 Å. The ω B97X-D3 functional corrects this error, but shows an extremely shifted minimum. The r_0 of 3.69 Å would be more characteristic of a ground-state aromatic complex. The hybrid functionals both overbind the complex, but the BHandHLYP functional, with a significantly larger proportion of exact exchange, performs much better. The B3LYP functional E_B value is more than double the NEVPT2 one, while the B2PLYP functional overbinds the complex by 80%. The dispersion contribution to E_B provided by the D3 correction is significant. Without this correction, the B3LYP and BHandHLYP functionals do not show an attractive exciplex interaction (Fig. 3.2). The uncorrected B2PLYP functional still shows a stabilizing interaction, with the MP2 component of the double-hybrid functional likely capturing a portion of the dispersion energy. The ADC(2) method is significantly overbinding, yielding an E_B more than twice as high as the NEVPT2 result. The r_0 obtained is also more than 0.1 Å smaller than the next-smallest r_0 .

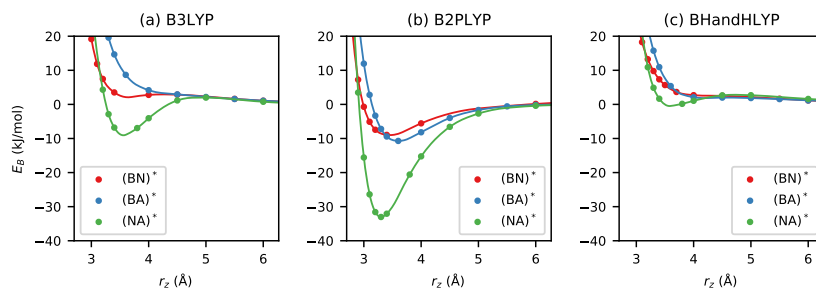


Figure 3.2: S_1 exciplex binding curves obtained using the B3LYP, B2PLYP, and BHandHLYP functionals with no empirical dispersion correction applied. Lines have been added to guide the eye.

The $(BA)^*$ exciplex, not surprisingly, is bound more strongly than $(BN)^*$, with an NEVPT2 binding energy of 27.69 kJ/mol. Similar E_B trends are observed in results from the LC-BLYP and LC-BLYP-TM functionals (Fig. 3.4). For this complex, the LC-BLYP-TD improves on the LC-BLYP-TM result by only ≈ 1.5 kJ/mol.

E_B values for the ω B97X-D3 functional are now too high, and both the ω B97 and ω B97X-D3 functionals display an apparent instability in the 3.1-3.2 Å region, resulting in linear regions in the potential energy curves to the left of r_0 . Hybrid and double hybrid results match the NEVPT2 curve closely, with B2PLYP and B3LYP results almost identical and slightly overbinding.

Similar behavior is observed for the hybrids and double hybrid in the $(NA)^*$ system

(Fig. 3.5), although a few differences from the other exciplexes are noticeable. In the absence of the D3 correction, the three hybrid and double hybrid functionals still show a stabilizing exciplex interaction (Fig. 3.2). Among the range-separated functionals, the LC-BLYP-TM and LC-BLYP-TD binding energies are larger than the ω B97 and ω B97X-D3 ones. The ω B97 functional shows unusual behavior around r_0 , while the ω B97X-D3 functional r_0 is again dramatically shifted toward high r_z values, a geometry error accompanied by a binding energy more than 50% too low. As in the case of (BN)*, tuning the LC-BLYP functional for the complex rather than the larger monomer alone improves the binding energy—by approximately 10 kJ/mol for this complex. This LC-BLYP-TD E_B value falls within 1 kJ/mol of the NEVPT2 reference, though the r_0 obtained is more than 0.15 Å too low, consistent with most of the other functionals.

Table 3.1: Binding Energies E_B and Optimal S₁ Intermolecular Separations r_0 for (BN)*, (BA)*, and (NA)*

Excitation Type	(BN)*		(BA)*		(NA)*	
	L_b		L_a		L_a	
Method	E_B (kJ/mol)	r_0 (Å)	E_B (kJ/mol)	r_0 (Å)	E_B (kJ/mol)	r_0 (Å)
NEVPT2	18.16	3.34	27.69	3.28	49.30	3.34
ADC(2)	38.60	3.00	46.58	3.16	92.10	3.05
LC-BLYP	8.37	3.41	10.78	3.49	25.04	3.25
LC-BLYP-TM	13.06	3.25	15.93	3.40	40.26	3.21
LC-BLYP-TD	16.97	3.17	17.47	3.35	48.90	3.19
ω B97	17.13	3.48	21.39	3.44	37.28	3.40
ω B97X-D3	15.46	3.69	29.34	3.47	27.04	3.71
BHandHLYP	24.79	3.25	25.94	3.42	53.63	3.25
B2PLYP	32.67	3.15	34.40	3.33	73.97	3.19
B3LYP	42.08	3.13	32.69	3.33	76.90	3.23

Separating the exciplexes into those derived from L_a states of the larger monomer and those derived from L_b states (Fig. 3.6) is a useful first step in analyzing trends in TDDFT error. ΔE_V and ΔE_A values suggest that, between the anthracene and naphthalene parent monomers, the L_b naphthalene excitation represents a greater challenge than the L_a anthracene excitation. Every ΔE_V value computed for naphthalene (Table 3.2) overshoots the estimated experimental value by at least 30 kJ/mol. The trend among ΔE_A values is similar. The difference between ΔE_V and ΔE_A results is related to the quality of the excited-state potential energy surface, and the differences

Table 3.2: Monomer S_1 Absorption Energies ΔE_V and ΔE_A .

Method	Naphthalene (L_b)			Anthracene (L_a)		
	E_V (kJ/mol)	E_A (kJ/mol)	E_V-E_A (kJ/mol)	E_V (kJ/mol)	E_A (kJ/mol)	E_V-E_A (kJ/mol)
LC-BLYP	453.8	448.3	5.5	383.0	366.4	16.6
LC-BLYP-TM	444.6	437.2	7.4	365.0	347.6	17.4
ω B97	466.6	456.2	10.4	391.8	373.3	18.5
ω B97X-D3	457.1	448.9	8.2	378.1	360.6	17.5
BHandHLYP	463.2	458.7	4.5	363.2	347.2	16.0
B3LYP	433.3	422.8	10.5	330.6	313.5	17.1
NEVPT2	436.4	—	—	366.3	—	—
ADC(2)	440.9	—	—	368.5	—	—
B2PLYP	431.0	—	—	346.7	—	—
Exptl.	398.8 ^a	383.1 ^b	15.7	347.7 ^a	331.0 ^c	16.7

^aEstimated vertical excitation energies with solvent correction[9] derived from experimental 0–0 excitation energies.[55] ^bRef. [56]. ^cRef [57].

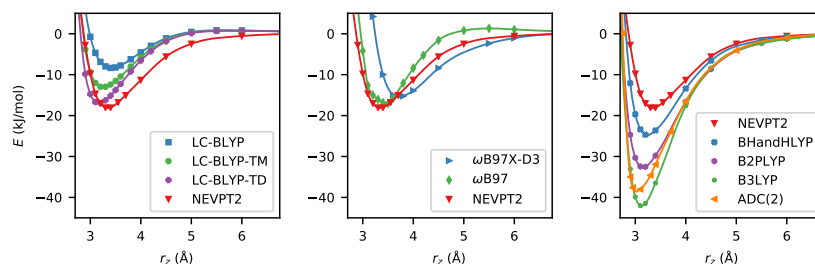


Figure 3.3: S_1 potential energies for (BN)* relative to $r_z = 10$ Å. Lines have been added to guide the eye.

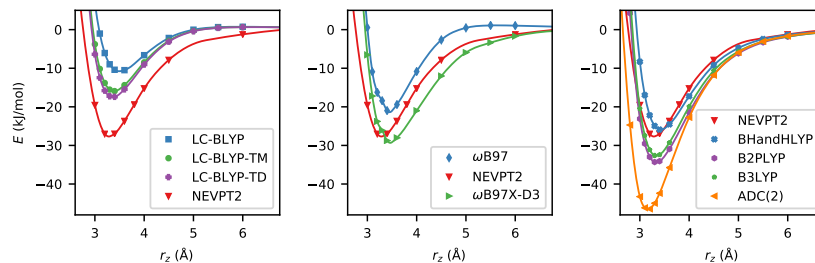


Figure 3.4: S_1 potential energies for (BA)* relative to $r_z = 10$ Å.

obtained for naphthalene are noticeably smaller than the estimated experimental difference. The NEVPT2 ΔE_V reported here is approximately 27 kJ/mol higher than the ΔE_V value reported for a similar CASPT2 calculation.[58] Based on additional

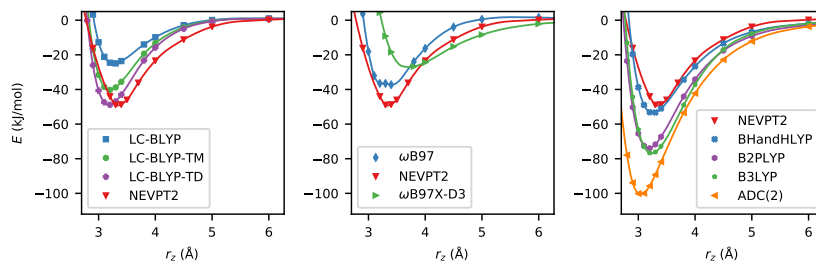


Figure 3.5: S_1 potential energies for $(NA)^*$ relative to $r_z = 10 \text{ \AA}$.

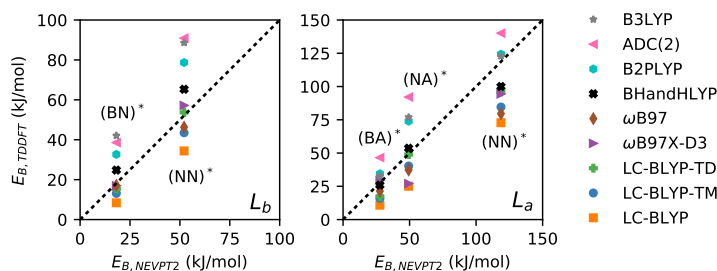


Figure 3.6: TDDFT binding energies E_B as a function of NEVPT2 binding energies for exciplexes in the L_b state (left) and the L_a state (right). For the naphthalene excimers, CASPT2/cc-pVDZ binding energies[13] are substituted for NEVPT2 values.

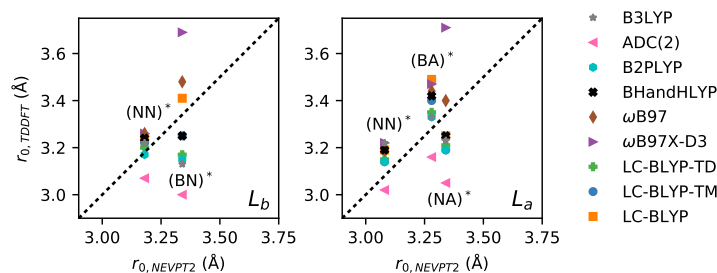


Figure 3.7: TDDFT optimal intermolecular separations r_0 as a function of NEVPT2 r_0 values for exciplexes in the L_b state (left) and the L_a state (right). For the naphthalene excimers, CASPT2/cc-pVDZ r_0 values[13] are substituted for NEVPT2 results.

NEVPT2 calculations, we attribute $\approx 6 \text{ kJ/mol}$ of this difference to the difference in monomer geometries used (B3LYP/def2-TZVP in this work vs. MP2/6-31G*), and a further $\approx 6 \text{ kJ/mol}$ to the different NEVPT2 basis sets (cc-pVDZ in this work vs. TZVP). The additional 15 kJ/mol difference may be attributed to the different perturbative correction approach (NEVPT2 vs CASPT2). For anthracene, though,

values of ΔE_A and ΔE_V are generally in better agreement with experiment, and the agreement between computed and experimental $\Delta E_V - \Delta E_A$ values is excellent.

When E_B values for the exciplexes are considered, though, the pattern becomes more complex. To provide more examples of each type, the L_a - and L_b -derived states of (NN)* in the eclipsed configuration are also considered. It is immediately apparent that the B2PLYP and B3LYP functionals perform much better for L_a -derived states than for L_b -derived states, with no meaningful difference between the two functionals for L_a -derived states. Both functionals predict L_b vertical excitation energies for the naphthalene monomer that are in excellent agreement with the NEVPT2 excitation energy (Table 3.2), so the error stems from problems with the description of the exciplex in its minimum-energy conformation.

The ω B97 and ω B97X-D3 functionals perform well for L_b -derived states, despite the fact that their ΔE_V values are 20-30 kJ/mol higher than the NEVPT2 ones. The fact that this destabilization of the excited monomer does not lead to overbinding indicates that the exciplex with $r_z = r_0$ is destabilized to a similar degree. For L_a -derived states more strongly bound than (BA)*, both functionals are underbinding, although the ordering of the two E_B values varies between complexes.

A difference between E_B results for L_a - and L_b -derived states is also apparent for the BHandHLYP functional. For L_b -derived states, the functional is uniformly overbinding, a result consistent with a good description of the exciplex but a high L_b excitation energy for the naphthalene monomer. The L_a excitation energy for naphthalene is not correspondingly high, resulting in an L_b-L_a gap of only 8 kJ/mol, when experimental reports range from 45-70 kJ/mol.[13] This depressed L_a energy likely contributes to the most notable BHandHLYP E_B error, observed for the L_a -derived naphthalene excimer.

Perhaps the most consistent TDDFT errors are observed from the LC-BLYP and tuned LC-BLYP functionals. The tuned functionals in particular yield reasonable ΔE_V values, although absolute error does increase with increasing interaction strength. A similar L_a-L_b energy difference for the naphthalene monomer of approximately 30 kJ/mol is obtained from all three LC-BLYP functionals. Although smaller than the reported NEVPT2 energy difference, this result is at least on the same order of magnitude. E_B errors of 20-40% are observed for all exciplexes, suggesting that the under-stabilization of minimum-energy exciplexes might have a uniform cause for both L_a - and L_b -derived states.

Errors in r_0 , illustrated in Fig. 3.7, do not show a uniform dependence on the exciplex state. For the more tightly-bound exciplexes (NEVPT2 $r_0 < 3.25$ Å), all results agree within ≈ 0.1 Å. Error increases significantly for the more loosely-bound complexes. The B2PLYP and B3LYP functionals give r_0 values approximately 0.2 Å too small for the L_b -derived (BN)*, but perform very well for the L_a -derived (BA)*. The r_0 values obtained from the ω B97X-D3 functional vary unpredictably—for (NA)*, the r_0 obtained is 0.37 Å too high.

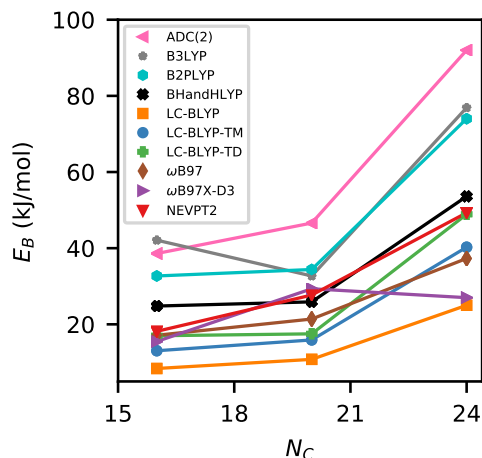


Figure 3.8: Binding energy E_B as a function of the number of carbons N_C in each exciplex.

The most consistent errors overall in both E_B and r_0 values are observed for the ADC(2) method. ADC(2) ΔE_V results for both naphthalene and anthracene monomers are in excellent agreement with the NEVPT2 values. However, the complexes are uniformly overbound, with absolute E_B errors in the 20-40 kJ/mol range, and the r_0 values obtained are all 0.05-0.1 Å too low. This overbinding may be due in part to the commonly-observed tendency of the MP2 method—which supplies the ground state energy in ADC(2) calculations—to overbind van der Waals complexes. Using a larger basis set seems unlikely to alleviate the issue, as recalculation of the binding energy of (BN)* using the cc-pVTZ basis at the cc-pVDZ minimum geometry and reference configuration yields an even higher binding energy of 45.5 kJ/mol, and repeating the procedure for (BA)* results in $E_B = 46.89$, a value virtually identical to the cc-pVDZ result.

Beyond reproducing individual binding energies, it is desirable for functionals to capture the relationships between the E_B values obtained for each complex. The

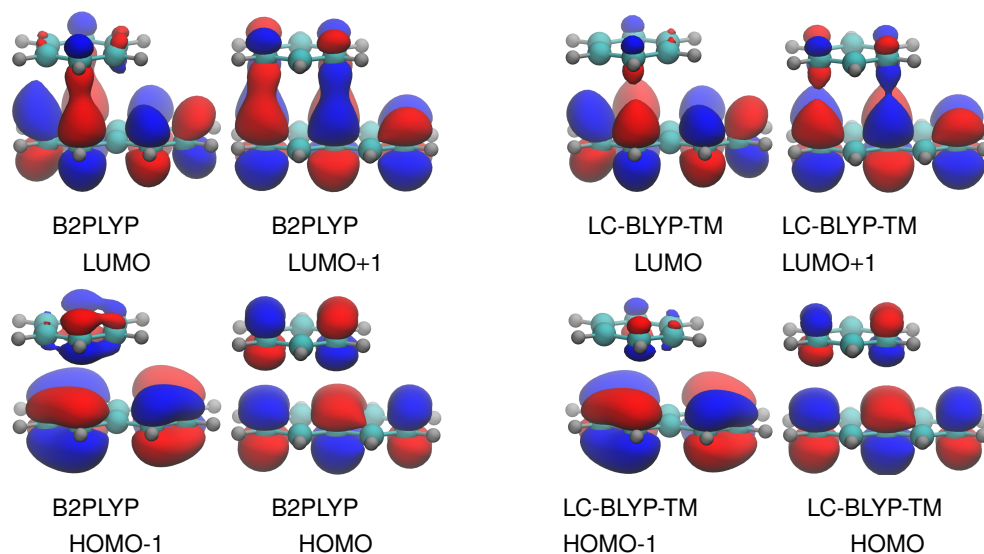


Figure 3.9: Frontier natural transition orbital isosurfaces for $(\text{BN})^*$.

$\omega\text{B97X-D3}$ and B3LYP functionals fail to capture the monotonic increase in E_B values with respect to complex mass (Fig. 3.8). The remaining functionals severely underestimate difference in E_B values for $(\text{BN})^*$ and $(\text{BA})^*$. The NEVPT2 E_B results for the two differ by more than 50% (9.5 kJ/mol), while the maximum obtained is 29% (2.4 kJ/mol) from the LC-BLYP functional.

Physical Origins of Exciplex Stabilization

It remains, then, to rationalize both TDDFT errors and the observed NEVPT2 trends in exciplex binding energy. The binding energies of ground-state noncovalent aromatic complexes scale approximately linearly with the number of carbon atoms in the complex N_C .^[53, 59–62] This is not the case for the exciplexes considered here (Fig. 3.8). For $(\text{BN})^*$ and $(\text{BA})^*$, the ratios of $E_{B,NEVPT2}$ to N_C are 1.16 kJ/mol and 1.15 kJ/mol, respectively. For $(\text{NA})^*$, the ratio is 2.05 kJ/mol.

Considering the form of the natural orbitals involved in the electronic transitions can help shed light on their varying character. Natural transition orbitals (NTOs) have been calculated for each exciplex using one generally overbinding functional, B2PLYP, and one underbinding functional, LC-BLYP-TM. For $(\text{BN})^*$, the difference between the E_B values obtained from each is high—the B2PLYP E_B is 80% too high, and the LC-BLYP-TM E_B is 28% too low. In both sets of NTOs (Fig. 3.9), the electron density is shifted toward the naphthalene monomer, suggesting that the exciplex excitation is principally a naphthalene excitation. However, this shift is more dramatic for the LC-BLYP-TM NTOs. The LC-BLYP-TM bonding orbitals

show significantly less electron density in the intermolecular region.

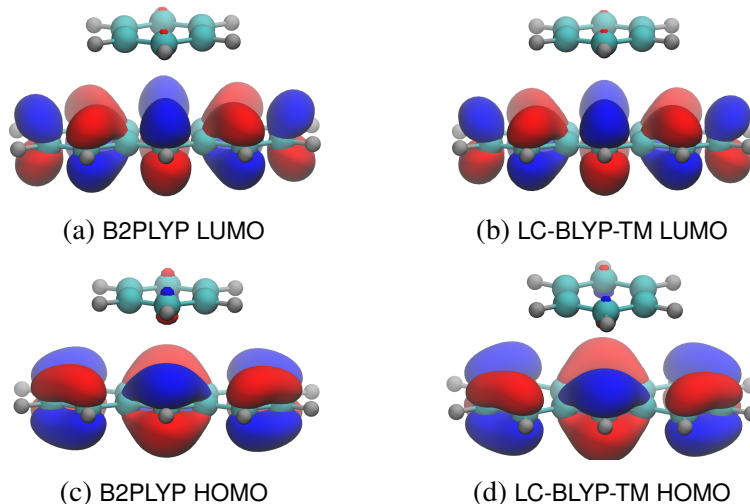


Figure 3.10: Frontier natural transition orbital isosurfaces for (BA)*.

To quantify the degree of exciton delocalization and the charge transfer contribution, statistical descriptors based on the one-electron transition density matrix formulated by Plasser and coworkers.[14, 63] These descriptors have been calculated for the B2PLYP functional and the LC-BLYP-TM functional (Table 3.3). Charge transfer number CT ranges from zero for a completely localized Frenkel excitation to unity for complete charge transfer. For the L_a -derived state of the naphthalene excimer, $CT = 0.5$, indicating equal charge transfer and localized excitation character.[14]

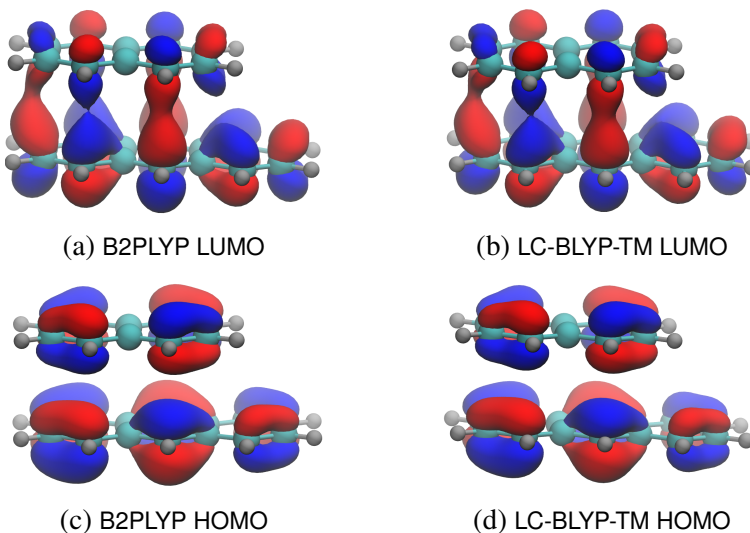


Figure 3.11: Frontier natural transition orbital isosurfaces for (NA)*.

The participation ratio PR of each monomer in the excitation represents a second

measure of excitation delocalization, with $PR = 2$ in the case of a symmetric excimer like $(NN)^*$, where the two indistinguishable monomers participate equally. The average exciton position, POS, ranges from 1-2, POS = 1,2 corresponds to exciton localization on a single monomer, and maximally delocalized excited states have POS = 1.5. For the mixed exciplexes, POS = 1 indicates exciton localization on the smaller monomer and POS = 2 indicates localization on the larger monomer. Population analysis for the electron and hole created by the excitation has also been performed to locate the charge carriers on specific monomers.

For $(BN)^*$, the picture that emerges from both functionals is one in which the excitation is primarily localized on the naphthalene monomer, but not exclusively—it is spatially shifted in the direction of the benzene monomer, which has nonzero electron and hole populations. However, the degree of delocalization varies noticeably between the two functionals, with the overbinding B2PLYP functional producing additional exciton delocalization. The difference in CT values is particularly apparent, with the B2PLYP CT almost 80% higher than the LC-BLYP-TM CT.

In the case of $(BA)^*$, the exciton descriptors obtained using each functional are much more similar, and considering the NTOs for the exciplex (Fig. 3.10) suggests why this might be the case—the electron density is located almost entirely on the anthracene monomer, particularly for the bonding LUMO orbitals. With $CT < 0.1$ and $PR < 1.1$, it is clear that $(BA)^*$ would be better described as BA^* .

If so, why is the per-carbon binding energy so similar to the one obtained for $(BN)^*$, where moderate exciplex stabilization is present? The larger size of the BA compared to BN suggests enhanced noncovalent interactions regardless of electronic state, and electronic excitation can increase the polarizability of aromatics.[64] Thus, the excitation of the anthracene monomer may increase the interaction strength even without notable exciton delocalization. The fact that the excitation is largely localized on the anthracene monomer likely also explains why the performance of the LC-BLYP-TM and LC-BLYP-TD functionals was so similar for $(BA)^*$; the electronic state of the benzene molecule remains nearly unchanged, so including it in the structure used for tuning does not significantly improve the description of the excited complex.

Although the NEVPT2 binding energy for $(BA)^*$ falls between the LC-BLYP-TM and B2PLYP ones, it is significantly larger than the calculated $(BN)^*$ NEVPT2 binding energy. Examination of the canonical HOMO orbitals obtained in the NEVPT2 calculation reveals a small amount of electron density on the benzene

monomer. Orbitals plotted with the same isovalue obtained from the LC-BLYP-TM and B2PLYP calculations do not show this density, suggesting that both functionals may underestimate the (BA)* PR value—an error that would not be uncovered by considering each binding energy in isolation. Shorter intermolecular distances are generally associated with increased orbital overlap and thus increased possibility for exciton delocalization. Differences in the observed levels of exciton delocalization, then, are consistent with differences in r_0 , which is overestimated by every DFT functional relative to the NEVPT2 result, regardless of the absolute binding energies obtained.

Finally, the binding energies obtained from the two functionals for (NA)* are in better agreement, each falling within 30% of the NEVPT2 result. The geometric agreement is striking; r_0 values differ by less than 0.02 Å, and the NTOs are virtually identical (Fig. 3.11). With CT \approx 0.35 and PR > 1.5, the charge transfer and exciton delocalization contributions to stabilization of (NA)* are the largest obtained for any of the exciplexes. The similarity of the exciton delocalization descriptors obtained using both functionals reflects the smaller relative error of each as well as the geometric similarity.

Table 3.3: Statistical descriptors for (BN)*, (BA)*, and (NA)* computed using the S_1 TDDFT one-electron transition density matrices at r_0 .

Complex	Functional	CT	PR	POS	Large Monomer		Small Monomer	
					h+ pop.	e- pop.	h+ pop.	e- pop.
(BN)*	B2PLYP	0.254	1.415	1.821	0.778	0.824	0.197	0.151
	LC-BLYP-TM	0.142	1.272	1.879	0.846	0.874	0.133	0.105
(BA)*	B2PLYP	0.060	1.063	1.969	0.945	0.936	0.025	0.034
	LC-BLYP-TM	0.053	1.058	1.972	0.926	0.928	0.027	0.026
(NA)*	B2PLYP	0.354	1.560	1.765	0.712	0.768	0.255	0.199
	LC-BLYP-TM	0.349	1.546	1.771	0.713	0.766	0.246	0.193

References

- (1) Jara-Cortés, J.; Rocha-Rinza, T.; Hernández-Trujillo, J. *Comput. Theor. Chem.* **2015**, *1053*, 220–228.
- (2) Rocha-Rinza, T.; Vico, L. D.; Veryazov, V.; Roos, O. *Chem. Phys. Lett.* **2006**, *426*, 268–272.
- (3) Rocha-Rinza, T.; Christiansen, O. *Chem. Phys. Lett.* **2009**, *482*, 44–49.
- (4) Diri, K.; Krylov, A. I. *J. Phys. Chem. A* **2012**, *116*, 653–662.

- (5) Van Duijneveldt, F. B.; van Duijneveldt-van de Rijdt, J. G. C. M.; van Lenthe, J. H. *Chem. Rev.* **1994**, *94*, 1873–1885.
- (6) Miliordos, E.; Aprà, E.; Xantheas, S. S. *J. Phys. Chem. A* **2014**, *118*, 7568–7578.
- (7) Orchin, M.; Jaffè, H. H., *Symmetry, Orbitals, and Spectra*; Wiley: New York, 1971.
- (8) Prlj, A.; Sandoval-Salinas, M. E.; Casanova, D.; Jacquemin, D.; Corminboeuf, C. *J. Chem. Theory Comput.* **2016**, *12*, 2652–2660.
- (9) Grimme, S.; Parac, M. *Chemphyschem* **2003**, *4*, 292–295.
- (10) Kuritz, N.; Stein, T.; Baer, R.; Kronik, L. *J. Chem. Theory Comput.* **2011**, *7*, 2408–2415.
- (11) Richard, R. M.; Herbert, J. M. *J. Chem. Theory Comput.* **2011**, *7*, 1296–1306.
- (12) Goerigk, L.; Grimme, S. *J. Chem. Theory Comput.* **2011**, *7*, 3272–3277.
- (13) Shirai, S.; Kurashige, Y.; Yanai, T. *J. Chem. Theory Comput.* **2016**, *12*, 2366–2372.
- (14) Plasser, F.; Lischka, H. *J. Chem. Theory Comput.* **2012**, *8*, 2777–2789.
- (15) Krueger, R. A.; Blanquart, G. *Int. J. Quantum Chem.* **2019**, *119*, e25819.
- (16) Trofimov, A. B.; Schirmer, J. *J. Phys. B: At. Mol. Opt. Phys.* **1995**, *28*, 2299–2324.
- (17) Angeli, C.; Cimiraglia, R.; Evangelisti, S.; Leininger, T.; Malrieu, J. P. *J. Chem. Phys.* **2001**, *114*, 10252.
- (18) Schapiro, I.; Sivalingam, K.; Neese, F. *J. Chem. Theory Comput.* **2013**, *9*, 3567–3580.
- (19) Dunning, T. H. *J. Chem. Phys.* **1989**, *90*, 1007–1023.
- (20) Chan, G. K.-L.; Keselman, A.; Nakatani, N.; Li, Z.; White, S. R. *J. Chem. Phys.* **2016**, *014102*, 014102.
- (21) Chan, G. K.-L.; Dorando, J. J.; Ghosh, D.; Hachmann, J.; Neuscamman, E.; Wang, H.; Yanai, T. In *Frontiers in Quantum Systems in Chemistry and Physics*, Wilson, S., Grout, P. J., Maruani, J., Delgado-Barrío, G., Piecuch, P., Eds.; Springer Netherlands: Dordrecht, 2008, pp 49–65.
- (22) Chan, G. K. L.; Head-Gordon, M. *J. Chem. Phys.* **2002**, *116*, 4462–4476.
- (23) Guo, S.; Watson, M. A.; Hu, W.; Sun, Q.; Chan, G. K. L. *J. Chem. Theory Comput.* **2016**, *12*, 1583–1591.
- (24) Olivares-Amaya, R.; Hu, W.; Nakatani, N.; Sharma, S.; Yang, J.; Chan, G. K.-L. *J. Chem. Phys.* **2015**, *142*, 34102.

- (25) Sun, Q.; Berkelbach, T. C.; Blunt, N. S.; Booth, G. H.; Guo, S.; Li, Z.; Liu, J.; McClain, J.; Sayfutyarova, E. R.; Sharma, S.; Wouters, S.; Chan, G. K.-L. *Wiley Interdiscip. Rev. Comput. Mol. Sci.* **2017**, *8*, e1340.
- (26) Sharma, S.; Chan, G. K.-L. *J. Chem. Phys.* **2012**, *136*, 124121.
- (27) Sayfutyarova, E. R.; Sun, Q.; Chan, G. K. L.; Knizia, G. *J. Chem. Theory Comput.* **2017**, *13*, 4063–4078.
- (28) Stephens, P. J.; Devlin, F. J.; Chabalowski, C. F.; Frisch, M. J. *J. Phys. Chem.* **1994**, *98*, 11623–11627.
- (29) Becke, A. D. *J. Chem. Phys.* **1993**, *98*, 1372–1377.
- (30) Grimme, S. *J. Chem. Phys.* **2006**, *124*, 034108.
- (31) Head-Gordon, M.; Rico, R. J.; Oumi, M.; Lee, T. J. *Chem. Phys. Lett.* **1994**, *219*, 21–29.
- (32) Grimme, S.; Ehrlich, S.; Goerigk, L. *J. Comput. Chem.* **2010**, *31*, 2967–2970.
- (33) Huenerbein, R.; Grimme, S. *Chem. Phys.* **2008**, *343*, 362–371.
- (34) Briggs, E. A.; Besley, N. A. *Phys. Chem. Chem. Phys.* **2014**, *16*, 14455–14462.
- (35) Weigend, F.; Häser, M.; Patzelt, H.; Ahlrichs, R. *Chem. Phys. Lett.* **1998**, *294*, 143–152.
- (36) Chai, J. D.; Head-Gordon, M. *J. Chem. Phys.* **2008**, *128*, 084106.
- (37) Lin, Y.-S.; Li, G.-D.; Mao, S.-P.; Chai, J.-D. *J. Chem. Theory Comput.* **2013**, *9*, 263–272.
- (38) Stein, T.; Kronik, L.; Baer, R. *J. Am. Chem. Soc.* **2009**, *131*, 2818–2820.
- (39) Leininger, T.; Stoll, H.; Werner, H.-J.; Savin, A. *Chem. Phys. Lett.* **1997**, *275*, 151–160.
- (40) Krueger, R. A.; Blanquart, G. *J. Phys. Chem. A* **2019**, *123*, 1796–1806.
- (41) Weigend, F.; Ahlrichs, R. *Phys. Chem. Chem. Phys.* **2005**, *7*, 3297–3305.
- (42) Weigend, F. *J. Comput. Chem.* **2008**, *29*, 167–175.
- (43) Laurent, A. D.; Blondel, A.; Jacquemin, D. *Theor. Chem. Acc.* **2015**, *134*, 1–11.
- (44) Sure, R.; Brandenburg, J. G.; Grimme, S. *ChemistryOpen* **2016**, *5*, 94–109.
- (45) Dreuw, A.; Wormit, M. *Wiley Interdiscip. Rev. Comput. Mol. Sci.* **2015**, *5*, 82–95.
- (46) Neese, F. *Wiley Interdiscip. Rev. Comput. Mol. Sci.* **2012**, *2*, 73–78.
- (47) Plasser, F. TheoDORE 1.0: A Package for Theoretical Density, Orbital Relaxation, and Exciton Analysis., <http://theodore-qc.sourceforge.net>.

- (48) Humphrey, W.; Dalke, A.; Schulten, K. *J. Molec. Graphics* **1996**, *14*, 33–38.
- (49) Iyer, E. S. S.; Sadybekov, A.; Lioubashevski, O.; Krylov, A. I.; Ruhman, S. *J. Phys. Chem. A* **2017**, *121*, 1962–1975.
- (50) Dubinets, N. O.; Safonov, A. A.; Bagaturyants, A. A. *J. Phys. Chem. A* **2016**, *120*, 2779–2782.
- (51) Casanova, D. *Int. J. Quantum Chem.* **2015**, *115*, 442–452.
- (52) Amicangelo, J. C. *J. Phys. Chem. A* **2005**, *109*, 9174–9182.
- (53) Podeszwa, R.; Szalewicz, K. *Phys. Chem. Chem. Phys.* **2008**, *10*, 2735–2746.
- (54) Bludský, O.; Rubeš, M.; Soldán, P.; Nachtigall, P. *J. Chem. Phys.* **2008**, *128*, 114102.
- (55) Biermann, D.; Schmidt, W. *J. Am. Chem. Soc.* **1980**, *102*, 3163–3173.
- (56) Reylè, C.; Brèchignac, P. *Eur. Phys. J. D* **2000**, *8*, 205–210.
- (57) Staicu, A.; Rouillè, G.; Sukhorukov, O.; Henning, T.; Huisken, F. *Mol. Phys.* **2004**, *102*, 1777–1783.
- (58) Schreiber, M.; Silva-Junior, M. R.; Sauer, S. P.; Thiel, W. *J. Chem. Phys.* **2008**, *128*, 134110.
- (59) Wang, W.; Sun, T.; Zhang, Y.; Wang, Y. B. *J. Chem. Phys.* **2015**, *143*, 114312.
- (60) Fedorov, I. A.; Zhuravlev, Y. N.; Berveno, V. P. *J. Chem. Phys.* **2013**, *138*, 1–6.
- (61) Ehrlich, S.; Moellmann, J.; Grimme, S. *Acc. Chem. Res.* **2013**, *46*, 916–926.
- (62) Lee, N. K.; Park, S.; Kim, S. K. *J. Chem. Phys.* **2002**, *116*, 7910–7917.
- (63) Plasser, F.; Bäppler, S. A.; Wormit, M.; Dreuw, A. *J. Chem. Phys.* **2014**, *141*, 024107.
- (64) Benchea, A. C.; Babusca, D.; Morosanu, A. C.; Dimitriu, D. G.; Dorohoi, D. O. *AIP Conf. Proc.* **2017**, *1796*, 030013.

*Chapter 4***PREDICTING AROMATIC EXCIPLEX FLUORESCENCE
EMISSION ENERGIES**

Adapted from Ref. [1] with permission from the PCCP Owner Societies.

4.1 Introduction

With a complete understanding of the error associated with TDDFT descriptions of exciplex interactions, we are ready to undertake a larger-scale exploration of the photoresponse of flame-relevant PAH complexes. Our first objective for this work is to provide a database of high-quality TDDFT fluorescence emission energies for noncovalent PAH homo- and heterodimers, focusing on complexes containing the small- and medium-sized PAHs likely to be present in the largest quantities in flames. These PAHs have recently been identified as the most probable soot-nucleating species.[2] Ultimately, calculating fluorescence emission energies for every possible heterodimer is not a computationally tractable approach, so we will attempt to link calculated exciplex fluorescence for the heterodimers with the electronic and geometric properties of the constituent monomers. If such relationships exist, they will allow spectroscopists to make use of the large databases of calculated PAH monomer properties already available.[3, 4]

4.2 Methods

Describing the lowest-energy singlet valence excited states of PAHs represents a well-known challenge for TDDFT. The electronic structure of acene monomers is marked by two low-lying singlet excited states. The L_a state consists almost entirely of a HOMO→LUMO transition, while the L_b state represents a mix of HOMO-1→LUMO and HOMO→LUMO+1 transitions. Noncovalent dimer formation can change the energy ordering of the transitions; e.g., the L_b state is lower in energy than the L_a state for the naphthalene monomer, but the order is reversed for the dimer, with the state energies crossing around an intermolecular distance of 3.5 Å.[5, 6] Several hybrid functionals, including the popular B3LYP functional, reverse the order of these states for the naphthalene monomer.[7, 8] The LC-BLYP functional[9] provides a reasonably well-balanced treatment of the L_a and L_b excitations in acenes. This range-separated functional also reproduces the short-range attractive portion

of the acene exciplex potential energy surfaces (around 3 Å) without an additional dispersion correction.[10]

Performance of the LC-BLYP functional may be further optimized by tuning the range-split parameter γ , which controls the switching between DFT exchange at short interaction distances and Hartree-Fock exchange at long interaction distances.[11, 12] For each starting structure, γ is chosen to minimize the disagreement between calculated orbital energies for the neutral and ionized structures and the predictions made using the DFT version of Koopman's theorem. The tuning procedure improves the description of the exciplex interaction around the minimum-energy geometry without significantly changing monomer excitation energies, leading to better agreement between DFT and multireference exciplex binding energies.[10] Values of γ used for each complex and monomer are reported in [1]. As a check, fluorescence energies have been recalculated for a subset of complexes using the B2PLYP functional[13] with doubles correction,[14] which has also been shown to describe exciplex interactions well.[10] The two functionals are in good agreement, with the B2PLYP functional predicting emission energies slightly lower than the tuned LC-BLYP functional for most complexes (Fig. 4.1).

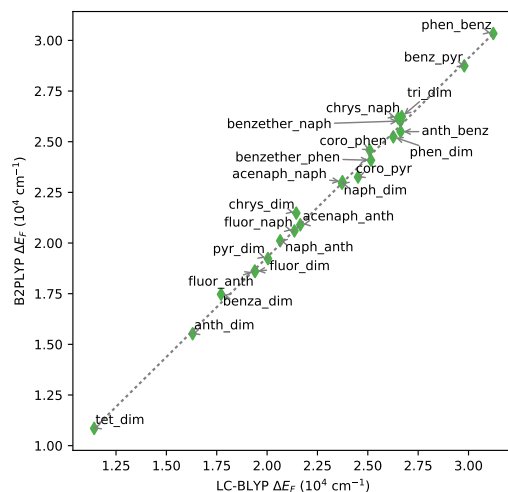


Figure 4.1: A comparison of ΔE_F values computed using the LC-BLYP-T functional with ΔE_F values computed using the B2PLYP-D3 functional.

Calculating oscillator strengths for electronic transitions is an important second step in estimating their contributions to experimental spectra and predicting relative fluorescence band intensity. Range-separated functionals in general reproduce EOM-CCSD oscillator better than either GGA or hybrid GGA functionals, with

the LC-BLYP functional among the top three performers.[15] The tuned LC-BLYP functional has also shown top performance for calculated fluorescence lifetimes.[16] Tuned versions of the LC-BLYP functional (LC-BLYP-T) have been used in all electronic transition energies and oscillator strengths reported, and LC-BLYP-T analytical gradients were used in the S_1 potential energy surface geometry optimization. The def2-TZVP basis set[17] was chosen because it yields electronic transition energies that agree well with the ones calculated using the much larger aug-cc-pVTZ basis set,[18] and def2-TZVP binding energies for small exciplexes are in good agreement with multireference results.[10] Basis set error in multireference calculations of exciplex binding energies has been discussed extensively in a recent work.[19] The Tamm-Dancoff approximation was applied. Calculations were carried out using the ORCA electronic structure package[20] version 4.0.0. Integration grid size 5 was used, with tight SCF convergence.

Eclipsed configurations typically represent the lowest-energy geometry for aromatic excimers,[21–23] so starting structures for the exciplexes were chosen to maximize the number of overlapping aromatic rings. An initial intermolecular separation of 3.3 Å was chosen based on previously-calculated optimal exciplex separations.[10] The fluorescence emission energy ΔE_F represents the vertical transition energy at the minimum-energy geometry on the S_1 potential energy surface. The energy difference between ΔE_F and the monomer absorption energy ΔE_A represents the sum of the exciplex binding energy and the energy difference on the ground-state potential energy surface between the optimal ground-state geometry and the optimal S_1 geometry, often referred to as the repulsion energy. Coordinates for the minimum-energy S_1 structures are reported in [1]. The monomer bandgap or optical gap for monomers is calculated as the difference between the highest-occupied and lowest-unoccupied orbital energies (ΔE_{HL}) at the optimal ground state geometry, as recorded in the PAH Index.[24]

4.3 Results and Discussion

Tetracene Isomer Excimers

We begin our survey with an examination of homodimers composed of tetracene isomers, where molecular geometry represents the only degree of freedom. Electronic properties of each monomer are reported in Table 4.1, along with the shortened names that will be used in this work. Representative Clar structures[25] for each tetracene monomer, and the other PAH monomers considered, are illustrated in

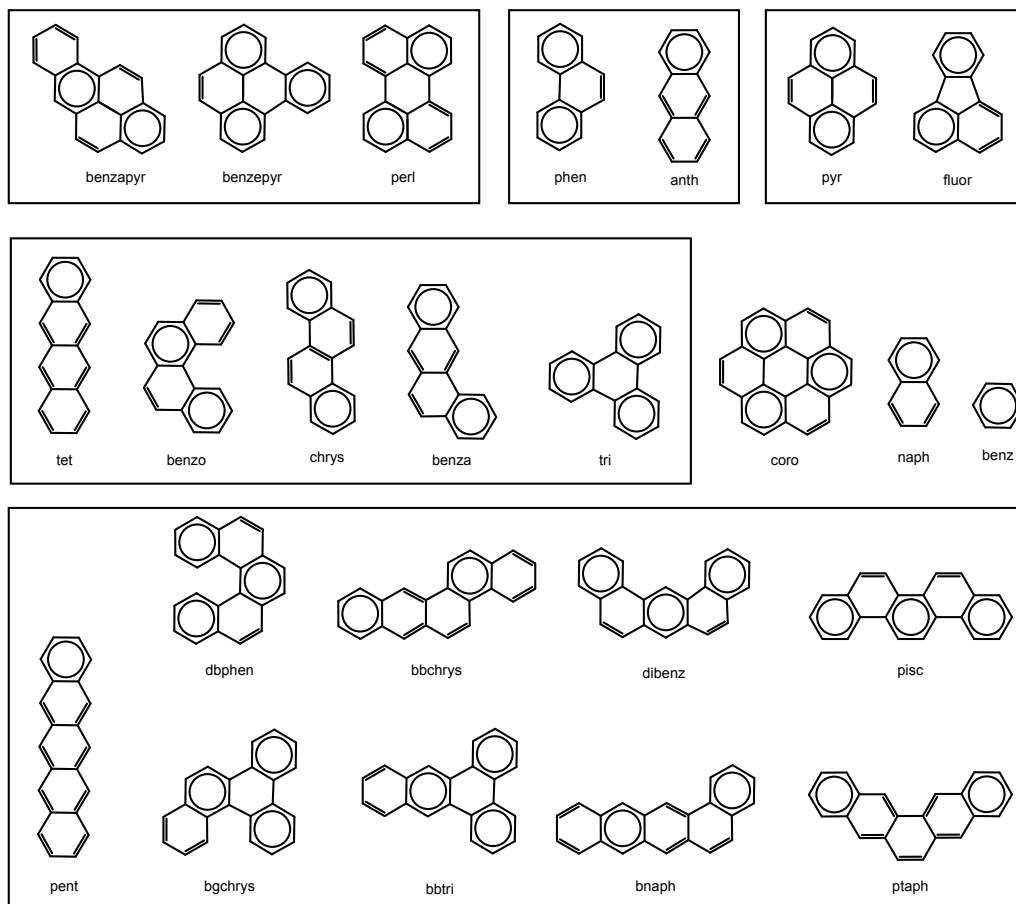


Figure 4.2: Clar structures[25] for the PAH monomers considered in this chapter. In each case, a representative Clar structure is shown, although multiple distributions of aromatic sextets may contribute to the overall electron density. Isomers are shown in the same box.

Fig. 4.2.

A strong stabilizing excimer interaction is observed for all of the isomers, corresponding to red shifts of about $30000\text{-}40000\text{ cm}^{-1}$ (Table 4.2). For four of the isomers, an almost perfectly linear relationship exists between ΔE_F for the excimer and ΔE_{HL} for the monomer (Fig. 4.3a). Replacing ΔE_{HL} with the ΔE_F values computed for the monomers yields another clearly linear relationship, albeit one with reduced explanatory power; the amount of variation in ΔE_F for the excimers explained by variation in monomer ΔE_F values is 85%, compared with 97% for ΔE_{HL} (Table 4.3).

The benzo exciplex emission energy is elevated relative to the chrys emission energy, despite a very similar ΔE_{HL} . This distinctive behavior may well stem from the

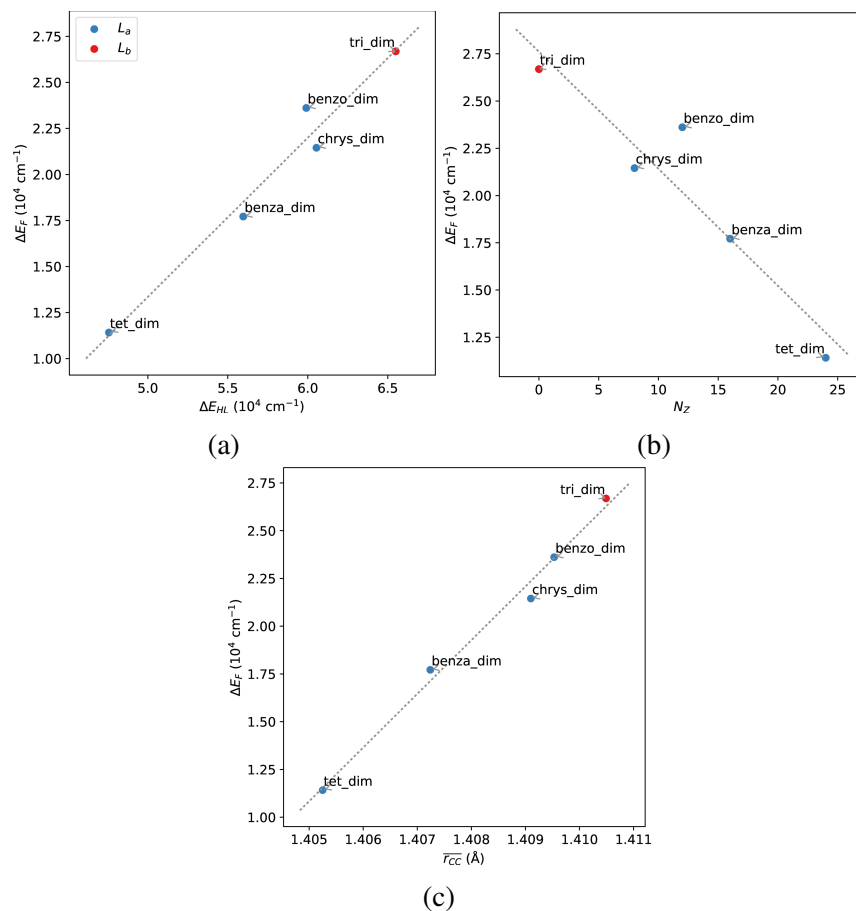


Figure 4.3: Variation in ΔE_F for excimers containing tet isomers with respect to ΔE_{HL} , N_Z , and $\overline{r_{CC}}$.

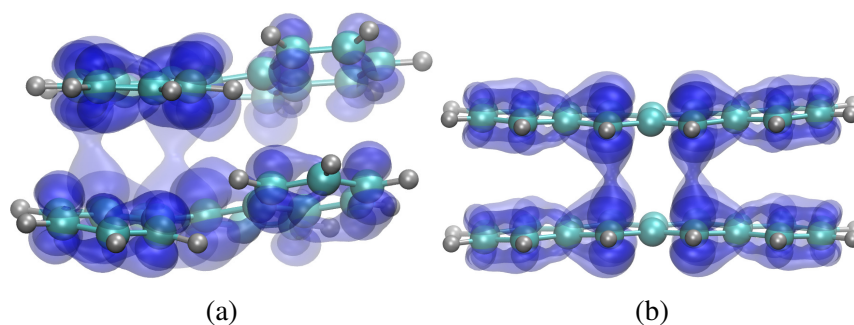


Figure 4.4: Orbitals involved in the $S_0 \rightarrow S_1$ transition for the benzo excimer (left) and the tet excimer (right), with ± 0.03 isosurfaces shown.

geometric differences—the benzo monomer has a u-shape, and the molecule is bent to prevent steric clashes between hydrogen atoms. Dihedral angles within the curve of the u are -13.2° and 15.6° , values that remain nearly identical upon excimer formation. The deviation of each monomer within the relaxed excimer from

perfectly planar geometry may be quantified using the planarity index, a measure based on the mean distance of atoms from a three-atom plane within the molecule, using the plane that minimizes this distance. A planarity index of 0 indicates a planar molecule.[26]

Benzo has by far the largest planarity index (Table 4.2), a level of distortion that contributes to large intermolecular distances between overlapping carbons in the excimer structure. C-C distances range from 3.24-3.96 Å, compared with 3.08-3.60 Å for chrys. Because the strength of the exciplex interaction depends on orbital overlap, which decays exponentially with internuclear separation, differences in intermolecular C-C distances of approximately 0.3 Å can have a noticeable impact on exciplex stabilization. The lack of frontier orbital electron density in the intermolecular region of the benzo excimer (Fig. 4.4a) compared with, for example, the tet excimer (Fig. 4.4b) is apparent. Monomers of the other tet isomers are also nonplanar in the minimum-energy excimer structure, but shorter C-C distances are maintained (3.18-3.54 Å for tet and 3.02-3.76 Å for benza).

The ordering of ΔE_{HL} energies in tet isomers is well-known, and has been rationalized using the PAHs' Clar structures (Fig. 4.2).[3] Clar structures are generated by placing benzene-like aromatic sextets (denoted by circles) in PAH rings and adding the remaining π electrons as double bonds. One aromatic sextet may be placed in each acene-like row of adjacent rings. Rings containing aromatic sextets are regarded as having higher local aromaticity. Large proportions of aromatic sextets and single bonds are associated with high ΔE_{HL} values, which generally correspond to higher thermodynamic and kinetic stability.[25] Among the tet isomers, the only possible Clar structure for tri displays both of these characteristics, and indeed tri has the highest ΔE_{HL} value of the isomers, while tet, with a single aromatic sextet and a number of double bonds, has the lowest.

For $C_{32}H_{16}$ PAHs, ΔE_{HL} has been shown to increase with the number of aromatic sextets, but the predictive value of sextet count alone is limited; for a given sextet number, ΔE_{HL} values vary by 1600–9700 cm^{-1} .[3] Three of the tet isomers have a sextet count of two. Quantitative descriptions of PAH edges offers another route to characterizing PAH topology. Mosbach and coworkers identify four types of PAH edge sites (Fig. 4.5).[27]

To obtain a one-dimensional ΔE_F model, we focus on a single edge type: zig-zag sites. Zig-zag sites are found along the central edges of linear acenes, distinct from the free edges found on both ends. The number of bonds that are part of zig-zag sites,

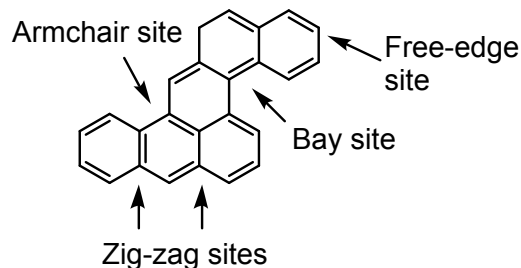


Figure 4.5: PAH edge groups identified by Mosbach and coworkers.[27]

N_Z , is different for each tet isomer, with the linear tet isomer having the maximum possible N_Z and the tri isomer having none. The N_Z value calculated for each excimer includes the number of zig-zag bonds present in both excimers. Emission energies from four of the excimers display a clear linear relationship with the number of zigzags (Fig. 4.3b), but the emission energy of benzo is again somewhat elevated as a result of the distortion caused by the bay edge group formed by the inside edge of the u.

Linear acenes also have the largest possible intramolecular C-C distances. We define the diameter D of a molecule to be the maximum intramolecular C-C distance and find a similar linear relationship between D and ΔE_F . N_Z slightly outperforms D as a predictor of ΔE_F , but the R^2 values obtained for each are similar.

Mean C-C bond length represents another structural feature correlated with aromaticity.[28] Here we use mean excited-state monomer bond length, which cannot be determined *a priori* like sextet number and requires a structure optimized in the excited state. Because this structure is the monomer, the resources required to calculate $\overline{r_{CC}}$ are significantly smaller than those required for the complex ΔE_F calculation. The correlation coefficient R^2 obtained from the linear fit of ΔE_F with respect to $\overline{r_{CC}}$ (Fig. 4.3c) indicates that 99% of the variation in ΔE_F may be explained by its relationship with $\overline{r_{CC}}$ (Table 4.3), making it the most successful single geometry descriptor. Substituting mean ground-state bond length decreases R^2 to 0.03, underlining the significant differences in geometry and aromaticity between the two states.

Pentacene Isomer Excimers

To extend our exploration of topology effects on ΔE_F , we have considered a representative subset of the 12 isomers of pentacene. The linear relationship between ΔE_F and ΔE_{HL} is clear (Fig. 4.6a), and for pentacene, ΔE_{HL} is the most accurate

Table 4.1: Electronic properties for constituent monomers of the complexes considered in this work.

Monomer	Shortened name	Formula	ΔE_{HL} (cm ⁻¹)	Excitation type	ΔE_F (cm ⁻¹)
coronene	coro	C ₂₄ H ₁₂	56997	<i>L_b</i>	26589
pyrene	pyr	C ₁₆ H ₁₀	57178	<i>L_b</i>	30193
tetracene	tet	C ₁₈ H ₁₂	47567	<i>L_a</i>	21983
benz[a]anthracene	benza	C ₁₈ H ₁₂	55965	<i>L_a</i>	28450
benzo[c]phenanthrene	benzo	C ₁₈ H ₁₂	59906	<i>L_b</i>	28935
benzene	benz	C ₆ H ₆	87843	<i>L_b</i>	42845
naphthalene	naph	C ₁₀ H ₈	67239	<i>L_b</i>	35549
phenanthrene	phen	C ₁₄ H ₁₀	66162	<i>L_b</i>	31827
anthracene	anth	C ₁₄ H ₁₀	54428	<i>L_a</i>	27397
benz[e]pyrene	benzepyr	C ₂₀ H ₁₂	57374	<i>L_b</i>	29420
benz[a]pyrene	benzapyr	C ₂₀ H ₁₂	51990	<i>L_a</i>	26667
fluoranthene	fluor	C ₁₆ H ₁₀	58859	<i>L_a</i>	22784
triphenylene	tri	C ₁₈ H ₁₂	65499	<i>L_b</i>	31466
chrysene	chrys	C ₁₈ H ₁₂	60542	<i>L_b</i>	30093
dibenz[a,j]anthracene	dibenz	C ₂₂ H ₁₄	56056	<i>L_b</i>	27739
benzo[b]triphenylene	bbtri	C ₂₂ H ₁₄	56018	<i>L_b</i>	29257
benzo[b]chrysene	bbchrys	C ₂₂ H ₁₄	52975	<i>L_a</i>	26462
benzo[a]naphthacene	bnaph	C ₂₂ H ₁₄	47891	<i>L_a</i>	22957
pentacene	penta	C ₂₂ H ₁₄	41668	<i>L_a</i>	18332
perylene	perl	C ₂₀ H ₁₂	48924	<i>L_a</i>	23680
pentaphene	pentaph	C ₂₂ H ₁₄	55289	<i>L_b</i>	26406
picene	pice	C ₂₂ H ₁₄	59511	<i>L_b</i>	28902
benzo[g]chrysene	bgchrys	C ₂₂ H ₁₄	57674	<i>L_b</i>	28563
dibenzo[c,g]phenanthrene	dbphen	C ₂₂ H ₁₄	58548	<i>L_b</i>	26867

predictor of ΔE_F . The ordering obtained for monomer ΔE_{HL} is in good agreement with recent TDDFT results.[29] Again, ΔE_{HL} performs better than ΔE_F for the monomer as a predictor of excimer emission energy (Table 4.3).

For the geometric descriptors, though, the picture becomes more complicated. Several of the isomers have bay edge groups, but the location of the bay is important in determining the S₁ excimer geometry. Bnaph and bbchrys each have a single edge group and nonplanar monomers—intermolecular C-C distances for bnaph and bbchrys range from 3.19-3.81 Å and 3.11-3.82 Å, respectively. The carbon atoms separated by the largest intermolecular distances are the ones on the end of the shorter continuous acene segment, which is one ring long for bnaph and two rings long for bbchrys.

One isomer, dbphen, even includes a fjord group. As with benzo, the planar structure

Table 4.2: Electronic and geometric properties of noncovalent homodimers.

Monomer	Monomer planarity	Excitation type	ΔE_F (cm ⁻¹)
tet	0.070	L_a	11416
benza	0.053	L_a	17715
benzo	0.231	L_a	23987
coro	0.005	L_b	21608
anth	0.061	L_a	16303
naph	0.036	L_a	23719
benzepyrr	0.027	L_a	21432
benzapyrr	0.044	L_a	16152
pyr	0.027	L_a	20040
phen	0.008	L_b	26267
fluor	0.020	L_a	19406
tri	0.007	L_b	26688
chrys	0.081	L_a	21450
dibenz	0.052	L_a	18560
bbtri	0.047	L_b	17718
bbchrys	0.048	L_a	15891
bnaph	0.062	L_a	11752
penta	0.072	L_a	7365
perl	0.013	L_a	14128
pentaph	0.018	L_a	19566
pice	0.025	L_a	22558
benz	0.007	L_b	32862
bgchrys	0.331	L_a	21322
dbphen	0.5814	L_a	24820

Table 4.3: R^2 values for the complex descriptors.

Descriptor	Tet Isomers	Pent Isomers	Naph containing	All
$\overline{\Delta E_{HL}}$	0.967	0.935	0.742	0.783
$\overline{\Delta E_F}$	0.863	0.712	0.688	0.758
\overline{D}	0.774	0.482	0.183	0.539
N_O	–	–	–	0.328
N_Z	0.885	0.507	0.390	0.486
$\overline{r_{CC}}$	0.990	0.755	0.819	0.471
M	–	–	0.173	0.343

is distorted to prevent steric clashes between hydrogen atoms, with dihedral angles of approximately $\pm 17^\circ$ for the carbon atoms in the fjord edge group. The dbphen

Table 4.4: Electronic and geometric properties of noncovalent heterodimers.

Larger monomer	Smaller monomer	Planarity		Excitation type	ΔE_F (cm ⁻¹)
		large mon	small mon		
coro	pyr	0.021	0.013	L_b	24516
tet	benz	0.063	0.003	L_a	21299
naph	benz	0.006	0.005	L_b	33411
phen	benz	0.007	0.001	L_b	31230
coro	naph	0.017	0.010	L_b	26001
coro	phen	0.022	0.007	L_b	25094
pyr	naph	0.041	0.014	L_b	25214
fluor	naph	0.038	0.017	L_a	21358
fluor	anth	0.044	0.010	L_a	19384
phen	naph	0.031	0.029	L_a	24882
anth	phen	0.043	0.049	L_a	22676
pyr	phen	0.019	0.012	L_a	22873
chrys	naph	0.072	0.006	L_a	26504
benza	naph	0.023	0.026	L_a	21664
benzapyr	naph	0.071	0.013	L_a	22306
anth	naph	0.034	0.031	L_a	20653
anth	benz	0.037	0.004	L_a	26631
pyr	benz	0.009	0.001	L_b	29789
tet	naph	0.009	0.016	L_a	18192
tri	naph	0.016	0.004	L_a	28417
benza	anth	0.042	0.052	L_a	16981
pyr	anth	0.061	0.010	L_a	21160
fluor	benz	0.005	0.003	L_a	22046
coro	anth	0.038	0.022	L_a	22447
coro	benz	0.018	0.001	L_b	26364
perl	naph	0.040	0.017	L_a	21706

excimer structure breaks the twofold symmetry of the dimer, leading to very large intermolecular C-C distances of up to ≈ 5.5 Å. This unexpected conformation means that ΔE_F is much higher than predicted by the simple N_Z descriptor. The ΔE_{HL} descriptor also underestimates ΔE_F , as was observed for the benzo excimer, which shares the dbphen excimer's twisted conformation.

In contrast, pentaph monomers have higher symmetry and are quite planar; the intermolecular C-C distances are 3.37-3.51 Å. Even pice, which has the maximum number of bay groups possible, has a larger monomer planarity index. The length of even the shortest C-C distance decreases the extent of intermonomer orbital

overlap, leading to a much higher ΔE_F than the geometry descriptors predict. This planarity may result from the relatively small, equal number of rings in each acene-like segment of the molecule. The tendency to undergo stabilizing distortion away from planar conformations tends to emerge for molecules containing one longer acene-like segment. Although nearly 70% of the variation in ΔE_F is attributable to its linear relationship with N_Z , the value of D as a monomer descriptor has been lost with the increasing geometric complexity. R^2 for the relationship between D and ΔE_F is less than 0.5.

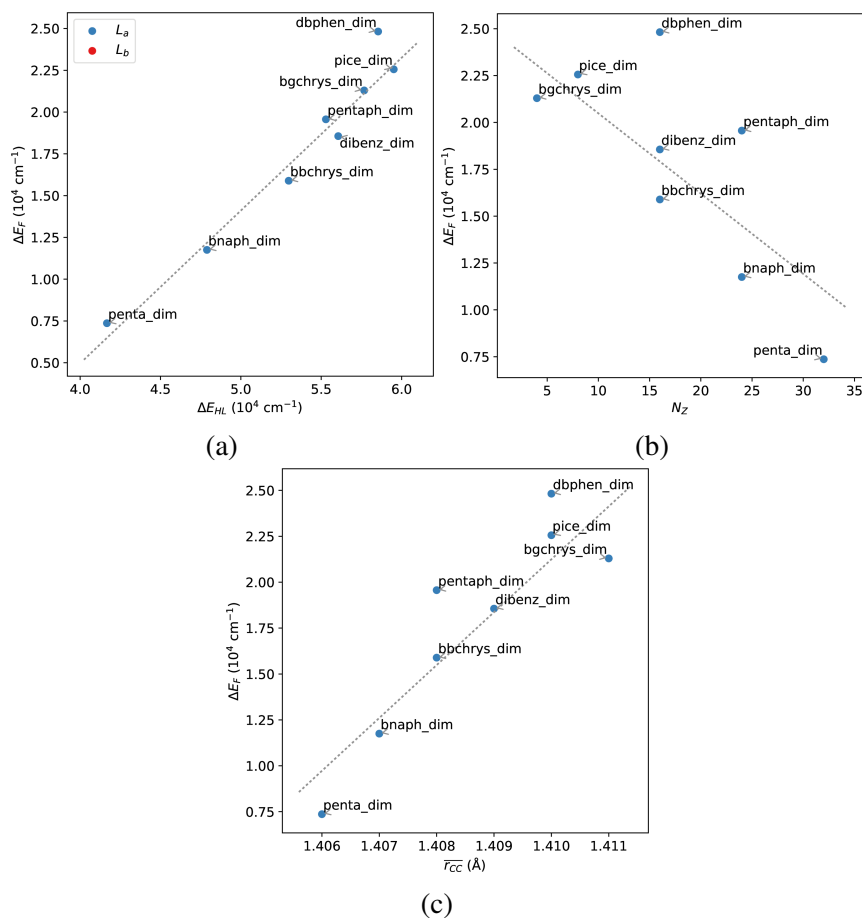


Figure 4.6: Variation in ΔE_F for excimers containing pent isomers with respect to ΔE_{HL} , N_Z , and $\overline{r_{CC}}$.

Exciplexes Containing Naphthalene

Next, we consider naph-containing homo- and heterodimers, allowing the mass and geometry of one of the monomers to vary. The naph monomer is generally expected to be present in relatively high concentrations in flames, and the small size allows examination of a number of complexes at reasonable computational cost. In

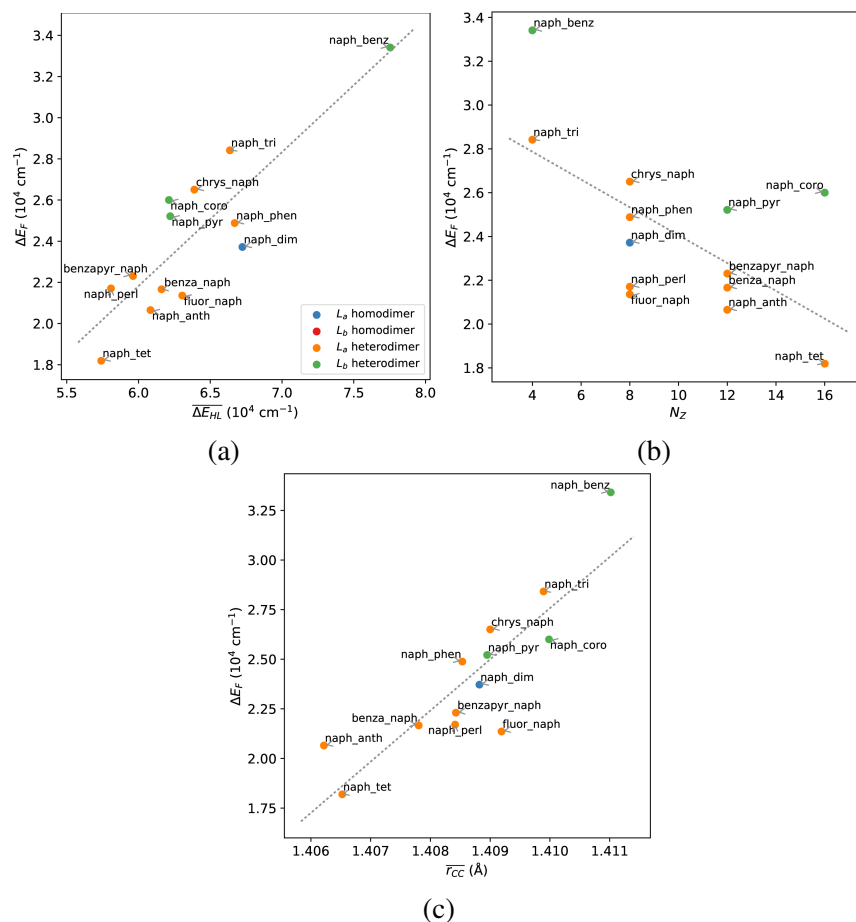


Figure 4.7: Variation in ΔE_F for complexes containing naphthalene with respect to ΔE_{HL} , N_Z , and r_{CC} .

some cases, more than one eclipsed configuration is possible. Because emissions from the global minimum configurations are expected to dominate due to relaxation on the S_1 surface, additional local minimum S_1 geometries are not considered. Minimum-energy geometries are illustrated in Fig. 4.9.

In place of ΔE_{HL} , we introduce the simple arithmetic mean of the HOMO-LUMO gap for the two monomers in each complex, $\overline{\Delta E_{HL}}$, which is equal to ΔE_{HL} for homodimers. $\overline{\Delta E_{HL}}$ may be used to predict ΔE_F within $\approx 3000 \text{ cm}^{-1}$. In total, the variation in $\overline{\Delta E_{HL}}$ for the complexes accounts for 71% of the variation in ΔE_F . The remaining variation may be attributed to the specifics of each interaction, in particular the amount of constructive orbital overlap possible given the geometric differences of the two monomers and the magnitude of the noncovalent interaction between the two. The naph excimer has the lowest-energy emission relative to the overall trend, which is not surprising given the high symmetry and perfect overlap

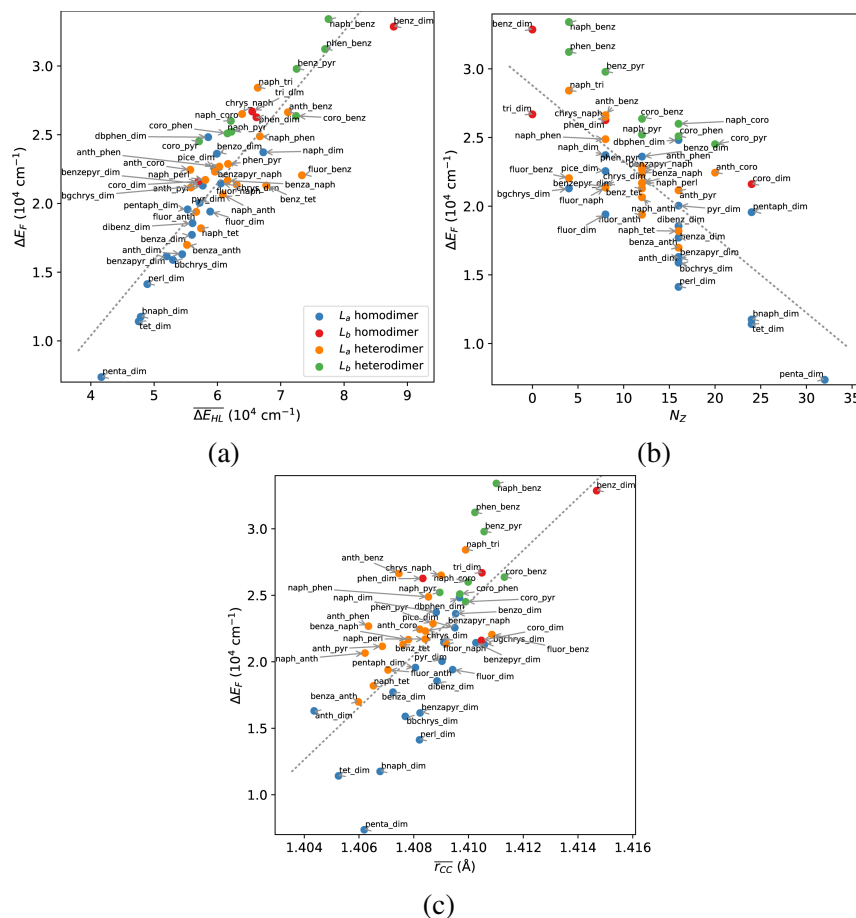


Figure 4.8: Variation in ΔE_F for all complexes with respect to $\overline{\Delta E_{HL}}$, N_Z , and $\overline{r_{CC}}$.

of the complex. At the other extreme, the naph-coro exciplex has the highest energy. N_Z , the total number of bonds in zig-zag sites over both monomers, largely fails as a predictor of ΔE_F . When the number of rings is allowed to vary, the number of possible PAH monomers with equal numbers of bonds in zig-zag edge groups is high; naph, phen, fluor, and chrys each have four. The r_{CC} descriptor is more successful, with $R^2 = 0.81$. The largest deviation from this linear trend is observed for the naph-fluor exciplex, which is not surprising given the presence of aliphatic bonds in the fluor molecule linking the naph- and benz-like groups.

The Complete Excimer and Exciplex Database

Now we allow both monomers to vary in mass and geometry. The heterodimer combinations chosen form a representative subset of the complexes that may be formed from the smallest PAHs, which are suggested to be present at higher concentration in flames based on kinetic estimates.[30]

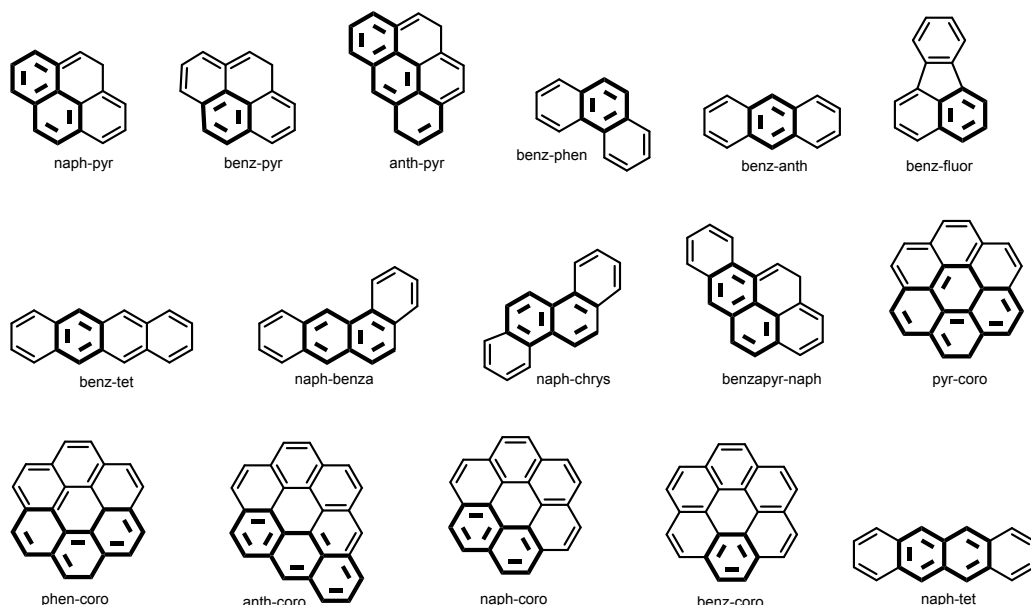


Figure 4.9: Minimum-energy excited-state geometries for heterodimer structures with multiple local minimum configurations.

The relationship between $\overline{\Delta E_{HL}}$ and ΔE_F holds surprisingly well, as Fig. 4.8a shows. This linear relationship explains approximately 80% of the variation in ΔE_F . The complexes emitting at the lowest energies relative to the overall trend are generally homodimers; the benz dimer in particular has a ΔE_F approximately 5000 cm^{-1} lower than predicted from $\overline{\Delta E_{HL}}$. The coro-pyr dimer has the highest-energy emission compared to the predicted value. For heterodimers, the lowest-energy configuration typically has the smaller molecule centered over the larger molecule, minimizing the mean intermolecular C-C distance. This is not the case for the naph-coro, phen-coro, or anth-coro complexes, where the most favorable configurations avoid the central “hole,” a ring that has neither an aromatic sextet nor double bonds. For pyr, avoiding overlap with the hole means that two pyr rings extend past the edge of the coro monomer, a geometry even less favorable than the centered one. This example illustrates the value of Clar structures in rationalizing ΔE_F observations, even if sextet counts are not used in quantitative models. The most noticeable ΔE_F underestimates are observed for the benz-fluor and benz-tet complexes. Because the HOMO energy for benz is significantly higher than for either fluor or tet, the excitations remain localized on the larger chromophores, as has been observed for the benz-anth exciplex.[10]

For the complete database of complexes, the variation in ΔE_F associated with the geometric descriptors is again much lower than observed in each isomer group, with

$R^2 = 0.49$ for the relationship between ΔE_F and N_Z . This is not surprising, given the broader array of PAH topologies present. The introduction of pericondensed molecules and the presence of heterodimers complicates the relationship between N_Z and PAH topology, with N_Z identical for complexes as electronically dissimilar as the chrys dimer and the benz-pyr complex. It is not clear whether including more edge group counts in the model would improve agreement—edge topology is, if anything, more diverse for the larger tet and pent isomers.

Considering the monomer-mass-weighted $\overline{r_{CC}}$ (Fig. 4.8c) does not improve the correlation coefficient—like N_Z , this relationship accounts for about 50% of the ΔE_F variation. Examining $\overline{r_{CC}}$ values also reveals an unexpected trend in excited-state monomer geometries. In general, ground-state C-C bond lengths increase with increasing PAH mass, but the longest S_1 $\overline{r_{CC}}$ is the one obtained for benz, with the shortest values obtained for anth and tet. In general, $\overline{r_{CC}}$ is longer for complexes with L_b $S_0 \rightarrow S_1$ transitions and shorter for complexes with L_a transitions. The arithmetic mean of the monomer diameters, \overline{D} , has similar predictive power, with $R^2 = 0.54$ for the linear relationship between \overline{D} and ΔE_F .

Though the geometry-based models used here have limited predictive power, each is still more useful than a one-dimensional model based on total complex mass M , which accounts for only 34% of the variation in ΔE_F . This level of success for the M -based model is likely explained by the fact that linear acenes, which are over-represented among small PAHs and thus over-represented in this database, do have $\overline{\Delta E_{HL}}$ values that decrease with increasing mass. The wide variation of ΔE_F among tet isomers and among pent isomers shows that mass is often useless in predicting ΔE_F . Similarly, the number of intermonomer C-C pairs that directly overlap, N_O , which we define as being separated by a distance of $< 0.25 \text{ \AA}$ in the plane of the monomers, has little predictive value, with $R^2 = 0.33$ for its linear relationship with ΔE_F .

Aliphatically-Bridged Complexes

Finally, we examine the possibility that PAHs connected by aliphatic linkers could be the source of visible-range fluorescence. MD/metadynamics simulations suggest that aliphatically-bridged PAHs have lower homodimerization propensity than similarly-sized PAHs that do not contain sp^3 carbons,[31] but intramolecular exciplex formation can occur without dimerization. Substitution with saturated hydrocarbon groups has a significant effect on the noncovalent dimerization propensity

of PAHs,[32] but the effect on PAH monomer electronic structure is expected to be small.[33] However, because orbital overlap is so critical to the stabilizing exciplex interaction, we would expect that if the presence of the linker disrupted the eclipsed configuration of the PAH sufficiently, this stabilization would be eliminated. Maintaining the eclipsed configuration entails significant angle strain for the aliphatic linker. In a study of the conformations of benzene molecules with attached aliphatic chains, the aliphatic chain had to be at least eight carbons in length for a conformation with the chain folded on top of the benzene to be observed at 110 °C.[34] At flame temperature, a wide range of conformational states are likely to be accessible to vibrationally-excited linked complexes. Our goal is not to calculate the relative free energy of the eclipsed conformation, but simply to determine the effect of the linker on the minimum-energy sandwich-like excited state structure and on the fluorescence emission energy for that structure.

Considering all possible linker lengths and positions for every complex in our noncovalent database is beyond the scope of this work. Instead, we have chosen a representative subset of structures from across the spectrum: the benz excimer, the benz-naph exciplex, the naph-anth exciplex, and the naph and anth excimers. Bridged structures suggested to be consistent with recent tandem mass spectrometry results include linkers with one to four carbons,[35] but we have confined our survey to complexes with two-to-four carbon linkers, where excimer formation produces less angle strain. Linker attachment points at the endmost carbon (α position), one carbon closer to the molecule center of mass (β position), and two carbons closer to the center of mass (γ position) have been considered. In each case, the attachment point is the same for both molecules.

Fluorescence wavelengths of the linked structures are reported in Table 4.5 and Figure 4.10. Often, the effect of the covalent linker on ΔE_F is small, particularly for two- and four-C linkers. The linkers generally lower ΔE_F , with the strongest effect observed for C3 linkers. Examining the minimum-energy S_1 structures and frontier orbital isosurfaces obtained for the linked benz excimer (Fig. 4.11) reveals why this is the case. The C2 linker disrupts the parallel eclipsed structure of the monomers. Intermolecular C-C distances range from 2.54 Å for the Cs closest to the linker to 3.24 Å; the noncovalent excimer has C-C distances ranging from 2.96-2.98 Å. The C2 frontier orbitals (Fig. 4.11a) show reduced intermonomer electron density in the region with the largest C-C distances, farthest away from the linker. The similarity of the ΔE_F values obtained for the noncovalent and C2 structures is likely due in

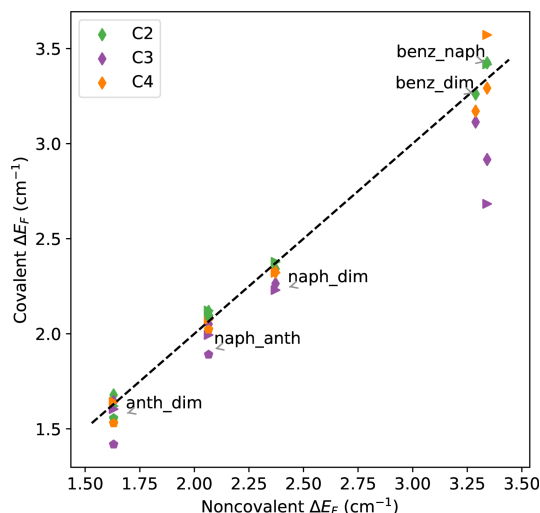


Figure 4.10: Emission energies for aliphatically-bridged complexes vs. emission energies for the corresponding noncovalent complexes. Diamonds indicate linkers on α carbons, triangles indicate β carbons, and pentagons indicate γ carbons. A dotted $x = y$ curve has been added.

part to a partial delocalization of the orbitals involved in the transition (in particular the LUMO+1 orbital) over the linker carbons. Because we have calculated vertical fluorescence energies, it is also likely that the lower ΔE_F results in part from higher repulsion energy on the ground-state potential energy surface. Benz dimers with C3 and C4 linkers have nearly-intact eclipsed structures, with 2.80-3.14 Å C-C distances (Figs. 4.11b and 4.11c). The C3 structure has the slightly lower-energy emission and more extensive frontier orbital electron density delocalization over the linker. The one structure where the energetic impact of the aliphatic linker is significant is the benz-naph exciplex with a C3 linker in the β position. ΔE_F is lowered by nearly 7500 cm $^{-1}$. In this case, the eclipsed configuration is maintained, and the order of the two lowest-energy singlet excited states flips; the L_a state becomes lower in energy than the L_b state.

The range of energies obtained for each complex generally decreases in size as mass increases. For the naph dimer, the linker position has virtually no impact on ΔE_F . In contrast, ΔE_F for the anth dimer is noticeably decreased for linkers in the γ position. The optimal S_1 geometry for the anth dimer is already nonplanar, with the central carbons of the two molecules closest together (3.05 Å) and the end carbons farther apart (3.41 Å). This geometry is perturbed the least when the linker is bound to the central carbons.

Of course, ΔE_F is not the only aspect of the electronic transition affected by the

addition of a linker. The oscillator strength for the fluorescence emission from most of the noncovalent homodimers is equal to zero for symmetry reasons. At flame temperature, intra- and intermolecular dimer modes are expected to be excited, resulting in nonzero oscillator strengths. The aliphatically-bridged structures, on the other hand, have nonzero oscillator strengths even in their minimum-energy S_1 geometries. Changing the position or length of the linker can cause the oscillator strength to vary by two orders of magnitude.[1]

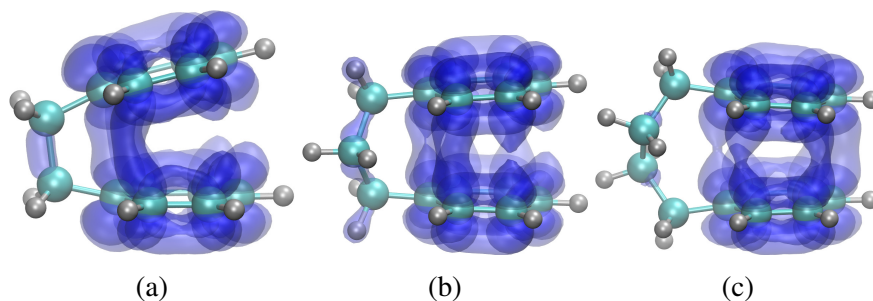


Figure 4.11: Orbitals involved in the $S_0 \rightarrow S_1$ transition for aliphatically-bridged benz dimers, with ± 0.05 isosurfaces shown.

References

- (1) Krueger, R. A.; Blanquart, G. *Phys. Chem. Chem. Phys.* **2019**, *21*, 10325–10335.
- (2) Kholghy, M. R.; Kelesidis, G. A.; Pratsinis, S. *Phys. Chem. Chem. Phys.* **2018**, *20*, 10926–10938.
- (3) Adkins, E. M.; Miller, J. H. *Phys. Chem. Chem. Phys.* **2017**, *19*, 28458–28469.
- (4) Ruiz-Morales, Y. *J. Phys. Chem. A* **2002**, *106*, 11283–11308.
- (5) Shirai, S.; Kurashige, Y.; Yanai, T. *J. Chem. Theory Comput.* **2016**, *12*, 2366–2372.
- (6) Plasser, F.; Lischka, H. *J. Chem. Theory Comput.* **2012**, *8*, 2777–2789.
- (7) Prlj, A.; Sandoval-Salinas, M. E.; Casanova, D.; Jacquemin, D.; Corminboeuf, C. *J. Chem. Theory Comput.* **2016**, *12*, 2652–2660.
- (8) Grimme, S.; Parac, M. *Chemphyschem* **2003**, *4*, 292–295.
- (9) Leininger, T.; Stoll, H.; Werner, H.-J.; Savin, A. *Chem. Phys. Lett.* **1997**, *275*, 151–160.
- (10) Krueger, R. A.; Blanquart, G. *J. Phys. Chem. A* **2019**, *123*, 1796–1806.
- (11) Kuritz, N.; Stein, T.; Baer, R.; Kronik, L. *J. Chem. Theory Comput.* **2011**, *7*, 2408–2415.

Table 4.5: Emission energies for covalently-linked structures.

Complex	Linker position	Linker length	Excitation type	ΔE_F (cm ⁻¹)
anth dimer	2	α	L_a	16972
	2	β	L_a	16200
	2	γ	L_a	15564
	3	α	L_a	16431
	4	β	L_a	16426
	3	γ	L_a	14184
	3	β	L_a	16038
anth-naph complex	4	γ	L_a	15300
	2	β	L_a	21222
	3	β	L_a	19936
	4	β	L_a	20747
	2	γ	L_a	20921
	3	γ	L_a	18907
	4	γ	L_a	20227
naph dimer	2	α	L_a	21173
	3	α	L_a	20509
	2	α	L_a	23414
	3	α	L_a	22640
	4	α	L_a	23240
	3	β	L_a	22297
	4	β	L_a	23629
benz-naph complex	2	β	L_a	23781
	2	α	L_b	34247
	3	α	L_a	29163
	2	β	L_b	34165
	3	β	L_a	26831
benz dimer	4	β	L_a	35714
	4	α	L_a	30912
	4	α	L_b	31706
	2	α	L_b	32605
	3	α	L_a	31133

- (12) Stein, T.; Kronik, L.; Baer, R. *J. Am. Chem. Soc.* **2009**, *131*, 2818–2820.
- (13) Grimme, S. *J. Chem. Phys.* **2006**, *124*, 034108.
- (14) Head-Gordon, M.; Rico, R. J.; Oumi, M.; Lee, T. J. *Chem. Phys. Lett.* **1994**, *219*, 21–29.
- (15) Caricato, M.; Trucks, G. W.; Frisch, M. J.; Wiberg, K. B. *J. Chem. Theory Comput.* **2011**, *7*, 456–466.

- (16) Wong, Z. C.; Fan, W. Y.; Chwee, T. S.; Sullivan, M. B. *Phys. Chem. Chem. Phys.* **2017**, *19*, 21046–21057.
- (17) Weigend, F.; Ahlrichs, R. *Phys. Chem. Chem. Phys.* **2005**, *7*, 3297–3305.
- (18) Laurent, A. D.; Blondel, A.; Jacquemin, D. *Theor. Chem. Acc.* **2015**, *134*, 1–11.
- (19) Krueger, R. A.; Blanquart, G. *Int J Quantum Chem* **2018**, DOI: 10.1002/qua.25819.
- (20) Neese, F. *Wiley Interdiscip. Rev. Comput. Mol. Sci.* **2012**, *2*, 73–78.
- (21) Iyer, E. S. S.; Sadybekov, A.; Lioubashevski, O.; Krylov, A. I.; Ruhman, S. *J. Phys. Chem. A* **2017**, *121*, 1962–1975.
- (22) Dubinets, N. O.; Safonov, A. A.; Bagaturyants, A. A. *J. Phys. Chem. A* **2016**, *120*, 2779–2782.
- (23) Casanova, D. *Int. J. Quantum Chem.* **2015**, *115*, 442–452.
- (24) NIST The NIST Polycyclic Aromatic Hydrocarbon Structure Index., <http://pah.nist.gov>.
- (25) Clar, E., *Polycyclic Hydrocarbons*; Springer Berlin Heidelberg: Germany, 1964.
- (26) Antić, M.; Furtula, B.; Radenković, S. *J. Phys. Chem. A* **2017**, *121*, 3616–3626.
- (27) Mosbach, S.; Celnik, M. S.; Raj, A.; Kraft, M.; Zhang, H. R.; Kubo, S.; Kim, K. O. *Combust. Flame* **2009**, *156*, 1156–1165.
- (28) Fortenberry, R. C.; Novak, C. M.; Lee, T. J.; Bera, P. P.; Rice, J. E. *ACS Omega* **2018**, *3*, 16035–16039.
- (29) Jones, L.; Lin, L. *J. Phys. Chem. A* **2017**, *121*, 2804–2813.
- (30) Wang, H. *Proc. Combust. Inst.* **2011**, *33*, 41–67.
- (31) Elvati, P.; Turrentine, K.; Violi, A. **2017**.
- (32) Elvati, P.; Violi, A. *Proc. Combust. Inst.* **2013**, *34*, 1837–1843.
- (33) Chen, D.; Wang, H. *Proc. Combust. Inst.* **2018**, *000*, 1–7.
- (34) Hewett, D. M.; Bocklitz, S.; Tabor, D. P.; Sibert, E. L.; Suhm, M. A.; Zwier, T. S. *Chem. Sci.* **2017**, *8*, 5305–5318.
- (35) Adamson, B. D.; Skeen, S. A.; Ahmed, M.; Hansen, N. *J. Phys. Chem. A* **2018**, *122*, 9338–9349.

PREDICTING THE PHOTORESPONSE OF SOOT NUCLEI: SPECTROSCOPIC CHARACTERISTICS OF AROMATIC AGGREGATES CONTAINING FIVE-MEMBERED RINGS

5.1 Introduction

Prior work on the electronic structure of PAH aggregates, including fluorescence emission from exciplex states, has focused on molecules containing only six-membered aromatic rings (e.g., naphthalene and pyrene) and six-membered rings connected by single C-C bonds (e.g., fluoranthene and perylene).[1–3] The photoreponses of complexes containing molecules with either cyclopenta-fused rings, such as acenaphthylene, or cyclopentadienyl groups, such as indene, have not been characterized. However, the presence of molecules containing these groups in flames has been supported by a number of mass spectrometry,[4–6] gas chromatography and mass spectrometry,[7] atomic force microscopy,[8] detailed kinetic modeling (e.g., [9] and [10]), and stochastic simulation studies.[4, 11] Decompositions of planar LIF spectra also include contributions from molecules with cyclopentadienyl groups.[12] Sometimes the concentration of molecules with five-membered ring groups is larger than the concentration of the parent PAH.[9, 12]

In order to determine how the energetics of exciplex formation in complexes containing chromophores with five-membered rings compares to the process in the corresponding complexes containing only six-membered rings, we will examine fluorescence energies and optimal excited-state geometries calculated using time-dependent density functional theory (TDDFT) for ten complexes containing cyclopentadiene, indene, and/or acenaphthylene. Spectroscopically-relevant excited- and ground-state binding energies and repulsion energies are also included. Taken together, these energies can shed light on the distinctive impact of each type of five-membered ring group on PAH complex photoresponse.

5.2 Computational Methods

All spectroscopic parameters involving excited states were computed with TDDFT using tuned[13, 14] versions of the long-range corrected BLYP functional (LC-BLYP-T)[15] with the def2-TZVP basis set.[16] This procedure has been shown to yield S_1 excitation and binding energies for PAH complexes that are in good

agreement with perturbatively-corrected multireference methods.[17] Values of the range-split parameter γ for monomers and complexes are reported in Tables S1-S3. DFT and TDDFT calculations were performed using the Orca electronic structure package[18] version 4.0.0. The Tamm-Dancoff approximation was applied, and grid size five was used.

Excited-state optimizations were started from eclipsed configurations, with aromatic rings overlapping as nearly as possible and an initial intermolecular separation of 3.3 Å. For complexes with low symmetry, optimizations were also performed for unique rotated configurations. Ground-state minimum energy configurations were determined using classical simulated annealing and optimization, followed by ground state DFT optimization using the LC-BLYP-T functional. Single-point energies were then calculated using the B2PLYP functional[19] with the D3 dispersion correction.[20] This functional has shown excellent performance in benchmarks involving noncovalent interactions.[21] To accelerate B2PLYP calculations, Coulomb integrals were evaluated using the resolution of identity (RI) approximation.[22] The simulated annealing process was carried out using the LAMMPS molecular dynamics package.[23] Atom velocities were initialized to random values drawn from the Maxwell-Boltzmann distribution for 150 K, the lowest temperature at which all of the noncovalent dimers are stable at infinite dilution. Temperature was lowered to 5 K over the course of the simulation using the Nosè-Hoover thermostat[24] with a time constant of 70 fs. A time step of 1 fs was used, with a total simulation time of 2 ns. All atomic interactions were modeled using the OPLS force field,[25] with parameters generated using the LigParGen server.[26]

Fig. 1.2 summarizes the relationship between the spectroscopic quantities calculated, which are introduced in Section 1.2. For reference geometries, we use an intermolecular separation of 10 Å, which is large enough for the interaction energy to become negligible. The shortened names that will be used to refer to monomers are given in Table 5.1.

5.3 Results and Discussion

Complexes in the Ground State

Although noncovalent complexes of small PAHs are not expected to be thermodynamically stable at flame temperature,[27–30] minimum-energy ground-state dimer configurations still represent an important reference point on the S_0 – S_1 potential energy surface, and formation of transient complexes may affect the rate at which

the first covalent bond is made.[9] The optimal S_0 geometries of the complexes are illustrated in Fig. 5.1. Most of the structures have “tilted T” conformations similar to the T-shaped structure generally agreed to be the global minimum configuration for the benzene dimer.[31–33] This conformation may increase stability through CH- π interactions between hydrogen atoms and the out-of-plane electron density present on the aromatic rings. It is important to note that noncovalent PAH complexes often have several potential energy minima, many of which are parallel-displaced configurations.[34, 35] By sampling initial dimer configurations from a molecular dynamics trajectory, we have explored a larger portion of the conformational space than is typically possible using grid searches across translation and rotation coordinates, but we cannot exclude the possibility that other minima with similar or even stronger binding energies exist.

Ground-state binding energies (Table 5.2) generally increase linearly in magnitude with increasing complex mass (Fig. 5.2). Linear regression analysis indicates that 76% of the variation in $E_{B,G}$ is explained by this linear relationship. The strongest binding is observed for the ind dimer, which, because of the additional hydrogen atoms on the unsaturated carbons, is able to maintain a parallel-twisted conformation while incorporating two CH-double bond interactions between the C5 groups. As expected, binding energies for all complexes are on the order of $k_B T$ (12.5 kJ/mol at 1500 K).

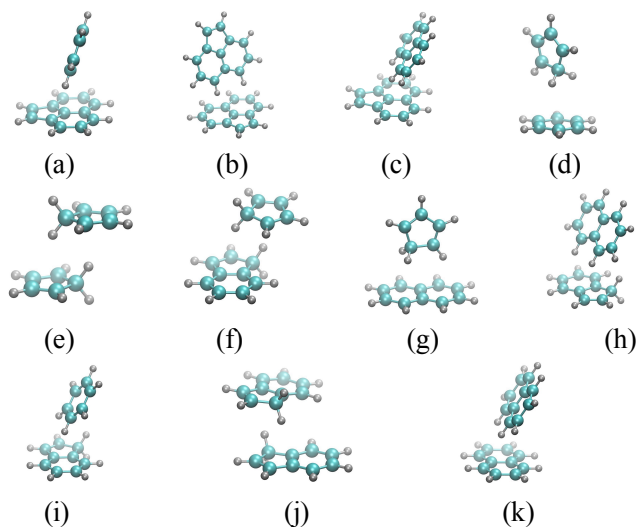


Figure 5.1: Complex structures optimized in the ground state for the (a) benz-ace complex, (b) ace dimer, (c) naph-ace complex, (d) cyclo-benz complex, (e) cyclo dimer, (f) cyclo-ind complex, (g) cyclo-naph complex, (h) naph-ind complex, (i) benz-ind complex, (j) ind dimer, and (k) naph dimer.

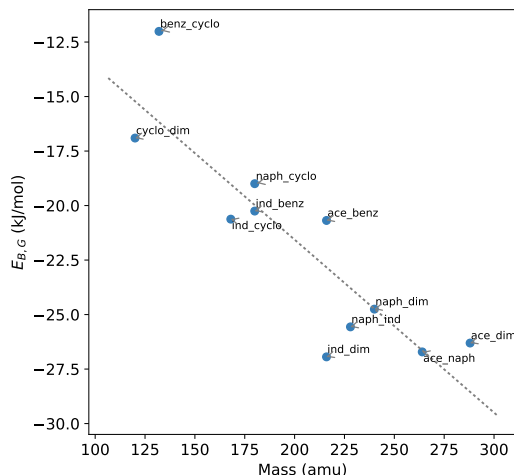


Figure 5.2: Ground state binding energies $E_{B,G}$ as a function of complex mass.

Monomer Electronic Structure

Characterizing monomer electronic structure is necessary to understand the photoreponse of aromatic complexes because the initial complex absorption energy is typically indistinguishable from the absorption energy of the constituent monomers,[36] although this approximation likely breaks down when initial monomer separation is small ($< 3.5 \text{ \AA}$).[3] Values for ΔE_A , ΔE_F , and the HOMO-LUMO gap for the ground state geometry ΔE_{HL} for each of the monomers are reported in Table 5.1. The $S_0 \rightarrow S_1$ transitions represent a mix of L_a (HOMO \rightarrow LUMO) and L_b (HOMO-1 \rightarrow LUMO+HOMO \rightarrow LUMO+1) transitions.

The lowest-energy transitions by far are observed for the ace monomer. Low-energy fluorescence emissions have also been observed for larger molecules containing cyclopenta-fused rings.[37] Although ace absorbs in the UV range, these larger structures could potentially account for visible-range absorption and emission behavior that is observed across flame regions.[1] With a difference of 107 kJ/mol between ΔE_A and ΔE_F , ace also displays the largest Stokes shift of any of the monomers. This shift reflects changes in each bond length, with the most dramatic changes observed in the cyclopenta-fused group, where the two single bonds are 0.08 \AA shorter in the excited-state structure and the double bond is 0.08 \AA longer. Taken together, the changes in bond length make the three bonds in the excited-state structure much more similar in length than in the ground state structure, which may indicate increased electron delocalization in the excited-state structure and thus increased aromaticity. Similar contracting of single bonds and lengthening of double bonds is observed for the cyclo monomer, which has an 102 kJ/mol Stokes shift.

Structures Containing Cyclopentadienyl Groups

The excited-state binding energies $E_{B,E}$ for the complexes considered in this work show markedly different behavior from the ground-state binding energies. The cyclo dimer, which contains the smallest monomers with the highest absorption energies (Table 5.1) has the highest $E_{B,E}$ of any complex considered. In the minimum-energy excited-state conformation (Fig. 5.3A), one monomer is rotated 180° with respect to the other, which alleviates the steric clashes between H atoms on the saturated carbon that would occur if the complex had the directly-overlapping sandwich geometry, which is the lowest-energy conformation for the six-membered ring excimers.

Planar in the ground state, the excited-state cyclo monomers are distorted, with a minimum intermolecular C-C distance (r_{CC}) of 2.38 Å—much shorter than is observed in PAH exciplexes, where distances of 3.0-3.5 Å are typical[17, 38, 39]—and a maximum r_{CC} of 2.96 Å. These short intermolecular distances allows significant orbital overlap, visible in isosurfaces of the frontier orbitals of the complex (Fig. 5.4 a), the driving force for the distortion. The combination of single and double bonds likely confers higher flexibility than is observed for PAHs, where π electrons are evenly delocalized. This flexibility is reflected in the planarity index[40] calculated for the excited-state cyclo dimer based on carbon atom coordinates (Table 5.2). A planarity index of zero indicates a perfectly planar molecule, with higher values indicating greater distortion. The monomers in the cyclo excimer show the highest nonplanarity of any excited-state complex. This highly nonplanar geometry is unfavorable in the ground state, though; the repulsion energy E_R for the cyclo dim is the highest for any complex. Strong excited-state binding and ground-state repulsion lead to a low fluorescence emission energy ΔE_F , the lowest calculated (Fig. 5.5).

Similar geometric distortion is observed for the excited-state cyclo-benz complex (Fig. 5.6C), although to a lesser degree—the planarity index for the benz monomer is 0.1428, compared with 0.1919 for the cyclo dim. The minimum r_{CC} observed is 2.59 Å, and analysis of the one-electron transition density matrix[41] shows higher electron and hole populations on the cyclo monomer (0.52 and 0.66, respectively, vs. 0.46 and 0.52 for the benz monomer). The lower electron density on the benz monomer is apparent from the frontier orbital isosurfaces (Fig. 5.4 b). These effects are associated with an $E_{B,E}$ value only a third as high as the one obtained for the cyclo dim. Nonetheless, ΔE_F is remarkably low for such a small complex—similar to ΔE_F for the pyrene dimer.[2]

This general pattern is repeated for the other structures containing cyclo groups.

Where cyclo groups overlap, as in the ind dimer and the cyclo-ind complex, the minimum-energy excited-state structure has some degree of distortion, and relatively high $E_{B,E}$ values are matched with high repulsion energies. Distortion of the monomers in the ind dimer is less extreme than distortion of the monomers in the cyclo dimer, and the ind-naph complex has nearly planar molecules. For the ind dimer, the conformation that places the two saturated carbon atoms on opposite sides of the complex is favored, as in the cyclo dimer. However, the addition of a six-membered ring decreases the relative rotation of the cyclo group, bringing the two six-membered groups closer to the eclipsed conformation favored for benz and naph excimers. Where cyclo groups overlap aromatic six-membered rings, excited-state binding is weaker, but E_R remains high, except for the ind-naph complex. Simultaneous variation in E_R and $E_{B,E}$ makes it difficult to generalize about ΔE_F for complexes in this group.

Table 5.1: Electronic properties of the monomers considered in this work.

Monomer	Shortened name	Excitation type	ΔE_{HL} (kJ/mol)	ΔE_A (kJ/mol)	ΔE_F (kJ/mol)
acenaphthylene	ace	L_a	8.6	327.5	220.4
benzene	benz	L_b	12.8	537.1	512.6
cyclopentadiene	cyclo	L_a	11.7	549.1	447.5
indene	ind	L_b	10.6	485.7	455.3
naphthalene	naph	L_b	10.0	449.7	425.3

Table 5.2: Spectroscopic parameters and excited state planarity descriptors for the complexes considered in this work.

Large monomer	Small monomer	Large mon planarity	Small mon planarity	Excitation type	ΔE_F (kJ/mol)	$E_{B,G}$ (kJ/mol)	E_R (kJ/mol)	$E_{B,E}$ (kJ/mol)
naph	naph	0.0355	0.0355	L_a	283.8	-17.3	62.9	-93.7
naph	ind	0.0138	0.0108	L_a	328.4	-19.9	40.9	-58.1
ind	ind	0.0831	0.0829	L_a	222.9	-20.8	122.9	-112.3
cyclo	cyclo	0.1919	0.1919	L_a	112.0	-16.1	220.9	-135.2
benz	cyclo	0.1428	0.1354	L_a	239.1	-9.4	173.5	-47.3
ind	benz	0.0379	0.1025	L_a	271.6	-16.6	142.0	-46.8
ind	cyclo	0.0618	0.1684	L_a	190.6	-18.0	157.9	-112.9
naph	cyclo	0.0924	0.1163	L_a	221.4	-14.6	136.5	-74.0
ace	ace	0.0199	0.0199	L_a	158.0	-18.7	59.4	-47.4
ace	benz	0.0043	0.0030	L_a	213.2	-15.4	37.8	-18.5
ace	naph	0.0080	0.0030	L_a	210.5	-17.1	38.9	-21.1

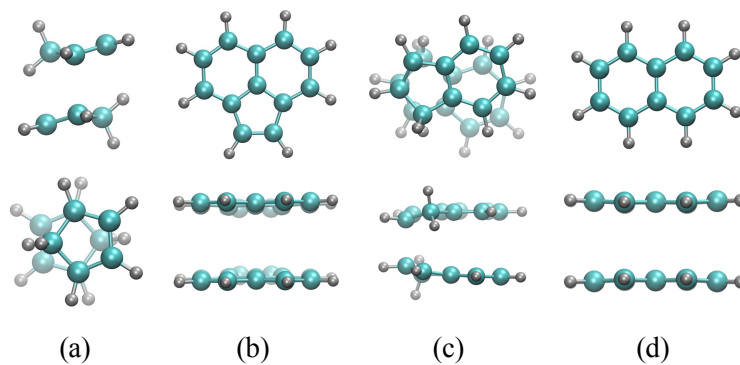


Figure 5.3: Homodimer structures optimized in the S_1 state for (a) cyclo, (b) ace, (c) ind, and (d) naph shown from top and side views.

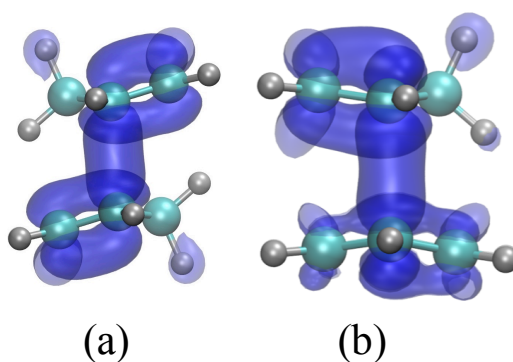


Figure 5.4: Orbitals involved in the $S_0 \rightarrow S_1$ transition for (a) the cyclo dimer and (b) the cyclo-benz complex, with ± 0.05 isosurfaces shown.

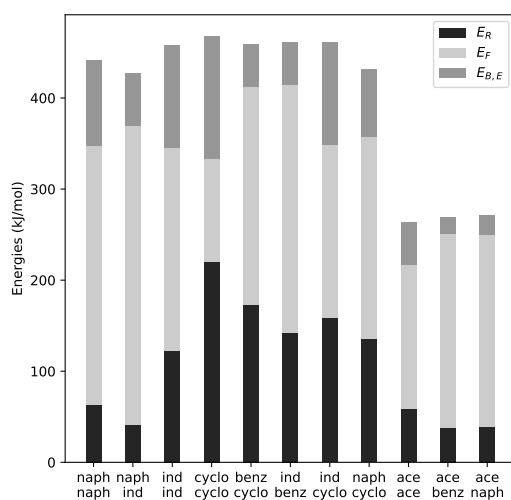


Figure 5.5: Partitioning of monomer absorption energy ΔE_A into repulsion energy E_R , fluorescence emission energy, ΔE_F , and excited-state binding energy $E_{B,E}$.

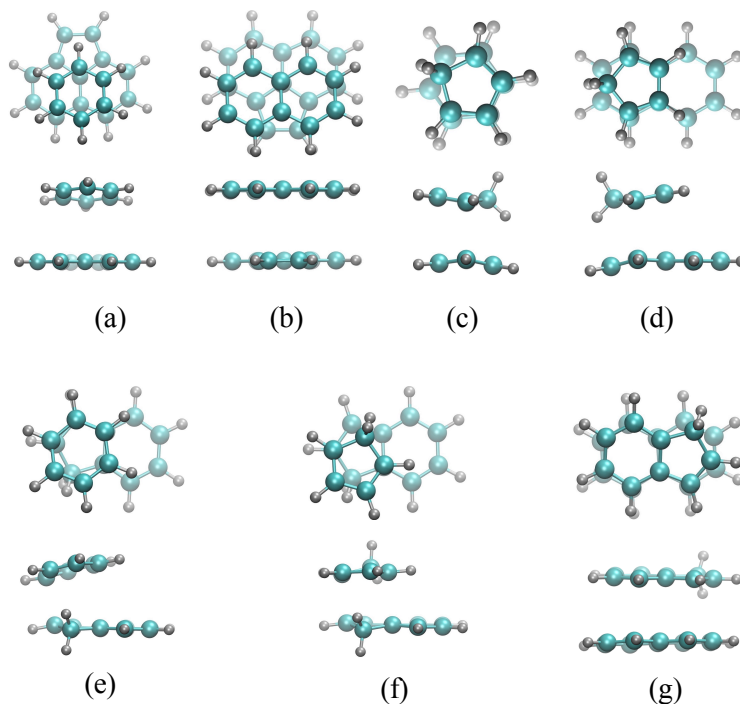


Figure 5.6: Heterodimer structures optimized in the S_1 state for the (a) benz-ace complex, (b) naph-ace complex, (c) benz-cyclo complex, (d) cyclo-naph complex, (e) benz-ind complex, (f) cyclo-ind complex, and (g) ind-naph complex shown from top and side views.

Complexes Containing Cyclopenta-Fused Groups

The ace monomer introduces an unsaturated cyclopenta-fused ring. The presence of this ring decreases distortion in the excited state—the three structures containing ace each have monomers with planarity indices lower than the ones calculated for the naph dimer, and the minimum value of r_{CC} is 2.9. In the ace-benz and ace-naph complexes, the smaller monomers remain even closer to perfect planarity.

The ace excimer shows the same eclipsed geometry observed for the naph excimer. The benz-ace exciplex and naph-ace exciplex, however, each have the smaller monomer shifted away from the ace monomer's two six-membered rings. In the benz-ace exciplex, the benz monomer is centered between the two 6-membered rings in the ace monomer and shifted toward the cyclopenta-fused group. The benz monomer is also tilted relative to the ace monomer, with a minimum r_{CC} of 3.08 Å and a maximum r_{CC} of 3.91 Å. Although the naph monomer in the naph-ace exciplex is similarly shifted toward the cyclopenta-fused group, no such tilting is observed. Values for r_{CC} are all greater than 3.3 Å.

These minimal excited-state conformational changes and high intermolecular C-C

distances are associated with small $E_{B,E}$ values that are similar for the benz-ace and naph-ace exciplexes. In both cases, the frontier orbitals are relatively localized on the ace monomer—likely a result of the significantly lower electronic transition energies observed for the ace monomer compared to the benz and naph monomers. Transferring an electron into a much-higher-energy orbital fails to significantly stabilize the complex. Low E_R values for the ace-naph and ace-benz complexes, however, keep ΔE_F in the same range as the other complexes. The slightly higher $E_{B,E}$ and ΔE_F for the ace dimer depress ΔE_F , yielding the second-lowest-energy emission for the complex database.

References

- (1) Mercier, X.; Carrivain, O.; Irimiea, C.; Faccinetto, A.; Therssen, E. **2019**, 1–37.
- (2) Krueger, R. A.; Blanquart, G. *Phys. Chem. Chem. Phys.* **2019**, *21*, 10325–10335.
- (3) Adkins, E. M.; Giaccai, J. A.; Miller, J. H. *Proc. Combust. Inst.* **2017**, *36*, 957–964.
- (4) Johansson, K. O.; Lai, J. Y. W.; Skeen, S. A.; Popolan-Vaida, D. M.; Wilson, K. R.; Hansen, N.; Violi, A.; Michelsen, H. A. *Proc. Combust. Inst.* **2015**, *35*, 1819–1826.
- (5) Apicella, B.; Carpentieri, A.; Alfè, M.; Barbella, R.; Tregrossi, A.; Pucci, P.; Ciajolo, A. *Proc. Combust. Inst.* **2007**, *31 I*, 547–553.
- (6) Faccinetto, A.; Desgroux, P.; Ziskind, M.; Therssen, E.; Focsa, C. *Combust. Flame* **2011**, *158*, 227–239.
- (7) Schenk, M.; Hansen, N.; Vieker, H.; Beyer, A.; Gölzhäuser, A.; Kohse-Höinghaus, K. *Proc. Combust. Inst.* **2015**, *35*, 1761–1769.
- (8) Schulz, F.; Commodo, M.; Kaiser, K.; De Falco, G.; Minutolo, P.; Meyer, G.; D’Anna, A.; Gross, L. *Proc. Combust. Inst.* **2019**, *37*, 885–892.
- (9) Kholghy, M. R.; Kelesidis, G. A.; Pratsinis, S. *Phys. Chem. Chem. Phys.* **2018**, *20*, 10926–10938.
- (10) Blanquart, G.; Pitsch, H. In *Combustion Generated Fine Carbonaceous Particles*, Bockhorn, H., D’Anna, A., Sarofim, A. F., Wang, H., Eds.; Karlsruhe University Press: 2008, pp 437–464.
- (11) Lai, J. Y. W.; Elvati, P.; Violi, A. *Phys. Chem. Chem. Phys.* **2014**, *16*, 7969–7979.
- (12) Jerez, A.; Villanueva, J. J. C.; Figueira, L. F.; Demarco, R.; Fuentes, A. **2018**.

- (13) Kuritz, N.; Stein, T.; Baer, R.; Kronik, L. *J. Chem. Theory Comput.* **2011**, *7*, 2408–2415.
- (14) Stein, T.; Kronik, L.; Baer, R. *J. Am. Chem. Soc.* **2009**, *131*, 2818–2820.
- (15) Leininger, T.; Stoll, H.; Werner, H.-J.; Savin, A. *Chem. Phys. Lett.* **1997**, *275*, 151–160.
- (16) Weigend, F.; Ahlrichs, R. *Phys. Chem. Chem. Phys.* **2005**, *7*, 3297–3305.
- (17) Krueger, R. A.; Blanquart, G. *J. Phys. Chem. A* **2019**, *123*, 1796–1806.
- (18) Neese, F. *Wiley Interdiscip. Rev. Comput. Mol. Sci.* **2012**, *2*, 73–78.
- (19) Grimme, S. *J. Chem. Phys.* **2006**, *124*, 034108.
- (20) Grimme, S.; Ehrlich, S.; Goerigk, L. *J. Comput. Chem.* **2010**, *31*, 2967–2970.
- (21) Goerigk, L.; Grimme, S. *Phys. Chem. Chem. Phys.* **2011**, *13*, 6670.
- (22) Weigend, F.; Häser, M.; Patzelt, H.; Ahlrichs, R. *Chem. Phys. Lett.* **1998**, *294*, 143–152.
- (23) Plimpton, S. *J. Comp. Phys.* **1995**, *117*, 1–19.
- (24) Hoover, W. G. *Phys. Rev. A* **1985**, *31*, 1695–1697.
- (25) Robertson, M. J.; Tirado-Rives, J.; Jorgensen, W. L. *J. Chem. Theory Comput.* **2015**, *11*, 3499–3509.
- (26) Dodda, L. S.; Cabeza de Vaca, I.; Tirado-Rives, J.; Jorgensen, W. L. *Nuc. Acids Res.* **2017**, *W1*, 6665–6670.
- (27) Hernández-rojas, J.; Calvo, F. *Phys. Chem. Chem. Phys.* **2019**, 5123–5132.
- (28) Totton, T. S.; Misquitta, A. J.; Kraft, M. *Phys. Chem. Chem. Phys.* **2012**, *14*, 4081–94.
- (29) Chung, S. H.; Violi, A. *Proc. Combust. Inst.* **2011**, *33*, 693–700.
- (30) Sabbah, H.; Biennier, L.; Klippenstein, S. J.; Sims, I. R.; Rowe, B. R. *J. Phys. Chem. Lett.* **2010**, *1*, 2962–2967.
- (31) Miyazaki, M.; Fujii, M. *Phys. Chem. Chem. Phys.* **2015**, *17*, 25989–25997.
- (32) Chandrasekaran, V.; Biennier, L.; Arunan, E.; Talbi, D.; Georges, R. *J. Phys. Chem. A* **2011**, *115*, 11263–11268.
- (33) Bludský, O.; Rubeš, M.; Soldán, P.; Nachtigall, P. *J. Chem. Phys.* **2008**, *128*, 114102.
- (34) Dubinets, N. O.; Safonov, A. A.; Bagaturyants, A. A. *J. Phys. Chem. A* **2016**, *120*, 2779–2782.
- (35) Podeszwa, R.; Szalewicz, K. *Phys. Chem. Chem. Phys.* **2008**, *10*, 2735–2746.
- (36) Saigusa, H.; Lim, E. C. *Acc. Chem. Res.* **1996**, *29*, 171–178.

- (37) Liu, J.; Herbert, J. M. *J. Chem. Phys.* **2017**, *034106*, 034106.
- (38) Krueger, R. A.; Blanquart, G. *Int. J. Quantum Chem.* **2019**, *119*, e25819.
- (39) Diri, K.; Krylov, A. I. *J. Phys. Chem. A* **2012**, *116*, 653–662.
- (40) Antić, M.; Furtula, B.; Radenković, S. *J. Phys. Chem. A* **2017**, *121*, 3616–3626.
- (41) Plasser, F.; Lischka, H. *J. Chem. Theory Comput.* **2012**, *8*, 2777–2789.

CONCLUSIONS AND OUTLOOK

6.1 Basis Set Selection for Multireference Calculations: Best Practices

The sensitive dependence of binding energy on basis set size and diffuseness reported in this work underscores the importance of careful basis set selection for accurate exciplex characterization. In the case studies presented here, extrapolated counterpoise-corrected double- and triple-zeta binding energies calculated using the moderately diffuse jun-cc-pV(N+d)Z basis set were in extremely good agreement with CBS values obtained from much more expensive triple- and quadruple-zeta jul-cc-pV(N+d)Z and aug-cc-pVNZ basis sets. These results suggest that diffuse basis functions may be necessary to obtain exciplex binding energies that are “right for the right reasons” or to calculate accurate properties based on the electron density, but the moderately augmented jun- and jul-cc-pV(N+d)Z basis set families yield energetic results virtually identical to the aug-cc-pVNZ family at significantly lower cost for $N > 2$.

These cases highlight the favorable basis set convergence properties of CP-corrected binding energies. Although a given $E_{B,CP}$ may be far from the correct result and also from the E_B computed using the same basis, the $E_{B,CBS}$ values extrapolated from the moderately-augmented jun-cc-pV(D+d)Z and jun-cc-pV(T+d)Z basis sets fall within 10% of the values obtained using the most expensive basis sets possible for the (BzBz)* and (BdBz)* systems. Calculating the CP correction requires two more energy evaluations than the uncorrected binding energy if monomer geometry remains constant, but these additional evaluations are never more expensive than the ones performed to obtain E_B .

Our examples also suggest that the common practice of using uncorrected aug-cc-pVTZ binding energies as a reference is extremely risky, given the potential for high BSSE. In the future, larger benchmark studies will play an important role in establishing guidelines for multireference calculations involving excited-state noncovalent interactions.

In this work, we have demonstrated for the first time the stability of the benzene-naphthalene and *cis*-butadiene–benzene exciplexes. We have also demonstrated that the E_B and $E_{B,CP}$ values computed for these weakly-bound complexes are subject

to larger error than the ones computed for the strongly-bound benzene excimer, and the $E_{B,CBS}$ are subject to greater uncertainty.

6.2 Asymmetric Acene Exciplex Properties via Multireference and DFT Methods

Next, we have reported the binding energies, geometries, and exciton properties of three acene exciplexes. These represents the first theoretical investigation of the benzene-anthracene and naphthalene-anthracene exciplexes, and the first TDDFT investigation of the benzene-naphthalene exciplex. CASSCF/NEVPT2 benchmark calculations have been performed to account for multireference character. We have shown that the benzene-naphthalene and naphthalene-anthracene exciplexes are stabilized by a moderate degree of exciton delocalization over both monomers and charge transfer that is revealed by analysis of TDDFT one-electron transition density matrices. The exciton in the benzene-anthracene complex is shown to be localized almost entirely on the anthracene monomer, perhaps because the large difference in the energies of each monomer's frontier orbitals inhibit their mixing and thus the formation of bonding orbitals. In every case, though, the degree of stabilization makes the electronic structure of the mixed exciplexes distinct from both the parent monomers and excimers of the parent monomers, an experimentally observable effect that should be accounted for in interpretation of fluorescence spectra.

The difficulties involved with calculating accurate valence excitation energies for acenes using TDDFT are well known, but this work also demonstrates that the accuracy of exciplex binding energies depends on the character of the monomer excited state from which the exciplex is derived. Binding energy errors are not easily predictable from the magnitude of the monomer excitation energy error. Double-hybrid functionals offer advantages over hybrid GGAs in providing a balanced description of both states, but strong overbinding is still observed for L_b -derived states. Significant variation is observed among the range-separated functionals considered, with functionals in the ω B97 family yielding inconsistent results. While the LC-BLYP functional is extremely underbinding for all complexes, tuning the range-separation parameter for each complex, or even for the larger monomer in each complex, improves binding energies significantly. Despite many promising results, it is clear that noncovalent excited-state interactions remain a significant challenge for TDDFT methods.

6.3 Towards a Predictive Model for Aromatic Exciplex Fluorescence Emission Energies

Our results show that many of the noncovalent and aliphatically-bridged complexes that can be formed from small to moderately-sized, flame-relevant PAHs have fluorescence emission energies in the visible range. The emission energy for complexes depends strongly on monomer topology. Within the sets of tetracene isomers and pentacene isomers, clear linear relationships exist between geometric characteristics such as the number of zig-zag edge groups and mean excited-state bond length and the excimer emission energy. Monomer HOMO-LUMO gap provides an excellent proxy for geometric effects on emission energy.

While the simple geometric models prove less predictive for a database of complexes containing both homo- and heterodimers, the linear relationship with the mean monomer HOMO-LUMO gap still accounts for almost 80% of the variation in complex emission energies. The value of this observation is clear: not only do polynomial-scaling computational costs for electronic structure methods make calculations of monomer properties significantly cheaper than dimer properties, but $\sim n^2$ complex fluorescence energies may be predicted from a database of n HOMO-LUMO gaps. It is important to note, though, that this model does not provide a means of distinguishing between complexes with similar mean HOMO-LUMO gaps on the basis of fluorescence emission energy. Complex-specific calculations will be required when an error of $\approx 3000 \text{ cm}^{-1}$ is not acceptable.

Lastly, we have shown that the presence of aliphatic linkers does not significantly affect trends in fluorescence emission energies. The variation in fluorescence observed is the result of distortion of the minimum-energy noncovalent complex structure and also delocalization of the orbitals involved in the transition over the covalent linker. Distinguishing between noncovalent and bridged structures will require more detailed analysis of spectral features or a combination of experimental methods.

6.4 Exploring the Spectroscopic Impacts of Five-Membered Ring Groups in PAH Complexes

Cyclopentadienyl groups and cyclopenta-fused groups each have distinctive effects on the spectroscopic properties of PAH clusters. Cyclopentadienyl groups undergo significant distortion in the excited state, causing strong excited-state binding as well as ground-state repulsion that produces low-energy fluorescence, especially in the smallest complexes. Complexes containing acenaphthylene, on the other

hand, show weaker excited-state binding for their size and correspondingly weak ground state repulsion. The acenaphthylene monomer is marked by extremely low-energy transitions relative to its parent PAH naphthalene, suggesting that larger molecules with one or more cyclopenta-fused groups might account for visible-range spectroscopic activity in flames. Moreover, noncovalent dimers containing both types of five-membered rings bind as strongly in the ground state as similarly-sized PAHs, suggesting that if transient noncovalent PAH complexes play a role in the soot nucleation process, complexes containing five-membered rings likely do as well. Symmetry differences as well as probable differences in vibrational mode energies due to the greater diversity of C-C bond types have the potential to yield large entropic differences between the two populations of monomers, making it important to consider both in soot nucleation models.

6.5 Directions for Future Work

Further theoretical characterization of the photoresponse of PAH complexes could proceed in two directions. The first involves applying the techniques described in this work to a broader range of flame-relevant species. These species might include PAHs substituted with oxygen-containing groups or with unsaturated aliphatic groups. Aliphatically-bridged PAH dimers with different bridge groups—including unsaturated or even aromatic chains—could also be considered.

Another avenue for investigation involves prediction of different spectroscopic characteristics for each complex. Computing vibrationally-resolved electronic spectra would provide a richer data set for fitting of experimental spectra as well as yielding insight about the dynamics of the electronic transitions. Oscillator strengths computed for relevant conformations for each complex could also be used in spectral fitting. To quantify the error associated with the TDDFT prediction of vibrational frequencies and oscillator strength, further benchmarking would likely be required.